Flexible transparent electrodes for optoelectronic devices

Dissertation

zur Erlangung des akademischen Grades
doctor rerum naturalium (Dr. rer. nat.) im Fach Physik
eingereicht an der

Mathematisch-Naturwissenschaftlichen Fakultät
Humboldt-Universität zu Berlin

von

Herrn Dipl.-Ing. Lukas Kinner

Präsidentin der Humboldt-Universität zu Berlin:
Prof. Dr.-Ing. Dr. Sabine Kunst
Dekan der Mathematisch-Naturwissenschaftlichen Fakultät:
Prof. Dr. Elmar Kulke

Betreuer / 1. Gutachter: Prof. Dr. Emil List-Kratochvil

Gutachter:
2. Prof. Dr. Thomas Riedl
3. Prof. Dr. Oliver Benson

Co-Betreuer:
Dr. Theodoros Dimopoulos
Dr. Felix Hermerschmidt

Tag der mündlichen Prüfung: 27.01.2021

„Ich erkläre, dass ich die Dissertation selbständig und nur unter Verwendung der von mir gemäß § 7 Abs. 3 der Promotionsordnung der Mathematisch-Naturwissenschaftlichen Fakultät, veröffentlicht im Amtlichen Mitteilungsblatt der Humboldt-Universität zu Berlin Nr. 42/2018 am 11.07.2018 angegebenen Hilfsmittel angefertigt habe."

_____

Datum, Unterschrift

To Lena

Acknowledgement

Finishing a Ph.D. thesis is not an easy task, yet it is not the bare effort of one alone. Many people accompanied me during this scientific journey like the Fellowship of the Ring accompanied Frodo on his journey to Mount Doom.

First of all, I want to thank the longest companion of my journey, Prof. Emil J. W. List-Kratochvil, who introduced me to this topic when I even had no master's degree. He gave me the possibility to work with his group in Berlin and brought me in contact with the AIT. Hence, I had the pleasure to do my Ph.D. in an international collaboration and work on the topic from many different points of view.

At the AIT, Dr. Theodoros Dimopoulos was my supervisor for the last 4 years. I sincerely want to thank him for sharing so much of his knowledge about the topic and general scientific working strategies with me. In our fruitful discussions, I learned a lot and I will for sure continue to use this knowledge for the rest of my scientific career.

Furthermore, I want to express my deep gratitude to Dr. Felix Hermerschmidt. In the labs of HU, Felix took me under his wing. He was always there for me to refine my writing skills but also brightened up tough working days with hilarious jokes and really nice conversations. Thank you so much – I never expected to find in the short amount of time I spent in Berlin a "scientific partner" *and* a friend.

I also want to thank my office partner Dr. Nina Plankensteiner, whom I got to know as Nina Winkler. It was of great use to have the direct help of a chemist in the office and to have the possibility to spend many evenings with Tarock to focus on different things than work.

Regarding Ph.D.-student related work-life-balance, I want to thank Dr. Martin Bauch. He not only helped me to get "stronger" in terms of programming and theoretical optics but also helped me get "stronger" physically since we spent many hours prior to work at the gym together. I am glad to say that for the last 4 years, he was not just a man I spent time with at the gym and work, he was my "best man" at my wedding last year. I am happy to finally not just receive support from him but to support him at his wedding in September as "best man" as well.

From the group at HU, I also want to thank Dr. Giovanni Ligorio for not only performing XPS measurements, but also helping me to understand and analyze the data. In addition, I want to thank Paul Zybarth and Bodo Kranz. Both of them integrated me very fast into the workflow at the labs in Berlin. Because of that, I was able to save a lot of time at my short Berlin trips.

To my friends I want to say thank you for helping me to take a break and have joyful moments, which regenerated me to carry on working.

Moreover, I want to thank my family for their support over the last 4 years, on the one hand I am very thankful for my parents who always believed in me and laid the foundation for my career by giving me the privilege of education and a cordial home, on the other hand my siblings who are truly my academic inspiration and always took care of their “smallest” brother.

Last but far from least, in fact the most important person to whom I want to express my gratefulness and love is my wife Lena, who was always there for me when I needed it the most. The last 4 years have been challenging for me in terms of work, but my one and only love made my live a lot easier with her endless support and patience. Especially, our wedding was the best day of the last 4 years and of course my entire life. Our honeymoon - which followed the wedding – helped a lot to regain enough energy to finish off this thesis. Thank YOU!

Abstract

Transparent electrodes (TEs) are a key element incorporated in many examples of modern optoelectronics (photovoltaics, displays and organic light-emitting diodes). All the mentioned devices rely on TEs to assure simultaneous light interaction with the active device layers and efficient charge carrier injection or extraction. The most widely used TE in today's industry is indium tin oxide (ITO).

However, there are downsides to the use of ITO, such as its scarcity and some of its inherent properties, such as its brittleness. The scope of this thesis is therefore to discuss alternatives to ITO. These alternatives must feature high flexibility if bent and low temperature processing in order to access thermally sensitive flexible substrates, while featuring higher or at least equal transmittance and conductivity compared to ITO. Two main approaches are examined in this thesis - one approach is based on using dielectric/metal/dielectric (DMD) films and the other is based on using silver nanowire (NW) films.

For the first approach, DMD electrodes are fabricated on glass and flexible polyethylene terephthalate (PET) substrates. A combination of sputtered TiO_x/Ag/AZO was found to yield the highest transmittance and conductivity ever reported for an electrode on glass and PET with an average transmittance larger than 85 % (including the substrate) in the range 400-700 nm and sheet resistance below 6 Ω/sq. Within a broad visible spectral range, the transmittance of the flexible electrode surpasses the transmittance of the bare PET. This performance was enabled by the use of a polymer layer between the PET and the DMD electrode. The interlayer modifies the growth of the TiO_x on the flexible substrate, rendering it similar to its growth on glass. This markedly increases the transmittance of the DMD electrode and effectively decreases its sheet resistance. The final electrode outperformed PET/ITO substrates in bending tests.

To test the device performance of TiO_x/Ag/AZO, DMD electrodes were implemented in organic light emitting diodes (OLEDs) with a solution-processed emitting layer. The OLED devices were fabricated in the inverted architecture, employing a ZnO:polyethylenimine, nanoparticle layer on top of the DMD for electron injection and a MoO_3 layer for hole injection. The results showed that the OLED devices with DMD electrodes on PET and glass outperform the ITO-based reference OLED devices in terms of maximum luminance as well as current efficacy. Specifically, DMD-based devices achieve up to 30 % higher current efficacy on glass and up to 260 % higher efficacy on PET, as compared to the ITO-based reference devices. Maximum luminance reaches up to 100000 cd m^{-2} for the DMD OLEDs on glass and 43000 cd m^{-2} for those on PET. This performance is attributed to the low sheet resistance of the electrodes combined with efficient light outcoupling and shows the potential of DMDs to replace ITO in modern optoelectronic devices. The presented electrode has a large potential for photovoltaic and optoelectronic applications, outperforming ITO.

As a second approach to achieve the goal of flexible transparent electrodes, NWs were investigated. The implementation of silver nanowires as TEs in solution processed organic light emitting diodes still faces two major challenges: high roughness of nanowire films and heat sensitivity of the most commonly used transparent substrate PET. Therefore, within this thesis, an embedding process with different variations is elaborated to obtain highly conductive and transparent electrodes of NWs on flexible PET substrates.

Firstly, the NWs are embedded into a UV-curable polymer, to reduce the electrode roughness and to enhance its stability. For the purpose of device integration, the NWs must touch the surface of the polymer; this demands that their embedding is followed by a transfer step from a host to a final substrate. Since the NWs require some sort of post deposition treatment (thermal or plasma) to reduce the electrode sheet resistance, a thermally stable host substrate is generally used. Both, thermally stable polyimide as well as temperature-sensitive PET can be used as flexible host substrates. This is made possible by adjusting the fabrication process sequence to accommodate the plasma curing step of the NWs. As a result, embedded NW electrodes, transferred from polyimide-to-PET and from PET-to-PET are obtained with a transmittance of 80 % (including the substrate) and sheet resistance of 13 Ω/sq, similar to electrodes transferred from glass-to-glass substrates. The attained highly conductive and transparent embedded NW electrodes on PET show superior performance in bending tests compared to PET/ITO samples. The introduced approach, involving low-cost flexible substrates, NW spray coating and plasma curing, is compatible with high-throughput, roll-to-roll processing.

As with the DMD electrodes, NW electrodes are implemented in a solution-processed organic light emitting diode with PDY-132 (Super Yellow) as the emissive layer. In contrast to many other works in this field, a ZnO:polyethylenimine nanoparticle electron injection layer is used on the nanowires instead of PEDOT:PSS or other organic hole injectors. The use of ZnO nanoparticles and polyethylenimine instead of pure organic layers yields many advantages in terms of process and device stability. The resulting devices show greater flexibility, conductivity and luminance than the PET/ITO reference devices, while having the same power efficacy.

Kurzfassung

Transparente Elektroden (TE) sind unverzichtbar in modernen optoelektronischen Bauelementen wie Photovoltaik, Bildschirme und organische Licht emittierende Dioden, da sie die gleichzeitige Interaktion von Licht und elektrischen Ladungsträgern mit der optisch aktiven Schicht gewährleisten. Die derzeitig am häufigsten verwendete TE ist Indium Zinn Oxid (ITO).

Obgleich am häufigsten eingesetzt, weißt ITO viele Nachteile auf wie beispielsweise, die Verwendung des seltenen Metalls Indium. Des Weiteren ist ITO spröde. Aufgrund der Nachteile von ITO scheint es wichtig, über Alternativen nachzudenken. Die vorliegende Arbeit setzt sich deshalb unter anderem mit ITO-Alternativen auseinander, die unter Biegestress mechanisch flexible sind und eine niedrige Herstellungstemperatur aufweisen, um thermisch sensible flexible Substrate beschichten zu können. Im Vergleich zu ITO sollen die Alterativen dennoch eine gleichhohe oder höhere Transmission und Leitfähigkeit aufweisen. Um das zu erreichen, werden hauptsächlich zwei verschiedene Ansätze in dieser Arbeit untersucht. Der erste Ansatz beruht auf Dielektrikum/Metall/Dielektrikum (DMD) Filmen, im zweites Ansatz werden Silber Nanodrähten (NW) als TE untersucht.

Im ersten Ansatz wurden DMD Elektroden auf Glas und Polyethylenterephthalat (PET) fabriziert. Eine Kombination von gesputterten TiO_x/Ag/AZO Schichten lieferte die höchste jemals gemessene Transmission und Leitfähigkeit für eine Elektrode auf Glas und PET. Als solche wies sie eine durchschnittliche Transmission größer als 85 % (inklusive Substrat) im Bereich von 400-700 nm und einen Schichtwiderstand von unter 6 Ω/sq auf. In einem breiten Spektralbereich des sichtbaren Spektrums übersteigt die Transmission der flexiblen Elektrode überdies die Transmission von PET. Diese Leistung wurde durch die Nutzung einer Polymerschicht zwischen PET und der DMD Elektrode erlangt. Durch die Zwischenschicht verhält sich das TiO_x Wachstum auf dem flexiblen Substrat ähnlich zu Glas. Dadurch steigert sich die Transmission merklich und der Schichtwiderstand wird effektiv reduziert. Die fertige Elektrode weist eine deutlich höhere Biegestabilität als ITO auf.

Um die Leistung der TiO_x/Ag/AZO Elektrode in einem Bauteil zu überprüfen, wurde sie in einer flüssig-prozessierten organischen Licht emittierenden Diode (OLED) implementiert. Unter Verwendung einer ZnO:Polyethylenimin Nanopartikelschicht als Elektronen Injektionsschicht und einer MoO_3 Schicht als Loch Injektionsschicht wurde die OLED in einer invertierten Architektur realisiert. Im Vergleich zu den Bauteilen auf PET/ITO und Glas/ITO zeigten OLEDs mit DMD Elektroden auf Glas und PET eine höhere maximale Luminanz und Strom Effizienz. Genaugenommen erreichten die DMD-basierten OLEDs eine 30 % höhere Strom Effizienz auf Glas und eine 260 % höhere Strom Effizienz auf PET im Unterschied zu den ITO-basierten Bauteilen. Die maximale Luminanz der DMD Elektroden auf Glas erzielte fast 100000 cd m^{-2} und 43000 cd m^{-2} auf PET. Diese Leistung beruht auf dem niedrigen Schichtwiderstand der DMD Elektrode kombiniert mit effizienter Licht Auskopplung und beweist das Potential der DMD Elektrode als ITO Ersatz in modernen optoelektronischen Bauteilen. Die gezeigte TiO_x/Ag/AZO

Elektrode hat somit ein größeres Potential für Anwendungen in Photovoltaik und anderen optoelektronischen Anwendungen als ITO.

Im zweiten Ansatz zur Realisierung flexibler transparenter Elektroden wurden NWs diskutiert. Die Implementierung von Nanodrähten in lösungsprozessierten organischen Licht emittierenden Dioden weißt noch immer zwei große Hürden auf: hohe Rauigkeit der Nanodrahtfilme und Wärmeempfindlichkeit des am meist genutzten transparenten flexiblen Substrates PET. Im Umfang der Arbeit werden deshalb verschiedene Versionen eines Einbettprozesses untersucht, um eine hoch leitfähige und transparente Elektrode auf Basis von Nanodrähten auf PET Substraten zu erhalten.

Um die Rauigkeit zu verkleinern und gleichzeitig die Stabilität zu erhöhen werden zunächst die Nanodrähte in ein UV-härtendes Polymer eingebettet. Zum Zwecke der Integration in ein Dünnschichtbauteil müssen die Nanodrähte die Oberfläche des Polymers berühren. Dafür braucht es den Transfer von einem Gast-Substrat zu einem Finalen-Substrat. Um den Schichtwiderstand von Nanodrahtfilmen zu reduzieren, muss eine Form der Nachbehandlung (thermisch oder via Plasma) stattfinden. Auf Grund dessen wird allgemein ein thermisch stabiles Gast-Substrat verwendet. In diesem Fall kann sowohl thermisch stabiles Polyimid als auch temperatur-sensitives PET verwendet werden. Dies wird durch die Änderung der Prozessreihenfolge bei der Herstellung ermöglicht. Final erhält man dadurch eingebettete Nanodraht Elektroden von Polyimid-zu-PET und von PET-zu-PET. In beiden Fällen wird eine Transmission von bis zu 80 % (inklusive Substrat) und ein Schichtwiderstand von 13 Ω/sq erreicht.

Die so erzeugten - hoch leitfähigen und transparenten - Nanodraht Elektroden sind ITO unter mechanischem Biegestress überlegen. Der gezeigte Ansatz beruht auf billigen flexiblen Substraten, Sprühbeschichten und Plasmaschweißen, allesamt Rolle-zu-Rolle skalierbare Prozesse.

Gleich wie bei den DMD Elektroden wurden auch NW Elektroden in eine lösungsprozessierte OLED implementiert. Im Unterschied zu anderen Arbeiten auf dem Feld der NW Elektroden wurde hier eine ZnO:Polyethylenimin Nanopartikelschicht als Elektronen Injektionsschicht anstelle von PEDOT:PSS oder anderen rein organischen Schichten verwendet. Die Verwendung von ZnO Nanopartikel und Polyethylenimin anstelle von reinen organischen Schichten bietet viele Vorteile in Betracht auf die Bauteilstabilität. Die Bauteile zeigten eine größere Flexibilität, Leitfähigkeit und Luminanz als die PET/ITO Referenzen während die selbe Leistungseffizienz erreicht wurde.

List of included Publications

This thesis is mainly based on work that has been published or is submitted at the journals mentioned below. The author of this thesis is also the first author of the listed publications and wrote the manuscripts. The permission to reproduce the content is given by the Creative Commons Attribution 4.0 license. Parts which have been published are indicated within the corresponding chapters. Parts of the reproduced content has been modified.

[1] Kinner L. *et al.* Polymer interlayers on flexible PET substrates enabling ultra-high performance, ITO-free dielectric/metal/dielectric transparent electrode. *Mater. Des.* **168**, 107663 (2019). DOI: 10.1016/j.matdes.2019.107663
Contribution: The author conducted all experiments except for the XPS measurements. The acquisition of the XPS data was carried out by Giovanni Ligorio. The author drafted the manuscript which was then finalized together with the co-authors.

[2] Kinner L. *et al.* Gentle plasma process for embedded silver-nanowire flexible transparent electrodes on temperature-sensitive polymer substrates. *Nanotechnology* **31**, (2020). DOI: 10.1088/1361-6528/ab97aa
Contribution: The author conducted all experiments and then drafted the manuscript which was finalized together with the co-authors.

[3] Kinner L. *et al.* Implementation of Flexible Embedded Nanowire Electrodes in Organic Light-Emitting Diodes. *Phys. Status Solidi - Rapid Res. Lett.* **2000305**, 6–11 (2020). DOI: 10.1002/pssr.202000305
Contribution: The author conducted all experiments and then drafted the manuscript which was finalized together with the co-authors.

[4] Kinner L. *et al.* ITO-free high performance flexible TiO_x/Ag/AZO electrodes for organic light emitting diodes. Submitted at *Mater. Des.* (2020)
Contribution: The author conducted all experiments and then drafted the manuscript which was finalized together with the co-authors.

Table of contents

1 Introduction and scope of the thesis

"You must unlearn what you have learned." - Master Yoda

To many people, invisibility belongs to science fiction- or fantasy-literature and movies. But in today's optoelectronic devices, invisible parts become real and cover a large scientific field. Usually electrode materials like Ag, Cu or Au are not transparent but with the rise of modern optoelectronics it became necessary to make conductors invisible or simply speaking: to create invisible metals.

The history of first transparent and conductive materials dates back to 1907 when Bädeker studied thin films of CdO.[1] The scope of Bädekers work was not the development of a transparent electrode to be implemented in a display or optoelectronic thin film device, because in those days, the state of the art in display technology was the cathode ray tube. Photovoltaic technologies were not mature and lighting was limited to light bulbs.

The technological need for a material which is transparent and conductive came less than 60 years later, when display technology developed from cathode tube to the first plasma display in 1964[2] and the first liquid crystal display in 1968[3]. Both technologies rely on a transparent electrode in the front of the display to control individual pixels and let the generated light out of the display to the observer. In this case, material specific properties of the TE like work function or chemical stability were less important because the electrode works mainly as transparent conductor and the requirements on the material were just transparency and conductivity.

The set of requirements needed to be expanded since 1986, when Tang built the first heterojunction organic photovoltaic cell[4] and one year later with his coworker Van Slyke the first organic light emitting diode[5]. Since then, material specific properties like work function and chemical stability became more important as, the transparent electrode needed to interact with the thin film device in terms of charge carrier injection or extraction and resist chemicals which are directly applied on the TE during processing. Since more than 100 years, transparent electrodes developed from a material study to a key part in modern optoelectronic devices.

TE needs to have high transparency to minimize optical losses, as well as low sheet resistance (R_{sh}). For example: in photovoltaic modules, a TE needs to have a sheet resistance lower than 10 Ω/sq to minimize serial resistance losses and hence reach a competitive power conversion efficiency. Another desired feature for TEs implemented in devices with ultra-thin active layers, is a low surface roughness in order to minimize the risk of shunts and leakage currents.[6–8]

In the last years, the optoelectronics industry is directed towards high-throughput, roll-to-roll (R2R) device processing, using flexible low-cost substrates such as polyethylene terephthalate (PET).[9] The

use of common plastic substrates instead of glass poses problems concerning the thermal stability of the substrate and the mechanical stability of the deposited layers (including TEs), which are prone to damages caused by the substrate bending during the production and operation. TEs are therefore required to address these issues of thermal and mechanical stability.

Today indium tin oxide (ITO) is the most dominant transparent electrode in the industry.[10] ITO deposited on glass shows high transmittance and low enough sheet resistance, necessary for its applications.[11] These facts hold only true if glass is used as substrate; achieving the same performance parameters on PET is difficult. If ITO is deposited on PET the limiting factors for high conductivity are the lower possible substrate temperature during the sputtering process and the high deposition rates necessary to achieve high conductivity.[12]

Therefore, transparent electrodes that address these concerns are needed, especially on flexible substrates. Hence, the scope of this thesis is the development of flexible transparent electrodes. Two approaches were chosen to fulfill this topic: On the one hand the study of dielectric metal dielectric (DMD) electrodes (chapter 4) and on the other hand the use of spray coated silver nanowire (NW) thin films (chapter 5). Both techniques feature up scalable potential which is important for future industrial application. Both approaches were first tested on glass to eliminate potential influence from PET. Later on, the processes and methods were modified for an optimized application on PET.

For a general understanding of the underlying physical theory, chapter two presents fundamentals and background. Detailed experimental methods and processes are described in chapter three. Chapter four presents the approach to develop a flexible transparent electrode via different dielectric metal dielectric layer sequences. First, different material sequences are presented yielding a combination of TiO_x/Ag/AZO as the most promising layer sequence. Sputtering the TiO_x/Ag/AZO electrode on PET proofed to be difficult due to initial substrate roughness of PET. Different ways of improving surface roughness and hence electrode performance are shown. In the end, an approach to build OLEDs on the outstandingly performing electrode is given. The presented devices outperform the reference devices on commercial PET/ITO substrates in terms of luminance, efficiency and mechanical stability.

Chapter five shows the approach in developing flexible TE on the base of silver nanowire thin films. Silver nanowires are solution processed which is a cheap processing method. To work around the high roughness of silver nanowire films an embedding process for inkjet printed silver grids was adapted for the nanowires to yield a smooth electrode surface. The process is further adapted in a way that heat sensitive, but cheap PET substrates can be used. Finally, OLED devices were processed on the embedded nanowire electrodes on glass and PET. The devices on the embedded nanowire electrode also outperformed the reference devices on commercial PET/ITO substrates in terms of luminance, efficiency and mechanical stability.

2 Fundamentals and background

Transparency and electrical conductivity seem to be trivial material properties. It is well known that glass is transparent not conductive and brittle while metals are not transparent, highly conductive and flexible. Solid state physics explains why different material types exist and how their macroscopic properties arise. This chapter deals with the physical models used in solid state physics which are necessary for the understanding of materials to develop a flexible transparent electrode.

2.1 From atomic bonds in matter to electronical and optical properties of solids

Electrical conductivity is one key property of transparent electrodes. The following chapter explains how and why electrical conductivity arises in some solids. Macroscopic material properties are defined by the sort of atoms in the solid, how the atoms are arranged in the solid and how the atoms are bound to each other. The type of atoms influences the type of bonding and to some degree the arrangement of the atoms. The arrangement of atoms in the solid can additionally be influenced by physical parameters. For example: carbon can exist in the form of graphite (coal) or diamond if high pressure and high temperature are applied.

The arrangement of atoms can roughly be used to divide solids into two categories: crystalline solids (regular atomic pattern) and amorphous solids (irregular atomic pattern). Crystalline solids are for example metals, while amorphous solids are for example glasses.[13]

Crystalline solids with a geometric atomic pattern offer the possibility to calculate macroscopic properties with quantum mechanical techniques. To do so, consider two single atoms as shown in Figure 2.1-1 (a). In the single atom case, electrons are surrounding the core in so called atomic orbitals, which have discrete energy levels. These orbitals are energetically allowed states in which the electron can surround the core without losing energy.[14]

If two or more atoms form a chemical bond, their orbitals start to overlap (Figure 2.1-1 (b)). As dictated by Pauli's exclusion principle, two electrons cannot occupy the same quantum state within a molecule. Hence, one atomic orbital needs to split up into two molecular orbitals (Figure 2.1-1 (b)). The new molecular orbitals have slightly different energy and allow each electron its own molecular orbital.[15]

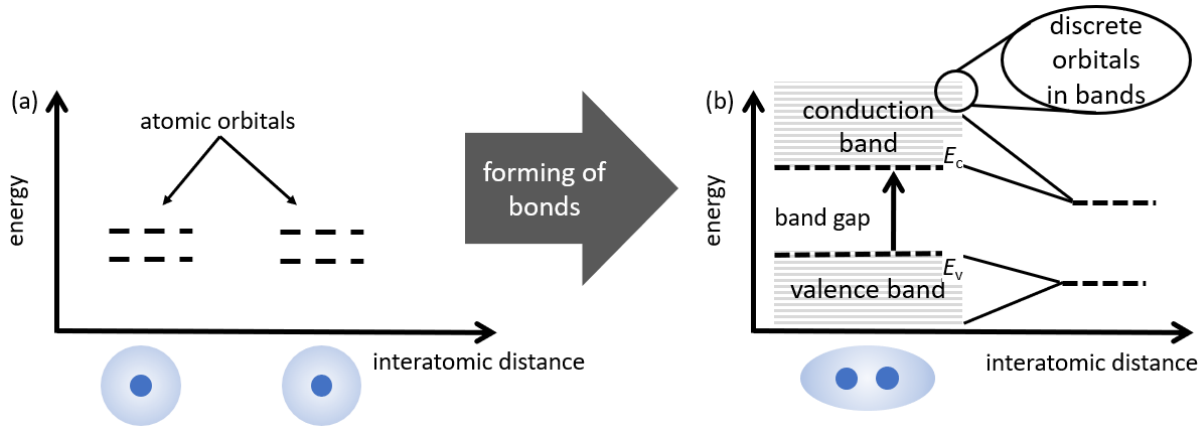

Figure 2.1-1: Transition of atomic orbitals (a) to molecular bands (b) by forming orbital overlap. The overlap of orbitals leads to the formation of bands (valence; conduction) in the solid-state body. Within the bands, electrons can only occupy discrete energy levels. Valence and conduction band can be separated by a bandgap where no electronic states exist. Taken from [16] and modified.

If the number of atoms in a solid N is large (~10^{22}), the number of orbitals is large with small energetic spacings in between (order of ~10^{-22} eV). These levels are so close together to be considered as one continuous energy band. As shown in Figure 2.1-1 (b), many discrete molecular orbitals form a band.[15]

2.1.1 Electronic band structure - forming the backbone of conductivity in solids

Theoretical band structures are calculated by solving the Schrödinger equation for electrons in the periodic potential of the atoms in the corresponding solid. Energetic areas, where no solution for the Schrödinger equation exists, lead to gaps between the bands (Figure 2.1-2 (b)) where electrons cannot be. These band gaps correspond to the energetic forbidden areas between discrete atomic orbitals.[13]
Energetic lower bands which form the bonds between the atoms and which have more localized electrons are called valence bands. Energetic higher bands with highly delocalized electrons are called conduction bands. This is because electrons can move along these bands through the solid.[14]
The Fermi level (E_F) is an important quantity in the band model of solid sates body. Fermi level should not be confused with Fermi energy. Fermi energy is a hypothetical quantity defined as the difference between the highest and lowest single particle state in a quantum system of non-interacting fermions at absolute zero K.[14]
However, in a real solid body, fermions (electrons) are interacting and T never equals 0 K. Therefore, E_F is a more useful quantity. E_F is defined as an energy level within the band structure which has at any given time a probability of 50 % to be occupied at thermodynamic equilibrium. The fact, that for electron conduction a state needs to be filled only part-time, makes this 50 % mark important to

characterize materials in terms of conductivity. If a state would be filled all the time with an electron, it would block this passage for other electrons for passing by.

In Figure 2.1-2, the material classifications according to E_F and band gaps are shown. In metals, there is no band gap between valence and conduction band. E_F lies within all the other bands. This is important for high conductivity as conductivity is aided by delocalization of many partially filled states close to E_F.

Figure 2.1-2 illustrates also a variety of semiconductors. An intrinsic semiconductor shows a band gap with E_F being in the band gap. This may imply that a semiconductor is an insulator. But the band gap is so small that at room temperature, some of the states in the conduction band are occupied. Semiconductors display band gaps between 0.1 and 6.4 eV. Further heating would promote more electrons across the band gap into the conduction band to support conductivity.[13–15]

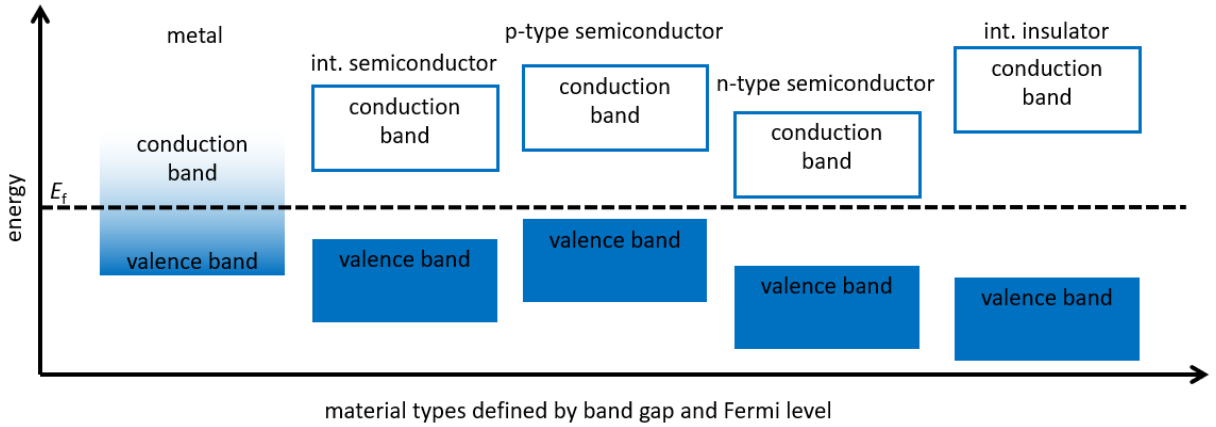

Figure 2.1-2: Characterization of materials by band gap and E_F. From left to right: Metal (no bandgap; E_F in between allowed states; intrinsic semiconductor (small bandgap; E_F in the middle of the bandgap); p-type semiconductor (small bandgap; E_F close to valence band); n-type semiconductor (small bandgap; E_F close to conduction band); intrinsic insulator (large bandgap; E_F in the middle of the bandgap). Taken from [16] and modified.

Another way to change the conductivity of a semiconductor can be done by doping. Doping is a process in which the atomic lattice of the solid is influenced by introducing extrinsic atoms into the lattice. If a semiconductor is p-doped, the extrinsic material is an electron acceptor which binds electrons. This leads to a shift of the valence band closer to E_F as shown in Figure 2.1-2. In contrast, n-doping is achieved by introducing an extrinsic electron donor into the lattice. As shown in Figure 2.1-2, this leads to a shift of the conduction band closer to E_F. P- and n-type semiconductors are also called extrinsic semiconductors. They have extrinsic atoms in the lattice compared to the intrinsic semiconductor, which has its properties without extrinsic atoms.[13–15]

The last material in Figure 2.1-2 is an insulator. Insulators show an E_F within the band gap like a semiconductor but their band gaps are far wider with approximate gaps of 15 eV.[13–15]

To sum up the theoretical description of solids: a solid can be a metal, a semiconductor or an insulator in terms of band gap consideration.

In practice, solids which are able to electrically conduct, are simply quantified by their resistivity (ρ) which is given in Ωm.[17] Resistivity needs to be multiplied by the length to cross section ratio of the conductor to yield the macroscopic value resistance (R) given in Ω, as shown in Eq. 1. The graphical description is shown in Figure 2.1-3 (a). If the cross section of a material is high, resistance is reduced. If the length of the conductor is increased, the resistance is also increased.

$$R = \rho \frac{L}{A} \qquad \text{Eq. 1}$$

R…resistance; *ρ*…resistivity; *L*…length of material; *A*…cross section of material

Supposing the form of the material is more like a thin film (2-dimensional) than a macroscopic (3-dimensional) body, one speaks of sheet resistance. The graphical transformation from calculating R to calculating R_{sh} is shown in Figure 2.1-3 (a-b). The 2-dimensional film is the most common case for TE since L and W are much larger than t. For example: in the case of this thesis, samples are 25 x 25 mm^2 while the conducting film thickness is between 10 and 100 nm.

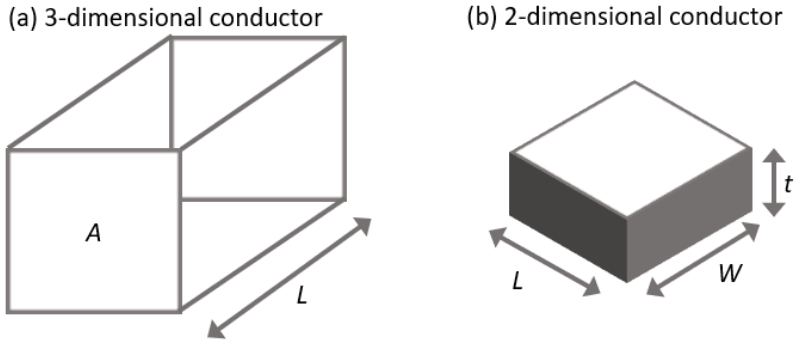

Figure 2.1-3: Definition of geometrical quantities of resistance of a 3-dimensional conductor (a) and a 2-dimensional conducting thin film (b).

R_{sh} is defined according to Eq. 2, the material dependent resistivity divided by the film thickness t. R_{sh} is given in Ω per square (Ω/sq), to distinguish it from normal resistance.[18]

$$R = \rho \frac{L}{A} = \rho \frac{L}{Wt} = R_{sh} \frac{L}{W} \rightarrow R_{sh} = \frac{\rho}{t} \qquad \text{Eq. 2}$$

R…resistance; *ρ*…resistivity; *L*…length of material; *A*…cross section of material

The inverse of resistivity is conductivity σ. Both values are connected by Eq. 3. Conductivity is given in *S/m*. Only a detailed understanding of one of both quantities is necessary to understand which material dependent quantities are influencing it.[17]

$$\sigma = \frac{1}{\rho} \quad \text{Eq. 3}$$

σ…conductivity; ρ…resistivity

A more detailed description and material dependent explanation of conductivity and hence resistivity is given by Eq. 4. Conductivity is proportional to the amount of charge carriers *n*, their elemental charge *e* and their mobility in the solid μ.[17]

$$\sigma = ne\mu \quad \text{Eq. 4}$$

σ…conductivity; *n*…number of charge carriers; *e*…electron charge; μ… mobility

This leads to the conclusion, that high conductivity is either achieved by a high number of mobile charge carriers in the solid or by a high mobility of the charge carriers. Both values are relatively high in the case of metals. In semiconductors, the number of mobile charge carriers is generally low and needs to be elevated for example by doping. However, the amount of charge carrier increase is limited by the dopant solubility in the host material (around 2×10^{21} cm^{-3}). Degenerately doped semiconductors have electron concentrations of up to $n < 1.5 \times 10^{21}$ cm^{-3} a factor of 50–100 lower than the electron concentration in metals.[19]

Mobility is defined by Eq. 5, as factor describing the relation between drift velocity of the charged particle v_d and an external applied electric field *E*.

$$\mu = \frac{E}{v_d} \quad \text{Eq. 5}$$

μ…mobility; v_d…drift velocity; *E*…electric field

In vacuum, an electron would just follow the electric field to ever increasing velocity (ballistic transport). Nevertheless, in solids, the drift velocity is mainly influenced by scattering events which hamper ballistic transport.[20] Electrons in metals are mostly scattered by phonons (lattice vibrations) at room temperature. Scattering events of charge carriers in degenerately doped semiconductors are dominantly induced by ionized impurities such as Sn^+ in ITO, Al^+ in ZnO and F^- or Sb^+ in SnO_2.

2.1.2 The refractive index – defining optical properties of solids

The previous chapter explained the formation of chemical bonds and the subsequent formation of band structures in solids. On the one hand, these band structures influence electrical conductivity. On the other hand, band structures also influence the optical properties of materials. To understand how transmittance of materials can be achieved, the section at hand gives detailed background information of how optical properties of solids arise.

It is widely known that the speed of light in vacuum is constant with 299792458 *m/s*.[21] Yet, light in media other than vacuum travels at lower speeds. The relation of slowing is described in Eq. 6, with *n* called the refractive index.

Thomas Young was the first who mentioned the word "refractive index" in 1807. Before that, it was common to give the relation of the speed of light inside and the speed of light outside the material.[22] From Eq. 6 it can be derived that "normal" materials can have at lowest a refractive index of one, which would be the refractive index of vacuum. Even though so called meta materials with negative refractive indices can be designed, they will not be further discussed here as they do not contribute to the understanding of this thesis.[23]

$$n = \frac{c}{v} \qquad \text{Eq. 6}$$

n… refractive index; *c*…speed of light in vacuum; *v*…phase velocity in medium

The slowing of light in a material and the subsequent regaining of speed when the light exits the material is not trivial. This phenomenon will be explained from two different points of view to make it easier to understand. First a more descriptive approach will be presented in Figure 2.1-4.

A light wave is oscillating freely in vacuum as no charges perturbate the oscillating electric field (1). (The magnetic field component is left out in this description for simplicity reasons.) If light is entering a material, charges are present from the surrounding atoms (2). Electrons and protons can follow the electric field of the light wave (3). Since one single proton is approximately 2000 times heavier than one electron, most of the movement induced by the electric field is done by electrons. This movement must not be confused with absorption because the electrons follow the electric field and create their own electric dipole by swinging. The swinging dipole is generating its own electromagnetic wave (4).[24] The new light wave superimposes with the incident wave.

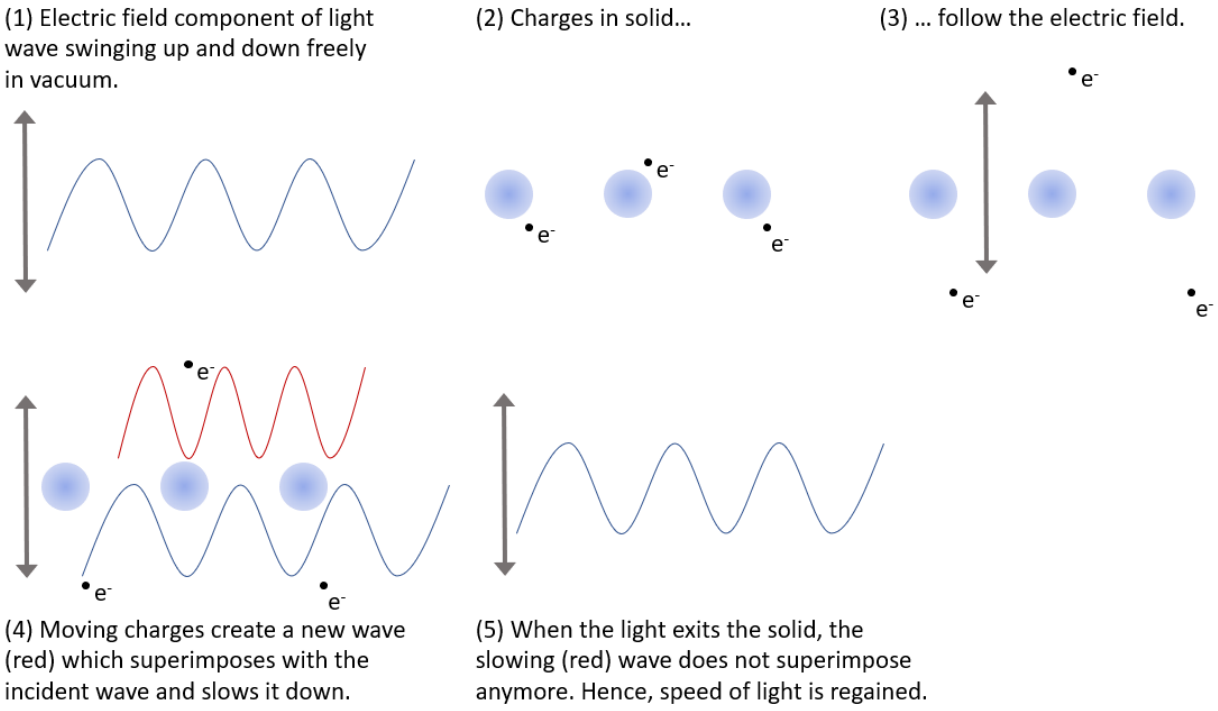

Figure 2.1-4: Process of slowing light in matter which yields the refractive index of a solid.

The superimposed wave in the material (incident plus created) shows a shorter wavelength but the same frequency. According to Eq. 7, if the wavelength λ decreases, the phase velocity v also needs to decrease to keep the frequency f constant.

$$\lambda = \frac{v}{f} \qquad \text{Eq. 7}$$

λ… wavelength; v…phase velocity; f…frequency

At first glance, one may think that if the wavelength λ is lowered, energy may rise due to Eq. 8. But it is also shown in Eq. 8 that the frequency is inversely proportional to the wavelength and energy is conserved.

$$E = \frac{hc}{\lambda} = hf \qquad \text{Eq. 8}$$

E…energy; h…Planck's constant; c…speed of light; λ… wavelength; f…frequency

When the light wave exits the material, no additional wave is superimposing anymore with the original wave and the original wave is again traveling with the speed of light (Figure 2.1-4 (6)).

Additional to the slowing of light in matter, Eq. 6 and Eq. 7 can be used to derive an important dependency of n. Eq. 7 can be reformed to yield a formula for the phase velocity v, which can be plugged in Eq. 6. This shows the dependence of n on the wavelength λ of the incoming light, hence $n = n(\lambda)$.

The Ewald-Oseen extinction theorem describes mathematically the change of phase velocity and hence the refractive index in matter.[25] The Maxwell's equations offer one way to derive it. As stated before, the electrons in the medium are creating a new wave which superimposes with the incident wave. The solution of Maxwell's equations for this case consist of the sum of two individual waves. One term describes the wave in vacuum which negatively interferes with the part of the new wave in the medium. Therefore, no wave with speed of light *c* is left in the medium. The second term is a wave in the medium which travels with a factor *n* slower than *c*.

From the negative interference of the waves in the medium and the creation of new waves by the oscillating electrons, one can conclude that light is extinct and recreated in the medium. A characteristic "extinction length" of matter can be defined, where the original light is completely replaced in matter. For example: visible light in air at sea level is completely exchanged at a distance of 1 mm.[26]

Furthermore, to slowing of light in matter extinction of some of the light intensity can happen within the material by absorption. In general, absorption in a semiconductor or an insulator can occur for photons with energies at least as high as the band gap. Photons with energies lower than the band gap cannot be absorbed. To give an example: SiO_2 (glass) is transparent for the visible spectral range (400 – 700 nm ≈ 3.1 – 1.75 eV) due to a band gap of 9 eV.[27]

Mathematically absorption can be described with a complex refractive index as shown in Eq. 9.

$$n^* = n + i\kappa \qquad \text{Eq. 9}$$

*n**… complex refractive index; *n*…real part of refractive index; *κ*…extinction coefficient

The complex refractive index *n** is a combination of the real refractive index *n* and its complex part the extinction coefficient *κ*. The extinction coefficient describes how much light intensity *I* of the incident light I_0 at material depth *z* is left (Eq. 10). Eq. 10 is called the Beer-Lamberts law.

$$I(z) = I_0 e^{-2\kappa\frac{c}{\omega}z} \qquad \text{Eq. 10}$$

I(z)…Intensity at material depth (z); I_0…incident intensity; *κ*…extinction coefficient; *c*…speed of light; *ω*…frequency; *z*…depth

The refractive index *n* and the extinction coefficient *κ* are material constants and can be determined by transmittance and absorption measurements. If *κ* equals zero, no absorption happens in the material. Another way to minimize absorption according to Eq. 10 is to minimize *z* by keeping the absorption length as short as possible (making a material as thin as possible).

A source of absorption in metals are surface irregularities which cover the entire surface. This effect is particularly important for metals which have plasma edges in the ultraviolet, e.g. silver. Micro irregularities cause scattering and absorption of the incident light by the excitation of surface

plasmons.[28] If thin metal films are used as TEs, it is important to achieve a low surface roughness to maximize transmittance.

The last optical quantity which is influenced by the refractive index and which also influences transmittance is reflection. Details on the interaction of light and solids are given in the next section.

2.1.3 Interaction of light and solids – transmittance, reflectance and absorbance

The previous section explained in detail the physical quantity refractive index. In this section, the influence of the refractive index on the interaction between light and solids will be explained.

Early descriptions of light were simplified to descriptions of light as rays. Light as rays belongs to geometrical optics. Geometrical optics treats light rays as straight lines which are reflected or refracted if interacting with matter. The law of reflection (Eq. 10) describes the ratio of the incident to the reflected angle which is the same as for a mechanical reflection:[29]

$$\theta_i = \theta_r \qquad \text{Eq. 10}$$

θ_i…incident angle; θ_r…reflected angle

The second part of geometrical optics deals with refraction. Refraction of light happens if light travels through a medium with refractive index n_1 and hits the boundary to another medium with refractive index n_2. In this case, the light changes its direction of propagation according to Snell's law (Eq. 11):[29]

$$n_1 \sin(\theta_i) = n_2 \sin(\theta_t) \qquad \text{Eq. 11}$$

θ_i…incident angle; θ_t…transmitted angle; n_1…refractive index of medium one; n_2…refractive index of medium two

A graphical description is given in Figure 2.1-5 where a light beam *I* (dark blue) falls on the interface between the two materials with refractive index n_1 (light blue) and n_2 (dark blue). The direction of the reflected light beam *R* as well as the direction of the transmitted light beam *T* can be calculated with Snell's law if the refractive indices are known.[29]

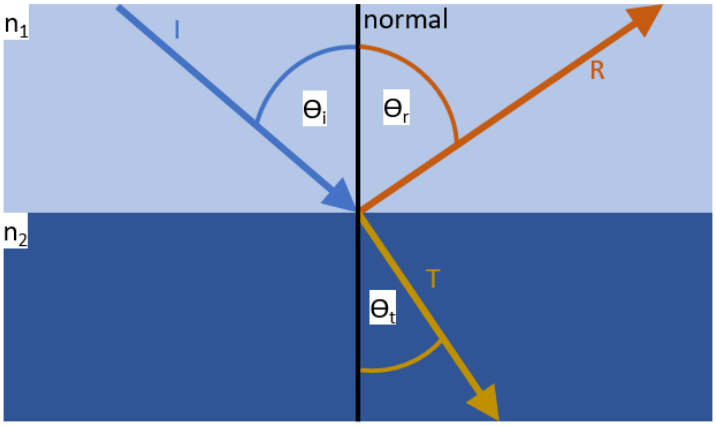

Figure 2.1-5: Relation between incident (*I*), transmitted (*T*) and reflected (*R*) light, while changing from optical media with refractive index n_1 to optical media with refractive index n_2. Depending on the relation of refractive indices and the angle of incidence, the angles of transmitted and reflected light change. Taken from [30] and modified.

A more comprehensive description of light is given by physical optics where additionally to the laws of geometric optics, the electromagnetic wave nature of light is considered. One important quantity of light as electromagnetic wave is polarization. The definition of polarization is shown in Figure 2.1-6. One speaks of p-polarization if the electric field of the light wave is swinging in the plane of incidence. If the electric field of the incident light is swinging perpendicular to the incident plane, one speaks of s-polarization.

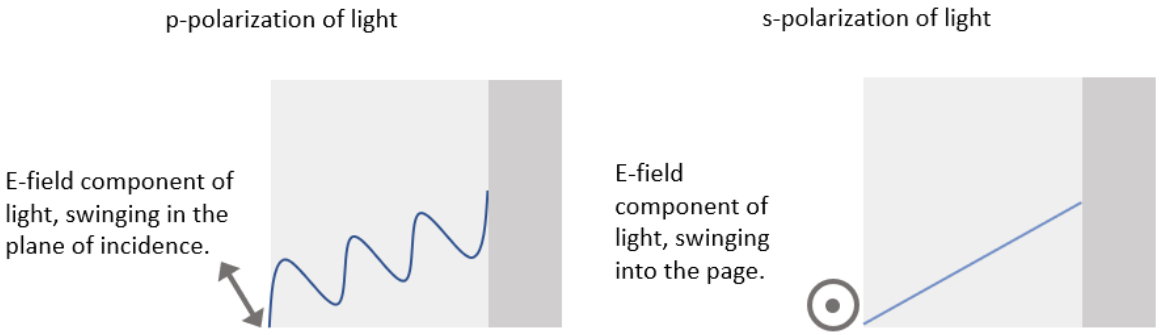

Figure 2.1-6: Definition of s- and p-polarized light waves.

The wave nature of light further leads to the effect of interference. Interference describes the superposition of two or more light waves. One distinguishes between positive and negative interference as shown in Figure 2.1-7. Positive interference occurs if electromagnetic waves add up their amplitudes (Figure 2.1-7 (a)) while negative interference is the case for amplitude extinction (Figure 2.1-7 (b)). Light intensity is proportional to the square of the amplitude, meaning that if the amplitude of a light wave is zero, no light exists and if the amplitude is higher more light is present.[31]

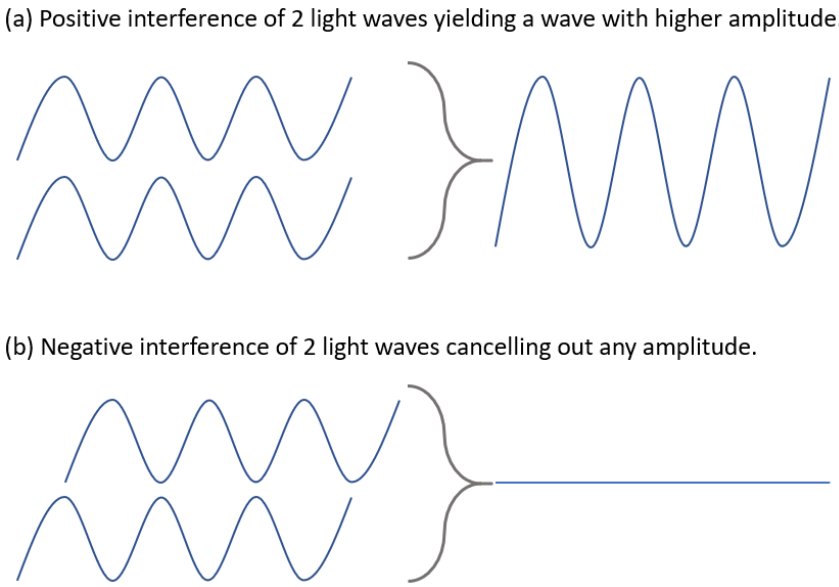

Figure 2.1-7: Positive interference of 2 light waves yielding one wave with higher amplitude (a); negative interference of two light waves yielding no light (b).

That said, interference is more related to power transfer of electromagnetic waves than to geometrical contemplation. Nevertheless, both phenomena occur simultaneously during light-matter interactions. For a deeper understanding of power transfer of electromagnetic waves between media with different refractive indices, consider the following set up: Light travels through an optical media with refractive index n_1, and hits the boundary to another media with refractive index n_2, as shown in Figure 2.1-8. In this simplified case, reflection and transmittance occurs.

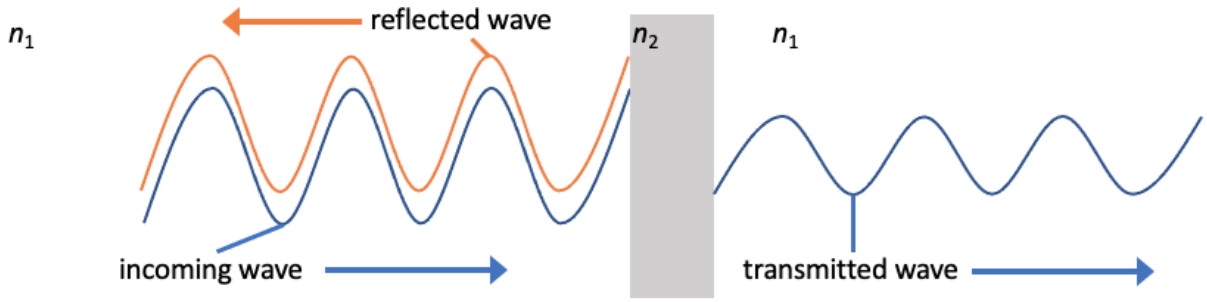

Figure 2.1-8: Schematic drawing of the amplitude relations of light hitting a transmitting thin film and being partly reflected and partly transmitted. (Absorption not drawn for simplification.)

Figure 2.1-8 shows how the amplitudes of light waves are influenced by refractive index changes in the light path (absorption not shown for simplicity). The transmitted and reflected wave show lower amplitudes equaling to lower light intensity. The factors of amplitude change can be calculated by Fresnel's equations.

Different polarization states of light result in different Fresnel equations for s- and p-polarized light (Eq. 12 – Eq. 15). The equations are given for two materials with the same magnetic permeability.[32,33] The factors for transmittance ($t_{s,p}$) and reflectance ($r_{s,p}$) only depend on the angle of incident and the

refractive index of the material. If the angle of incident is zero (light hitting the surface perpendicular), the factors only depend on the refractive indices because in this case, all the cosine terms equal 1. The reflectance factors become zero since the reflectance factors are only depended on the refractive indices and the refractive indices are equal ($n_1 = n_2$).

Therefore, it can be concluded that less light is reflected if light hits the boundary between two materials with similar refractive indices. On the contrary, more light is reflected if the difference between refractive indices is large. This observation is important for the creation of anti-reflective coatings and dielectric/metal/dielectric electrodes as will be shown later.

$$r_s = \frac{n_1\, cos(\theta_i) - n_2 cos(\theta_t)}{n_1\, cos(\theta_i) + n_2 cos(\theta_t)} \quad \text{Eq. 12}$$

$$t_s = \frac{2n_1 \cos(\theta_i)}{n_1 \cos(\theta_i) + n_2 \cos(\theta_t)} \quad \text{Eq. 13}$$

$$r_p = \frac{n_2 \cos(\theta_i) - n_1 \cos(\theta_t)}{n_2 \cos(\theta_i) + n_1 \cos(\theta_t)} \quad \text{Eq. 14}$$

$$t_p = \frac{2n_1 \cos(\theta_i)}{n_2 \cos(\theta_i) + n_1 \cos(\theta_t)} \quad \text{Eq. 15}$$

r_s… reflection coefficient for s polarized light; t_s…transmittance coefficient for s polarized light; r_p…reflection coefficient for p polarized light; t_p…transmittance coefficient for p polarized light

Note that $r_{s,p}$ and $t_{s,p}$ are the reflectance and transmittance factors. Absolute values for *R, A* and *T* of a material are given by: [32,33]

$$R = |r^2| \quad \text{Eq. 16}$$

$$T = \frac{n_2 \cos(\theta_t)}{n_1 \cos(\theta_i)} |t^2| \quad \text{Eq. 17}$$

$$T + R + A = 1 \quad \text{Eq. 18}$$

R…reflectance; *T*…transmittance; *A*…absorbance

The presented equations offer the possibility to calculate *T*, *R* and *A,* if the complex refractive indices of the materials are known. This is important for the later explained transfer matrix algorithm.

To measure transmittance, the simple relation given in Eq. 19 is valid. Transmittance is the relation of light intensity measured with a sample in the beam path to light intensity measured without a sample in the beam path. Since the refractive index is dependent on wavelength, *T* is also depending on the wavelength of the incoming light.

$$T(\lambda) = \frac{I(\lambda)}{I_0(\lambda)} \qquad \text{Eq. 19}$$

T…transmission; *I*…intensity measured with sample; I_0… intensity measured without sample

For reflectance measurements, a similar relation holds true (Eq. 20). However, reflectance measurements are done differently. R_0 is acquired by measuring the reflected light intensity of a mirror whose spectral reflectance is known. The sample to be measured replaces the mirror in the beam path. In contrast to the transmittance measurement, the reflectance spectra values need to be multiplied because the mirror is only reflecting a part of the original light source.

$$R(\lambda) = R_0(\lambda)\, R(\lambda) \qquad \text{Eq. 20}$$

R…reflectance; *R*…reflectance measured with sample; R_0… reflectance measured with reference mirror

From the measured *T* and *R* values of a single material layer, the complex refractive index can be calculated.

2.1.4 Calculation of optimized DMD layer thicknesses

As explained previously, metals are good conductors due to their large amount of highly mobile charge carriers. Unfortunately, the high amount of mobile charge carriers leads to high reflectance which inhibits high transmittance if metals are used as TE.

The reflectance is caused by the electrons in the metal which can follow the electric field of an incoming light wave. If the frequency of the incoming electric field is higher than the so-called plasma frequency of the electrons in the metal, the light wave can pass through as the electrons are unable to follow the electric field. Light with frequencies lower than the plasma frequency is reflected by the freely moving electrons. The formula for the plasma frequency is given in Eq. 21.

$$\omega = \sqrt{\frac{n_e e^2}{m^* \epsilon_0}} \qquad \text{Eq. 21}$$

n_e…density of electrons; e…the electric charge; m^*…effective mass of the electron; ϵ_0…is the permittivity of free space

If the effective mass of the electrons in the solid equals the free electron mass, the plasma frequency only depends on the density of electrons. Metals like Al or Ag have an approximate charge carrier (in this case electrons) density of 10^{23} cm^{-3}. Putting this value in Eq. 21, it yields a plasma frequency for metals in the UV region. This leads to the strong reflection of visible light which makes metals shiny. This reflectivity needs to be suppressed if metals are applied in a TE as transparent thin film. As shown in section 2.1.3, reflectance is influenced by the change of refractive index in the light path.

If a metal is sandwiched between two dielectrics in a dielectric/metal/dielectric architecture, the refractive indices and layer thicknesses of the dielectrics can be chosen that the overall reflectance interferes destructively as shown in Figure 2.1-9.

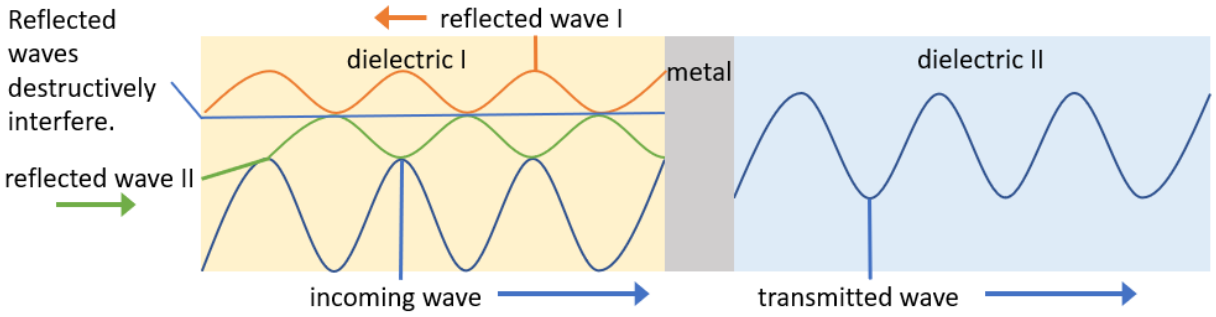

Figure 2.1-9: Schematic of the principle idea of a DMD electrode: an incoming light wave travels through dielectric I, hits the metal and is partly reflected (orange wave). The partly reflected wave is reflected at the dielectric I / air interface and creates the reflected wave II (green wave). The thickness of dielectric I needs to be chosen to assure destructive interference of the reflected waves I and II. The same is valid for the metal and the dielectric II but not drawn in this figure for reasons of simplicity.

Destructive interference of the reflected light waves must lead to higher transmittance due to energy conservation as shown in Eq. 18, since the absorption term in Eq. 18 is a material constant, depending only on film thickness and frequency of incoming light.

For the fast estimation of the optimized layer thicknesses of given dielectrics to form a DMD stack, optical simulation is a powerful tool. The so-called transfer matrix method (TMM) is a widespread algorithm for the optical simulation of stratified media and was also used in this thesis. In the following, a short introduction into the basic concept of TMM is given.

The given Fresnel equations of section 2.1.3 describe the fraction of light intensity transmitted, absorbed and reflected at an interface between two media. If there is more than one interface, multiple reflections and transmittances occur. For example: in Figure 2.1-10, light hits the first interface and is partially reflected (R_1) as well as partially transmitted (T_1). The partially transmitted light beam (T_1) is again partially reflected (R_i) and transmitted (T_i) at the second glass air interface. The partially reflected beam in the glass is partially reflected and transmitted another time at the first interface and so on (not shown).

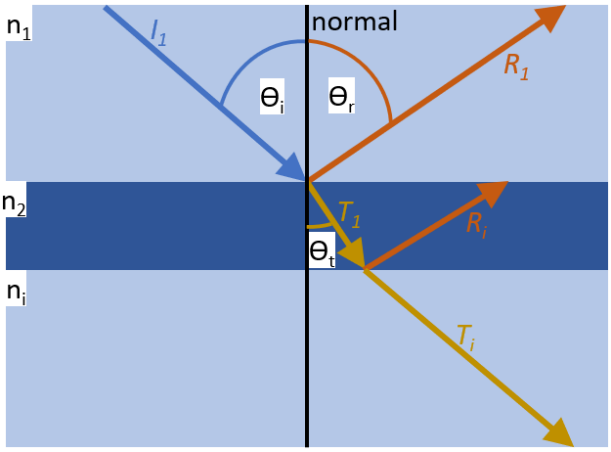

Figure 2.1-10: The figure shows the geometric contemplation of multiple transmissions and reflections in stratified media. Light beam I_1 hits the boundary between media with n_1 and n_2. This creates the light beams R_1 and T_1. T_1 creates R_i and T_i at the second interface. R_i can destructively interfere with R_1 leaving all the light either absorbed or transmitted. Taken from [34] and modified.

Depending on the thickness and the refractive index of the layers (in this sample the dark blue layer (Figure 2.1-10)), destructive or constructive interference can occur (see additional Figure 2.1-9). Infinite reflections and transmittances at the interfaces form the overall transmittance and reflectance of the layer sequence.

According to Maxwell's equations, the electric field across the boundaries from one medium to the next show simple continuity conditions. Hence, the field at the end of a layer can be calculated in a transfer matrix operation if the field is known at the beginning of the layer.[35,36]

This formalism was reformed to calculate the optimized layer thicknesses of the dielectrics, with given n and κ. The metal thickness was kept constant at 10 nm to have a good trade-off between transmittance and sheet resistance. In the simulation, an electromagnetic wave hits the DMD stack with starting values for the thicknesses of the dielectrics. Within the transfer matrix calculation, the Fresnel's equations from section 2.1.3 are used to estimate the new reflected and transmitted waves. For the use in the transfer matrix algorithm, the complex index of refraction $n^* = n + i\kappa$ is used instead of only using n. The reason for this is to take extinction into account. These steps are repeated until T is maximized for new d values for both dielectrics. The software was originally written by Dr. Bauch and realized in the programming language Python.

The simulation did not only yield the new thickness numbers but also a heat map to graphically illustrate the optimized layer thicknesses. The heat map visualizes the size of the sweet spot of dielectric layer thicknesses. For instance, if the sweet spot for two given dielectric thicknesses is large, the error in layer thickness production does not account so heavily, whereas if the sweet spot is small, it is more important to achieve the given dielectric layer thickness.

2.2 Transparent electrode concepts and materials

Modern optoelectronics such as flat panel TVs, e-readers, smart phones, smart glasses, touch screens, organic light emitting diodes (OLEDs) and organic photovoltaics rely on transparent electrodes (TEs).[12,37–40] TEs assure light interaction of the active layers (light emitter or absorber) while simultaneously offering the possibility of charge carrier exchange (injection or extraction). The basic two principles to make materials transparent and conductive are either to search for materials which are intrinsically good conductors and light transmitters or to make good conductors thin enough or mesh-like to transmit light. In the mesh-like case, the ratio of conductors to free space needs to be chosen wisely to guarantee homogenous charge carrier exchange over the area as well as isotropic light transmittance.

2.2.1 Transparent metal and oxide thin films

The most straight-forward idea to make a conductive material like a metal transparent is to make it thin enough to minimize Beer-Lambert extinction but still feature high enough conductivity. Metals like Ag, Cu, Au or Al with thicknesses between 5 and 15 nm showed reasonable results.[10,41–46]

To avoid the high reflectance from metals (as explained in section 2.1.4) another material class can be used. Semiconductors for example do not show high reflectance in the visual spectral range because their electron densities are generally lower compared to metals. Semiconductors also display low absorbance for photons with energies lower than the band gap. If the band gap is larger in terms of energy than the energy of an incoming photon, the photon will not be absorbed. A drawback of semiconductors is that their charge carrier density is in general lower than in metals. To work around the low charge carrier density, semiconductors used for TEs are intensively doped.

One example for a heavily doped wide band gap (3.7 eV) semiconductor is ITO.[10] ITO belongs to the class of transparent conductive oxides (TCOs). Other TCOs include fluorine-doped tin oxide (FTO), aluminum-doped zinc oxide (AZO) or solution processed metal oxides.[47,48]

Since ITO represents 97 %[49] of the USD 4.2 billion market, it is the main competitor on the TE market and will be discussed in detail. ITO consists of 74 % indium which is very scarce which leads to high prices for the electrodes.[50] Doping of indium oxide with tin oxide produces charge carrier densities in ITO from up to 10^{20} cm^{-3}, which is close to the density of metals. Although the charge carrier density is high, it is three orders of magnitude below metals leaving ITO with a plasma frequency in the infrared. Therefore, ITO does not reflect visible light.[51]

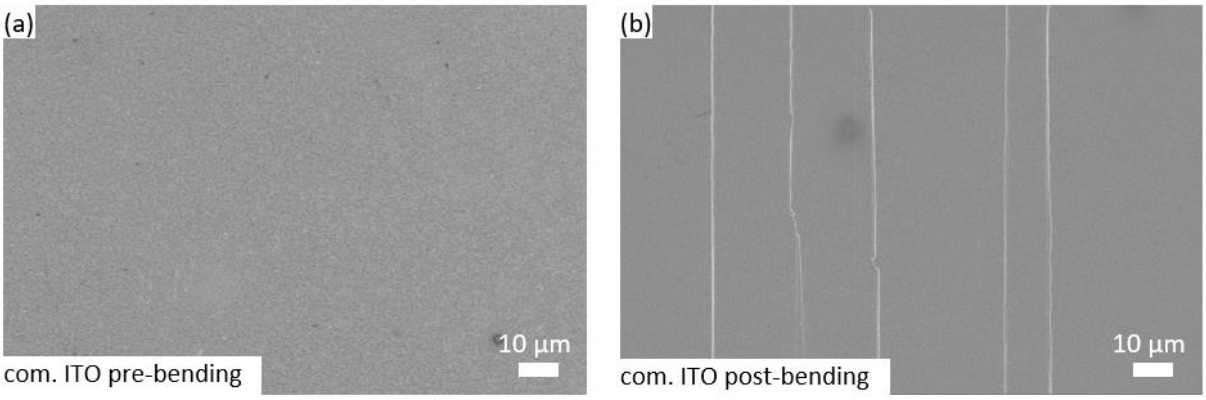

Figure 2.2-1: SEM images of commercial ITO deposited on PET initial surface (a) and surface after 70 compressive bending cycles (b), showing crack formation in the ITO which hampers conductivity. Taken from [52] and modified.

ITO became an industrial standard for TEs because of its high transmittance in the visible spectral range (<80 %) together with a low sheet resistance if deposited on glass.[12] Nevertheless, the trend in industry goes towards production on flexible substrates because roll-to-roll production offers faster production speeds than traditional bulk production of inorganic semiconductor devices like silicon solar cells.[53]

Yet, ITO fails to have a low sheet resistance on PET due to the lower possible substrate temperature and the unattainable high deposition rates which are necessary to achieve high conductivity during the sputtering process.[12] The R_{sh} of ITO on PET is therefore quite high (usually >40 Ω/sq). On PET, ITO is usually applied as an amorphous thin film, which is brittle. As shown in Figure 2.2-1, ITO gradually develops cracks upon repeated bending cycles. As a consequence, its resistance rapidly increases.[54–56] This fact makes it a bad competitor for flexible applications.[57] In terms of optical losses, the PET/ITO interface shows high internal reflections due to waveguide trapping of internally emitted light in ITO/organic layers, which decreases overall transmittance.[58]

The long list of drawbacks of ITO as flexible TE can be taken as a list of requirements for a potential competitor. Such a potential competitor to ITO uses the advantages of both, metals and TCOs in so called dielectric/metal/dielectric sandwich structures. Due to the metal layer in the middle of the stack, DMD electrodes offer high mechanical flexibility and do not require high temperatures during processing to achieve high conductivities.[59] As dielectrics TCOs such as ITO, (doped) ZnO, TiO_x, MoO_3 and WO_3 are used.[41,45,60] As metals, Ag, Au and Cu are predominantly used. In DMD electrodes, the R_{sh} is mainly determined by the metal and its thickness, while the transmittance is determined by the overall layered structure. A schematic of such a structure is shown in Figure 2.2-2.

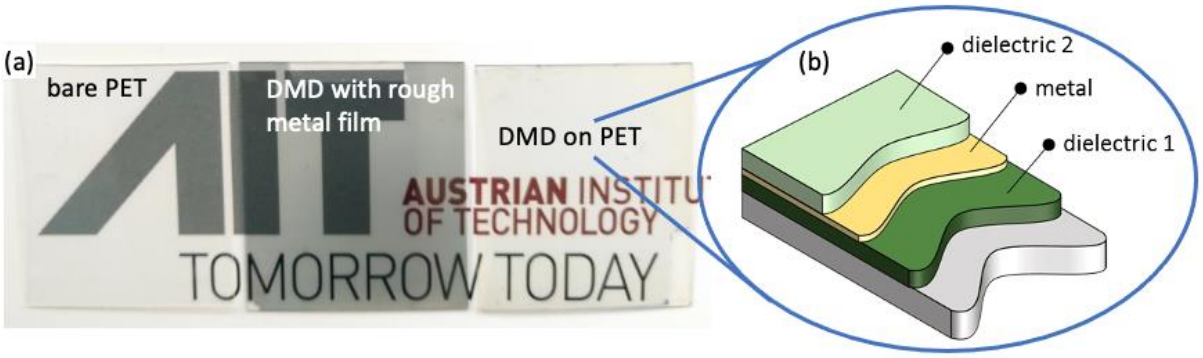

Figure 2.2-2: Images of a bare PET foil, a PET foil covered with a non-closed Ag layer and is therefore dark and a PET foil sputtered with an optimized DMD stack (a) and schematic of dielectric/metal/dielectric sandwich electrodes (b). Taken from [61] and modified.

As visible in Figure 2.2-2 (b), a metal is placed between two dielectrics. By choosing the dielectric material and thickness in an optimized way, the reflection of the metal is suppressed. This phenomenon is explained in section 2.1.4. Ambient-temperature deposition, mechanical stability[10,45,62,63], low roughness[41] and temperature stability[43] are valuable features of this TE class. Properties of DMD electrodes are summarized in a number of reviews.[64–66,12]

An additional advantage of DMD electrodes is, that the electrode work function can be adapted to specific device energetics through the selection of a suitable dielectric layers, as these span over a wide range of electron affinity and ionization potential values.[67,68] Additional materials can be chosen under the light of abundance (price) while keeping a high transmittance by adjusting the layer thicknesses according to its refractive index. Details of the state of the art DMD electrodes as well as intensive literature research will be given in chapter 4. Furthermore, chapter 4 deals with the experimental approach of achieving a superior TE by the use of sputtered DMD films and implementing it in an organic light emitting diode.

2.2.2 Metal nanowires

Thin metal films - either on their own or in a DMD electrode - are not the only way to implement metals as TEs. Instead of using a closed metallic film, one could apply a randomly oriented micro mesh of metals. The idea is basically similar to the idea of using thin metal films: take a good conductor but instead of making it very thin, make it transparent by the empty spaces between it. Such randomly oriented conductive micro meshes can be achieved by metal nanowires.

Sun et al. developed a polyol synthesis process for silver nanowires in 2002[69], first investigations for the use of silver nanowires as transparent conductive electrodes were performed by Lee et al. in 2008.[70] Since then, various optoelectronic devices incorporating metal nanowires as transparent electrodes have been shown in the literature.[71–74] So far, the performances of NW thin films rival already those of ITO.[50]

To deposit silver nanowires on a substrate, many different deposition techniques such as drop casting[74], spin coating[75], inkjet printing[76], bar coating[77,78] or spray coating[79,80] have been presented. In this thesis, spray coating was chosen as depositing technique as it features R2R scaling potential. Samples of silver nanowire films either on glass (a) or on PET (b) are shown in Figure 2.2-3.

Figure 2.2-3: Silver nanowire films on glass (a) and on PET (b), produced by spray coating during this thesis.

NW films feature high transparency (90-96 %) as well as low R_{sh} (9-70 Ω/sq).[81] Additionally to this possible outstanding optical and electrical properties, nanowires show excellent mechanical stability in bending which makes them a good choice for flexible and R2R processed electrodes.[82]

Nevertheless, NW films show some drawbacks such as the need for post deposition treatments to minimize contact resistance[83,84], high roughness[12] and poor adherence to flexible substrates[85].

The need for post deposition treatments arises from the production of silver nanowires. Most silver nanowires on the market are produced by polyol synthesis developed by Sun et al..[83] During synthesis, an organic capping layer arises around the nanowires which have a high specific surface area and are hence prone to oxidation of the metal. This organic capping layer around the wire inhibits metal-metal contact which decreases the conductivity significantly.[70] To get rid of the capping and to weld the wires together to increase wire to wire conductivity, different post deposition treatments like heating[40],

plasmonic flash light welding[86] or chemical treatments like HCl vapor[87] have been introduced. The post deposition issue is especially critical to overcome as the most common flexible and transparent substrate is PET. PET has a glass transition temperature of 70 °C which hampers heat intensive processing.[88] Various workarounds and the approaches tested in this thesis as well as further literature research will be given in chapter 5.

2.2.3 Metal grids and carbon based transparent electrodes

A similar idea to NWs as TE in terms of a conductive mesh are metal grids. Grids can be fabricated photolithographically, inkjet printed and electro plated.[52] Depending on the type of deposition, grid structures can vary from 2 µm line width and grid spacings of 10 µm for photolithographic grids[92], up to 150 µm line width and 8 mm spacing for inkjet printed grids[8,37,93,94]. Inkjet printed grids are shown in Figure 2.2-4 (a). (Figure 2.2-4 (b)) displays the implementation of inkjet printed grids in OLEDs.[8]

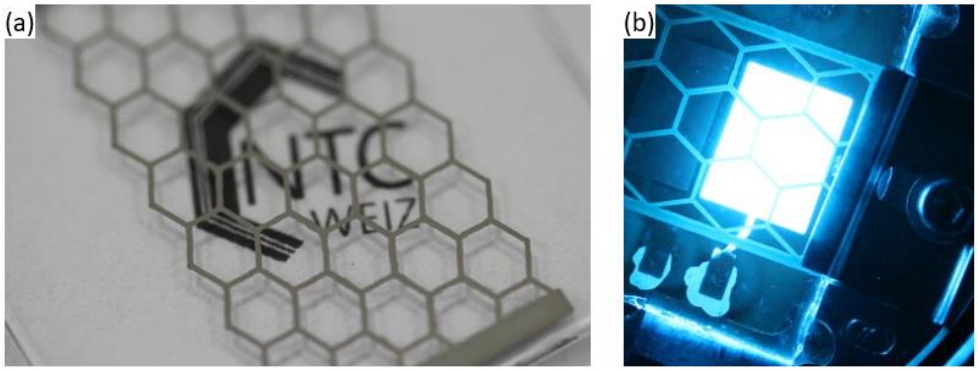

Figure 2.2-4: Inkjet printed metal grids on glass (a) and inkjet printed metal grids implemented as TE in a blue OLED (b). Taken from [8] and modified.

Grid structures with larger spacings in between them have shown the need for a conducting polymer to guarantee homogenous conductivity over the whole electrode surface. Such a conducting polymer which is widely applied in organic electronics and which has even been used as standalone TE is poly(3,4-ethylenedioxythiophene) polystyrene sulfonate (PEDOT:PSS).

PEDOT is a conjugated polymer on thiophene basis. PSS is an isolator but mixed with PEDOT for doping to achieve electrical conductivity in thin films. PSS is very acidic, which leads to a pH value of approximately 1.5-2.5 for most PEDOT:PSS solutions. This can cause problems if PEDOT:PSS is applied on surfaces prone do acids for example AZO.[95]

Various deposition methods for the application of PEDOT:PSS thins films such as spin coating, inkjet printing, screen printing and spraying have been presented.[96] Depending on the demands on the PEDOT:PSS layer (coating technique, conductivity, work function), various formulations of the solution exist.[97]

Carbon forms the base of organic conductors not only in polymers like PEDOT:PSS but also in Graphene. Graphene is a perfect monolayer of carbon atoms. The carbon atoms are arranged in hexagons. Solving the Schrödinger equation for the carbon atoms arranged in this pattern shows that graphene is a zero band gap semiconductor which comprises electrons delocalized over the whole molecule offering the possibility to conduct electrons without scattering.[98] Combined with possible doping of graphene, this leads to high in plane conductivities.[99]

Sheet resistances of up to 800 Ω/sq are in contrast with the high in plane conductivity of graphene. The high sheet resistance is caused by the fact that so far, solution processed graphene films consist of thousands of graphene flakes (Figure 2.1-1) building up grain boundaries, high contact resistance and showing many defects. Nevertheless Wu et al. already showed that solution processed graphene films deliver OLED performances comparable to ITO.[100]

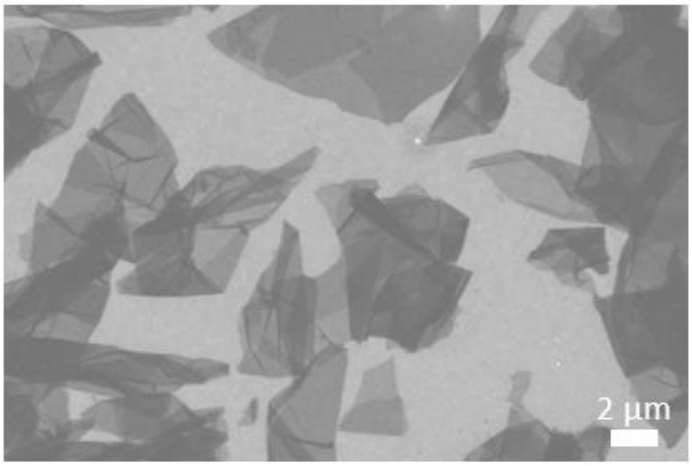

Figure 2.2-5: SEM images of graphene flakes (dark sheet like wrinkled structures) spin coated from solution on a glass/ITO substrate (light background).

Although not used in this thesis, carbon nanotubes (CNT) are mentioned as an approach for TEs in the scientific community. Carbon nanotubes are rolled up graphene flakes. Carbon nanotubes have already been successfully applied in displays and photovoltaic devices as transparent electrodes.[53-55] Important for the application of CNTs as TEs is that the concentration of CNTs needs to be high enough to build a percolation network similar to nanowires.[104]

2.3 Organic light emitting diodes

Since the last three decades, organic light emitting diodes march steadily towards commercialization. The possibility to create flexible, lightweight, portable, wearable and flexible lighting and display applications makes OLEDs a unique device for the consumers market.[57] Due to the broad industry applications of OLEDs, they were chosen as a testing device for the developed TEs.

Additionally, the OLED was chosen as testing device for TEs because of its susceptibility to electric field inhomogeneities caused by inhomogeneous electrodes. If the electric field between the two electrodes is inhomogeneous, charge carrier injection will be inhomogeneous. This leads to inhomogeneous light emission and higher shunt failure rate as the light emitting material is inhomogenously stressed.[92,105–107] This chapter gives a short introduction on the physical background of organic electroluminescence and the state of the art in OLED designs.

2.3.1 Charge carrier injection and light generation

Section 2.1.1 described the formation of electronic bands in solids. One sort of the presented materials are semiconductors. Semiconductors show an energy gap between the conduction and the valence band. If holes (charge carrier in the valence band) and electrons (in the conduction band) recombine in a semiconductor, a photon can be created.

In an OLED, the valence band corresponds more or less to the highest occupied molecular orbital (HOMO) and the conduction band to the lowest unoccupied molecular orbital (LUMO). Details on the differences between inorganic and organic semiconductors are left out as they are out of scope of this thesis.

In the easiest set-up for an OLED, the organic semiconductor material is sandwiched between two electrodes. In the examples shown in Figure 2.3-1, the organic semiconductor (OSC) is sandwiched between cathode and anode. Figure 2.3-1 (a) shows the OSC, the anode and the cathode in the so called flat band regime. The flat band regime represents the OLED under a small enough forward bias to flatten the LUMO and the HOMO.

Figure 2.3-1 (b) shows the same relations under an applied forward bias. This bias causes an increased potential at the cathode side and a subsequent alignment of the energy levels in the device. Important to notice is that the work functions of the materials stay constant. The lowest unoccupied molecular (LUMO) and the highest occupied molecular orbital (HOMO) also align according to these circumstances.

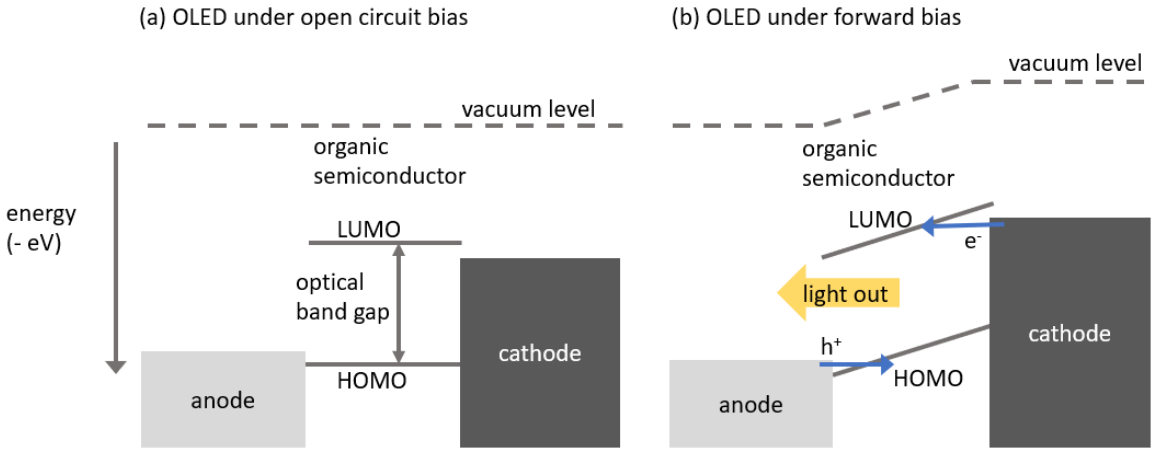

Figure 2.3-1: Energy levels of materials in a regular OLED architecture, the device is turned off, small energy barriers arise between anode and HOMO and cathode and LUMO which inhibit charge carrier injection (a). OLED under forward bias (turned on), blue arrows symbolize injection of electrons (e^-) and holes (h^+) via tunneling, e^- and h^+ travel along the electric field between anode and cathode until they recombine under the emission of light (yellow arrow) (b). Taken from [12] and modified.

The alignment leads to the formation of a triangular shaped energy level alignment (Figure 2.3-1 (b), right top and left bottom). Through this triangular shaped energy barrier, electrons and respectively holes can be injected via tunneling (blue arrows) into the OSC. Injected holes and electrons move along the active layer under the influence of the electric field until they come close enough for Coulomb interactions and form an exciton.[108] From the exciton state, the electron and hole can recombine under the emission of light (yellow arrow). The energy of the photon is proportional to the size of the bandgap.

The voltage current characteristic of an OLED gives information on the rectification of the device. A theoretical current density-voltage-luminance (JVL) characteristic is shown in Figure 2.3-2. An exponential increase from the turn on voltage under forward bias is desired. Under backward bias, the current should be as low as possible. If not, this is an indicator for shunts through the light emitting layer. For the same reason, the current in forward bias should be as low as possible until the turn on voltage. The turn on voltage is extracted from the luminance measurement (Figure 2.3-2) (in this thesis the bias at which 10 cd/m^2 are emitted from the OLED). A low turn on voltage indicates a smooth energy band matching of the different layers of the device and results in efficient charge carrier injection.

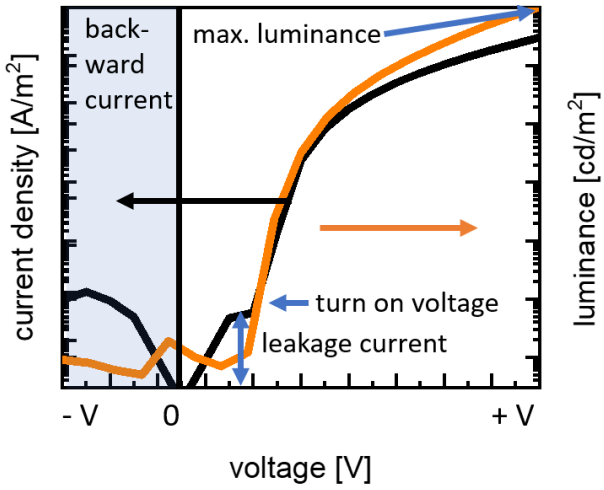

Figure 2.3-2: Theoretical JVL characteristic of an idealized OLED device. The black line shows the electrical current flowing through the device under forward bias. Up to the turn on voltage, the current should be low as otherwise the device is shunted. An exponential increase at the turn on voltage under the emission of light (orange line) is desired.

The current efficacy of an OLED can be calculated by dividing the luminance values by the current density values and is a quantity of the efficacy of the device. A more precise device efficacy is defined by the power efficacy, which takes the bias at which the OLED operates into account. Power efficacy is given in lm/W.

2.3.2 Device architectures

At the moment, two types of OLED architectures exist in the literature: regular and inverted (see Figure 2.3-3 for a schematic drawing). The set up where the bottom electrode is the anode and the top electrode is the cathode is referred as regular architecture (Figure 2.3-3 (a)). The OLED has an inverted architecture if the bottom electrode is the cathode and the top electrode the anode (Figure 2.3-3 (b)).

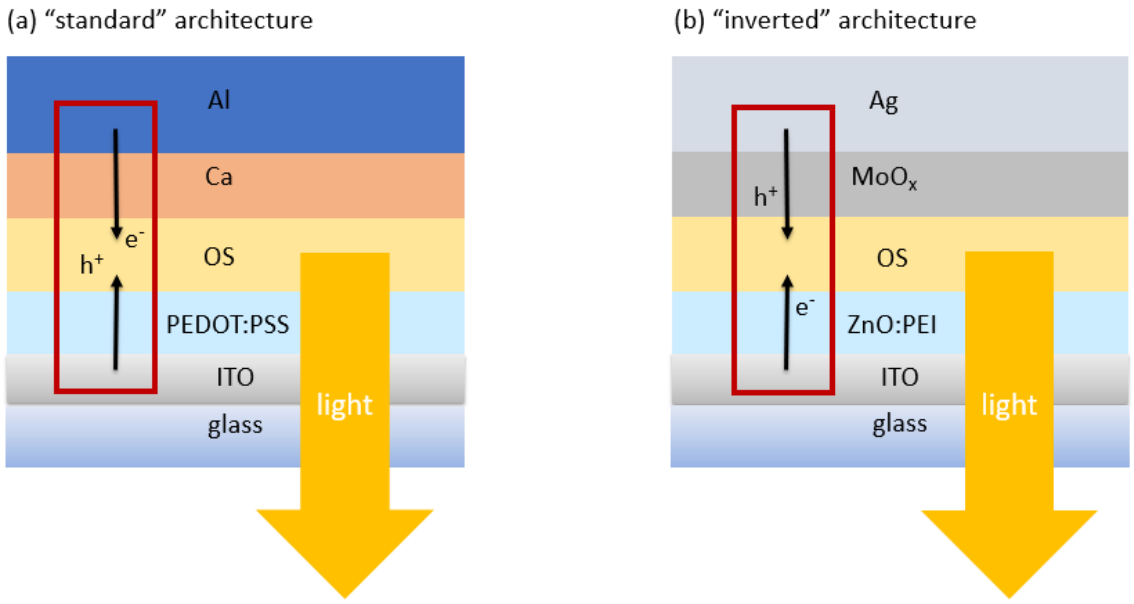

Figure 2.3-3: Schematic representation of a bottom emitting OLED in regular architecture (holes are injected from the bottom and electrons from the top) (a) and inverted architecture (holes are injected from the top and electrons from the bottom) (b).

In the most usual case of a regular architecture bottom emitting OLED, ITO coated glass is spin coated with PEDOT:PSS as hole injector (anode) and finished with the Al/Ca layers (cathode) as electron injector on the top. Within the OSC layer, holes and electrons recombine to light (yellow arrow). Details on the energy levels in the device and the light creation mechanism are shown in the previous section. This architecture features some drawbacks. A standard PEDOT:PSS solution has a pH value of 1.5-2.5; the underlaying electrode needs to withstand this acidity.[109] A further drawback of PEDOT:PSS is its loss of conductivity under moist conditions as it is usually dissolved in aqueous solutions. On the electron injecting side of the device, Ca features a drawback. Ca is a very reactive metal because of its low work function. This makes the device prone for degradation.[110]

In a bottom emitting inverted architecture device (Figure 2.3-3 (b)), the layers for hole and electron injection are exchanged. Holes are injected from the top electrode and electrons are injected from the bottom electrode. In this case, low work function materials are needed at the bottom electrode, hence PEDOT:PSS is replaced for example with ZnO nanoparticles (ZnONP). In this thesis, the ZnO nanoparticle solution is mixed with polyethylenimine (PEI) before spin coating the layer to further improve electron injection into the OSC.[110,111]

On top of the OSC, a high work function material such as MoO_x is applied to guarantee hole injection. The inverted device architecture features some benefits over the regular architecture. Due to the use of ZnO, the OS is already embedded between two oxides which work as encapsulation material since they are not prone to oxygen, which enhances device stability. Furthermore, the inverted structure matches the state of the art active matrix display technology with its n-channel transisitors.[111] In terms of processability, a ZnONP:PEI solution has advantages over a PEDOT:PSS solution due to its pH neutrality and the fact that it can be dissolved in IPA.

3 Experimental techniques

"Do or do not. There is no try." – Master Yoda

The chapter at hand deals with the experimental methods used in this thesis. First, the deposition methods for thin films which were used to deposit different material types with corresponding physical properties are explained. After a successfully thin film deposition, in depth characterization of the various films is crucial to understand the influence of deposition parameters on morphology, conductivity and transparency. In the second part of this chapter, a detailed explanation of the necessary characterization methods and the conclusions which can be drawn, is given. Besides the presentation of deposition and characterization techniques, the process steps for OLED fabrication are shown and explained.

3.1 Fabrication methods

For the creation of transparent electrodes, many approaches have been put forward. The most widely used processes in industry at the moment are vacuum based, including evaporation and sputtering, depending on the materials.[112] Large research effort has been put forward to develop solution processed methods and materials as an alternative. In this thesis, both approaches were used to develop different sorts of transparent electrodes as both deposition techniques feature distinct pros and cons. Therefore, first vacuum-based and later solution-based processes used in this thesis will be discussed. Prior to depositing thin films on transparent substrates, different cleaning steps are necessary to avoid contamination of the deposited thin film material.

3.1.1 Substrate cleaning

Independent of deposition method, thin film growth is influenced by the surface the material is applied on. For physical vapor deposition methods (i.e. sputtering), the surface energy can strongly influence homogenous film growth because the surface energy influences surface diffusion of arriving particles. For instance: if the surface diffusion is hindered because particles stick at the place where they arrive, film growth can become columnar. This leads to a rough and inhomogeneous film with low conductivity and transparency in a TE.

Similar influences can be observed for solution processed materials. For example: if the surface energy of a transparent substrate is high, solutions applied on the substrate form droplets on the surface and do not disperse over the surface. If this is the case, materials solved in the solvent are inhomogeneously distributed over the surface. This leads again to rough films that tend to inhomogeneous conduction and low transparency. [113]

Obviously, a surface must be free of any residual contaminations and have the same surface energy configuration to make experiments in thin film deposition reproducible. To achieve this, glass and PET samples were cleaned as follows: 25 × 25 mm^2 glass substrates (Menzel Gläser) or for OLED production 1 mm-thick glass substrates (Ossila), pre-cut in 20 × 15 mm^2, were cleaned in a 2 % Hellmanex III (Hellma Analytics) - ultrapure water solution in an ultrasonic bath, then rinsed with ultrapure water and sonicated in acetone and isopropanol.

The PET substrates (Melinex® 504 with one side treated for adhesion by the manufacturer) and polyimide (Kapton® HN Dupont) foils were first cut into 25 × 25 mm^2 pieces and then cleaned in the same way as glass, except for the acetone sonication. For flexible OLED applications, PET and Kapton® foils were cut into 20 x 15 mm^2 pieces. Both glass and PET substrates were dry-blown with compressed nitrogen. In all experiments, the films were deposited on the adhesion-promoting side of the PET foil.

3.1.2 Sputtering

In terms of fast processing, accurate film thickness control, broad material choice, control over stoichiometry, film smoothness and film adhesion sputtering is a powerful deposition technique to achieve high quality thin films. Generally, sputtering describes the bombardment of a "target" material with ions (primarily of a noble gas). This leads to the ejection of target atoms from the surface of the solid-state body. These atoms than can than be adsorbed on a substrate and start growing a film there. A schematic of sputtering is shown in Figure 3.1-1.

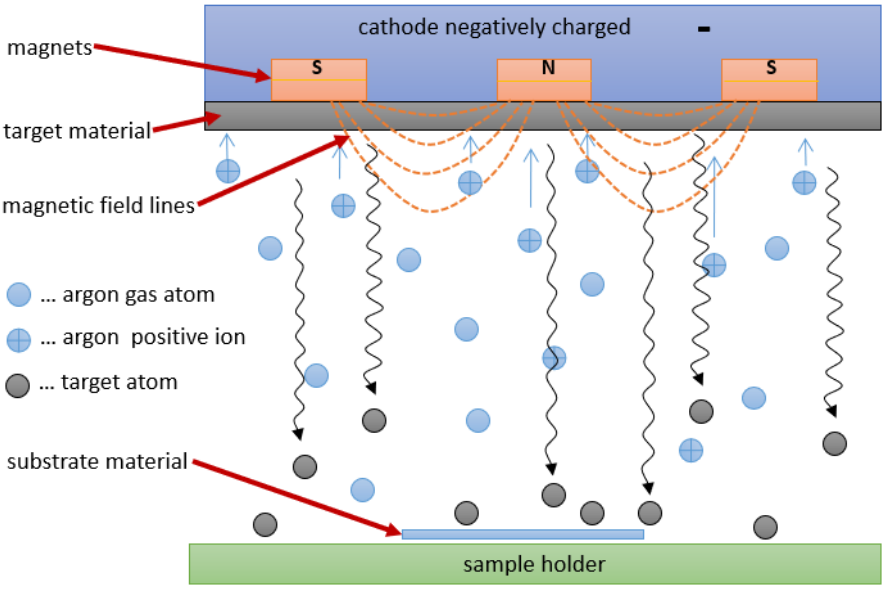

Figure 3.1-1: Schematic of magnetron sputtering. The negatively charged cathode is at the top and attracts positively charged Ar ions, which bombard the target material in front of the cathode and shoot out target atoms. Target atoms condense on the substrate material on the sample holder (bottom). To keep charged particles close to the target material, magnets are embedded in the cathode. Taken from [114] and modified.

In the work for this thesis, all sputtered materials were sputtered in direct current (DC) mode with Ar or Ar/O_2 (for reactive sputtering, as explained later) as sputter gas. In DC mode, a DC potential is applied between substrate and target. The target has a negative and the substrate a positive potential. The Ar atoms are ionized in the electric field by collisional ionization. The Ar ions are positively ionized; this leads to an acceleration towards the target. There, Ar^+ ions collide with the target atoms as shown in Figure 3.1-1. If the energy of the incident Ar^+ ion is higher than the binding energy of the target atom, an atom is ejected from the target surface.[115] The whole process takes place in a vacuum chamber to make the mean free path of the particles long enough to overcome the target to substrate distance. Due to the low pressure, the electrons and ions form a sputter plasma.

Additionally, to the electric field, a magnetic field is arranged behind the cathode (Figure 3.1-1). This form of sputtering is called magnetron sputtering. Due to the magnetic field, electrons are bound by Lorentz' forces to a circular movement over the target. This circular movement enhances the collision

probability between electrons and Ar atoms close to the target. An enhancement of the sputter rate at constant pressure can be achieved.[115]

A special form of DC sputtering is reactive sputtering. Reactive sputtering can be used to create different oxide or nitride films of a pure metal target depending on oxygen or nitrogen concentration in the sputter gas during sputtering. In this thesis, reactive sputtering with oxygen was used to create TiO_x. The reactive gas atoms can react with the target material, with target atoms in the plasma or with target material on the substrate to form new compounds, in this case oxides.[115]

A major drawback of DC sputtering is that it is only applicable for materials with sufficient conductivity. For electrical insulators, radio frequency (RF) sputtering exists as one form of sputtering. In this mode, instead of a DC field, a high frequency alternating field is applied between target and substrate. A capacitor is connected in series to keep the plasma neutral and cut off the DC part. Due to the alternating field, electrons and ions are accelerated in opposite directions. As a consequence of the much higher ion mass compared with the electron mass, ions cannot follow the changing electric field anymore from frequencies higher than approximately 50 kHz. Electrons move in the plasma area and collide more often with Ar atoms compared to DC mode. A superimposed offset potential accelerates the ions towards the target where the material is sputtered off. Because of the higher collision rate in the plasma area, the rate for RF sputtering is kept constant for lower pressures, giving the possibility to change film morphology.[115]

The sputter system used in this thesis is visible in Figure 3.1-2. It is a Leybold Univex 450C cluster tool.

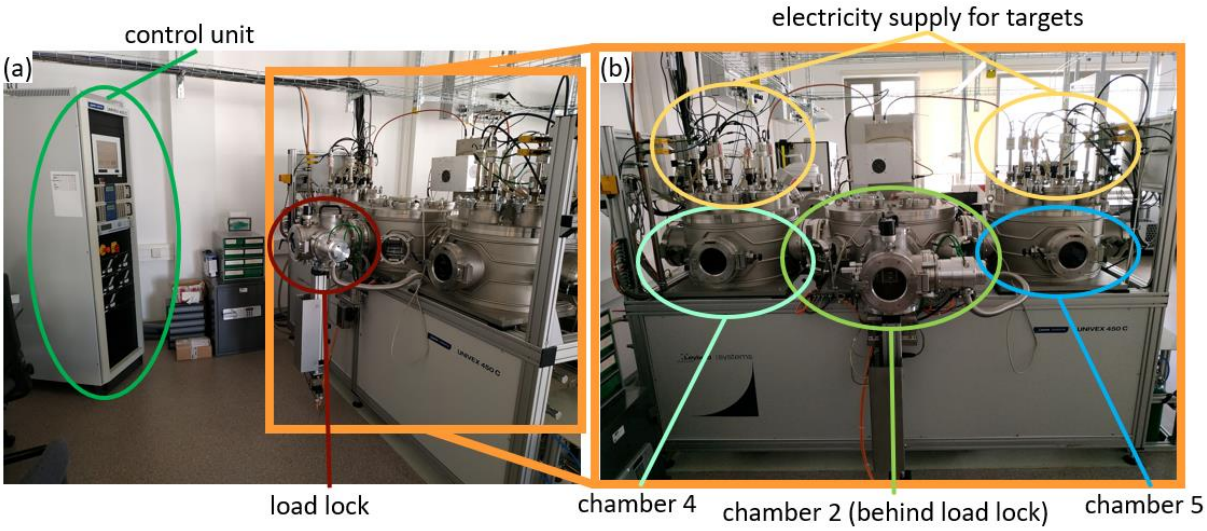

Figure 3.1-2: Side view of Leybold Univex 450C cluster tool with control unit and load lock (a). Front view of the various chambers of the sputter tool (b).

The cluster tool is controlled via the control unit in Figure 3.1-2 (a). Sample substrates are brought in via the load lock. The load lock is separated from the chambers by the so-called gate valve. This makes it possible for chambers 2, 4 and 5 (Figure 3.1-2 (b)) to be constantly under vacuum while the samples

can be changed. In chamber 2, a robotic arm is mounted which brings the substrates to the desired chamber. The chambers are separated from each other by gate valves to avoid contamination during sputtering. Sputtering targets are only mounted in chamber 4 and 5 where one can also see on top the electricity supplies for the process (Figure 3.1-2 (b)).

In the case of this thesis, TiO_x was sputtered reactively from a Ti target in Ar/O_2 (80/20) atmosphere, at 120 W sputter power and 0.1 Pa pressure, yielding a sputter rate of 0.014 nm/s. Ag was sputtered at 40 W in pure Ar atmosphere and 0.1 Pa pressure with a rate of 0.5 nm/s. AZO was sputtered from a ZnO target with 2 wt. % Al_2O_3, in pure Ar atmosphere at 0.1 Pa and 60 W, resulting in a rate of 0.28 nm/s. ZnO was sputtered from a pure ZnO target in pure Ar atmosphere, at 0.1 Pa, at 40 W, yielding a rate of 0.152 nm/s.

All targets were 4-inch in diameter and their distance to the substrate 100 mm. Base pressure in the deposition chamber was $1.4\text{-}2.4 \times 10^{-5}$ Pa. All films were deposited without substrate heating. In this thesis, variation of material thickness is denoted with subscripts in nm e.g. AZO_{51} means the device with an AZO thickness of 51 nm.

3.1.3 Ultra-sonic spray coating

Spray coating is an industry compatible and up scalable (for R2R applications) method for applying solution processed thin films on transparent substrates.[80,116,117] Therefore, it was chosen in this thesis for depositing NWs.

A schematic of the ultra-sonic spraying nozzle is shown in Figure 3.1-3 (a). The spraying solution is pumped to the nozzle by a motorized syringe (not shown) at a given flow rate. On its path through the ultra-sonic nozzle, the spraying solution is deagglomerated by the vibrations in the nozzle body. On the surface of the nozzle, a film of spraying solution is formed. By the vibration of the nozzle, microscopic solution droplets are ejected from the surface of the solution film Figure 3.1-3 (b). These droplets are blown down to the substrate by the shaping air. Above the nozzle, a shield which channels the shaping air is mounted (Figure 3.1-3 (b)). The shaping air forms the spraying cone and determines the impact speed of the droplets which are ejected from the nozzle surface.

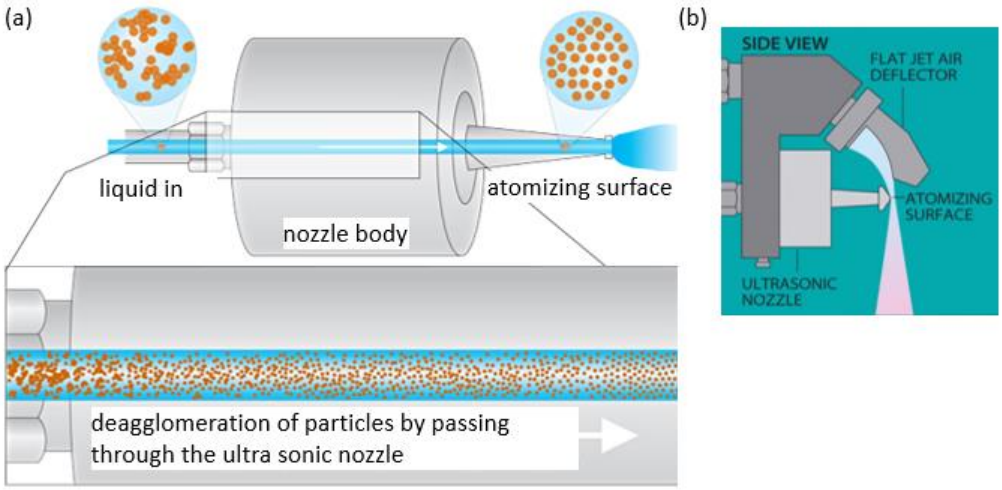

Figure 3.1-3: Schematic of spraying nozzle during spraying showing the liquid throughput. The magnification of the liquid throughput shows the deagglomeration of particles (nanowires) in the liquid stream because of ultra-sonic vibrations (a). Side view of the whole spray head, the liquid is atomized on the surface of the nozzle tip, atomized solution droplets are blown to the substrate by the jet air (b). Taken from [118] and modified.

Figure 3.1-4 shows the used Sonotek ExactaCoat spray coating unit. The whole system itself is visible in Figure 3.1-4 (a). The spraying unit itself is enclosed in a chamber with an attached exhaust. On the outside of the chamber a syringe pump is mounted, controlling the flow rate of the solution to the nozzle (not visible). Inside the chamber (Figure 3.1-4 (b)), a hotplate for substrate heating is mounted at the bottom. Above the hotplate level, the motor units for moving the spray head are fixed on rails. The spray head itself is equipped with a Sonotek ultrasonic nozzle, operating at a frequency of 120 kHz (Figure 3.1-4 (c)).

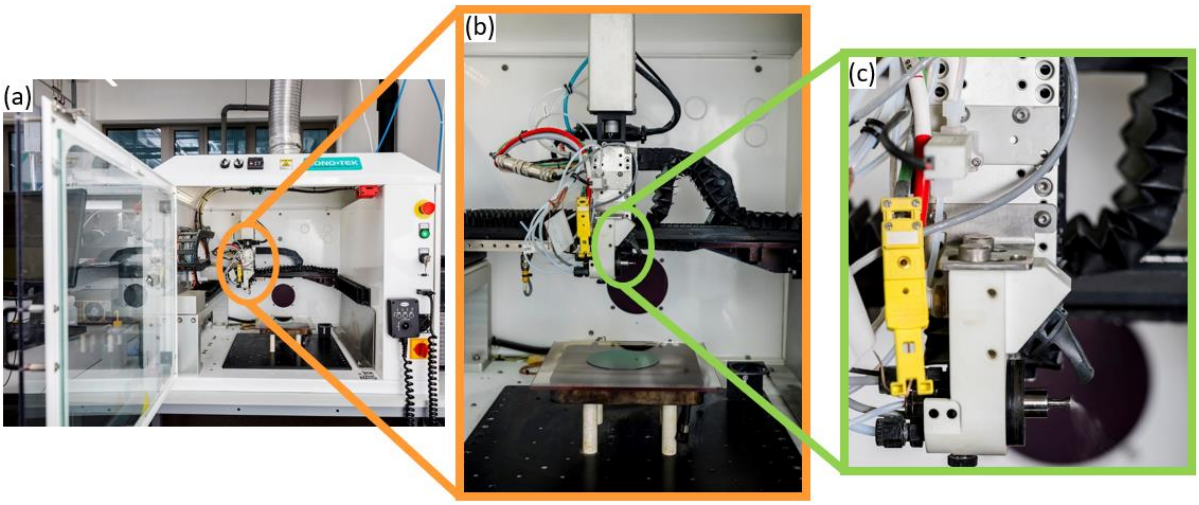

Figure 3.1-4: Spray coating unit used for this thesis, front view of the safety chamber with front door opened (a), inside the chamber is the whole spray head moving above the hot plate on rails (b), spray head ejecting liquid (c). © AIT, Sophie Menegaldo

Scardacci et al. published an article in 2011 about the optimum spraying parameters for Ag nanowires.[116] They showed that high back pressure (which refers to shaping air in this case) is beneficial for high figure of merit NW networks.

Because of the work from Scardacci et al., the shaping air was set to 9.95 bar, with 10 bar the highest possible setting of the machine. The nozzle to substrate distance was set to 200 mm. The flow rate of the suspension from the syringe to the nozzle was set to 0.4 ml/min and the power of the ultrasonic transducer was set to 1.7 W. The hotplate was set to 110°C for substrate heating. The number of scans of the nozzle above the substrate was 20.

For making the NW spraying solution, NWs were purchased from Sigma Aldrich (product code: 739421). According to the manufacturer's specifications, the mean wire length and diameter are 10 µm and 60 nm, respectively. NWs were delivered in an isopropyl alcohol (IPA) suspension with 0.5 % solid content. For the depositions presented here, this suspension was further diluted to a ratio of 1:5 with IPA, resulting to a 0.1 % NW solid content solution.

3.2 Characterization methods

This section explains the used techniques to investigate the properties of the manufactured thin films. Microscopic structural characterization as well as optical and macroscopic electrical characterizations were carried out to fully understand the influence of different layer morphologies on electrical and optical performance of the developed TE.

3.2.1 Structural characterization

To better understand optical and electrical behavior of the deposited films, microscopic morphology analysis needs to be done. For example: non-closed and fibrous metal films have low conductivity due to an unreached percolation threshold and low transmittance due to plasmonic absorption of micro clusters.

X-ray photoelectron spectroscopy (XPS)

XPS is a useful tool to non-destructively determine the chemical composition of solids at their surface. Additional to a chemical quantization of the atoms, the local bonding environment of an atomic species can be determined to understand the surface chemistry. The surface chemistry strongly influences sticking and diffusion parameters of adatoms during sputtering. This information is important to understand and influence film growth.[113]

XPS is based on the photoelectric effect which describes the ejection of electrons from a solid under the irradiation of photons. In XPS measurement systems, X-rays are used as a photon source to reach the electronic core structure of the atoms and their chemical bonds in the solid.[119]

The measuring process itself goes as follows: X-ray photons of known energy hit the material surface and eject an electron. The electron is accelerated with an applied electric field and its kinetic energy analyzed. According to Eq. 22, the binding energy of the electron can then be calculated with the work function ϕ depending on the spectrometer and the material, which is an adjustable instrumental correction factor. XPS data show graphs with the number of electron counts on the Y-axis versus the binding energy on the X-axis.[120]

$$E_{binding} = E_{photon} - (E_{kinetic} + \phi) \qquad \text{Eq. 22}$$

$E_{binding}$…binding energy; E_{photon}…photon energy; $E_{kinetic}$…kinetic energy of emitted electron; ϕ…work function

XPS was performed in a JEOL JPS-9030 photoelectron spectrometer system using the Al K_a (1486 eV) excitation source (monochromator was employed). The samples were grounded during the photoemission measurements.

X-ray diffraction

X-rays can not only be used to quantify the electronic structure of a solid by the photoelectric effect but also to determine the spatial arrangement of atoms in a solid (crystal structure). Knowing the crystal structure of a thin film is important in thin film production because the same material may have different properties depending on its crystal structure. Crystalline silicon for instance has higher charge carrier mobilities than amorphous silicon.

X-ray diffraction (XRD) is an important technique to determine the crystal structure of a material. It is done by shining X-rays of known wavelength on the sample. The collimated X-rays are diffracted by the crystal lattice of the sample. The diffraction pattern is recorded by an X-ray detector. According to Eq. 23 (Bragg's law), the distance between the atomic crystal layers of the material can be calculated. Hence, the atomic structure of the material can be estimated.

$$2d\,\sin(\theta) = n\lambda \qquad \text{Eq. 23}$$

d…distance between crystal layers; θ…incident angle; n…integer; λ…wavelength of X-rays

Figure 3.2-1 shows the used machine for this thesis. The sample is put on the sample stage. From there it is hit by X-rays coming from the X-ray tube outlet. The incident angle Θ is usually very small (2°-5°).

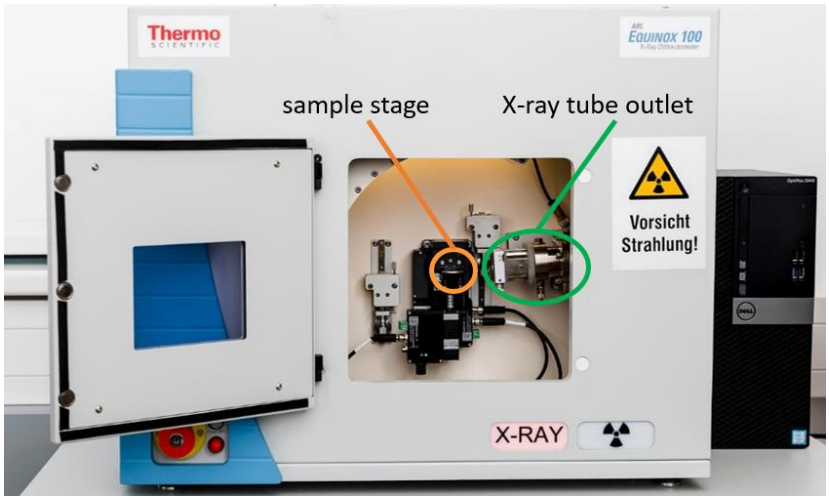

Figure 3.2-1: X-ray diffraction unit used in this thesis. © AIT, Sophie Menegaldo

The detector for the scattered X-rays is a semi-sphere enclosed in the housing (not visible). The detector resolves angle depended the counts of scattered X-rays. From the angle dependent X-ray count intensity, the crystal lattice is determined by assigning characteristic peaks to known values. The crystal structure of the films was investigated by a ThermoFisher Scientific ARL Equinox 100 X-ray diffractometer using a Cu K_a source (1.5419 Å).

Layer morphology (SFM, SEM, Confocal laser microscope)

To get a fast impression of a surface morphology in the nanometer scale, a scanning electron microscope (SEM) is the tool of choice. A SEM works by scanning an area with an electron beam and mapping the reflected electrons. The use of electrons as "light source" in this sort of microscope offers far higher resolutions of the sample surface compared to a microscope with visible light because the wavelength of electrons is far shorter than that of visible light. SEM images have magnifications of up to 1 000 000 times, while visible light microscopes have magnifications of up to 1000 times. Because of the use of an electron beam as light source, conductivity of the sample is important to inhibit unwanted electron deflection from charging.

For this thesis, a Zeiss SUPRA 40 as shown in Figure 3.2-2 (a), was used. The samples are mounted on the sample stage (Figure 3.2-2 (b)) and then brought into the vacuum chamber Figure 3.2-2 (c). The vacuum chamber is necessary to make the mean free path of the electrons long enough to go from the electron gun to the substrate and from the substrate to the detectors.

SEM-images were acquired with 5 kV acceleration voltage. For detection, a secondary electron and an in-lens detector were used. The in-lens detector detects electrons directly reflected from the sample surface and has a higher resolution than the secondary electron detector. The secondary electron detector detects electrons which are ejected out the of the sample by the primary electron beam leading to a better spatial resolution than the in-lens detector.

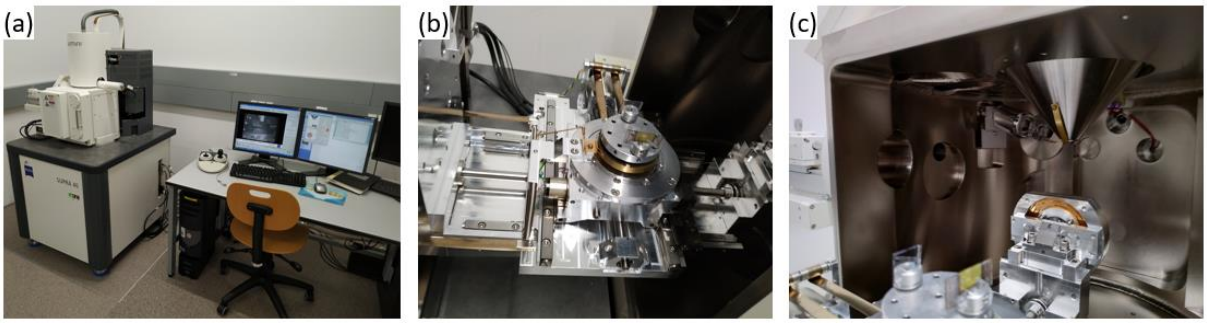

Figure 3.2-2: SEM used in this thesis (a); sample stage with samples mounted for cross-section images (b); inside view of the vacuum chamber (c).

In addition to SEM images, scanning force microscopy (SFM) measurements were done. A SFM works by moving an almost atomic sharp tip over a surface. For this thesis, two different modes for the tip movement were used: the tapping mode and the contact mode. In the tapping mode, the tip is vibrated by a piezoelectric stimulus. A laser measures the deflection of the tip. The tip is than brought close enough to the sample that the van der Waals forces of the surface atoms of the sample dampens the deflection. The change in vibration is mapped and gives an image of the surface morphology.

In the case of SFM measurements, the sample does not need to be electrically conductive in comparison to SEM measurements where a conductive surface is needed for the measurement.

Furthermore, a SFM measurement yields important statistic surface parameters such as the root mean square (RMS) roughness. The formula for the one-dimensional RMS roughness is given in Eq. 24. It describes the square root of the mean of the squares of the measured height values. This means that the higher the RMS value, the higher are the height changes of a surface. The RMS roughness is an important quantity to qualify TEs, because a high RMS roughness of the TE can lead to shorts through a thin film device.

$$RMS = \sqrt[2]{\frac{1}{n}\sum_{i=1}^{n} y_i^2} \qquad \text{Eq. 24}$$

RMS…root mean square; *n*…number of measured height points; *y*…measured height

The whole set up is shown in Figure 3.2-3. The samples are mounted underneath the sample stage (Figure 3.2-3 (a)). The samples stage holds the laser above the sample. In Figure 3.2-3 (b), the sample stage is shown. It is housed in a noise cancelling housing to avoid tip vibrations caused by sound. Additionally, one can see the microscope above the sample stage which is used to align the laser focus the measuring tip and the sample. Figure 3.2-3 (c) shows the whole system with computers to monitor the measurement.

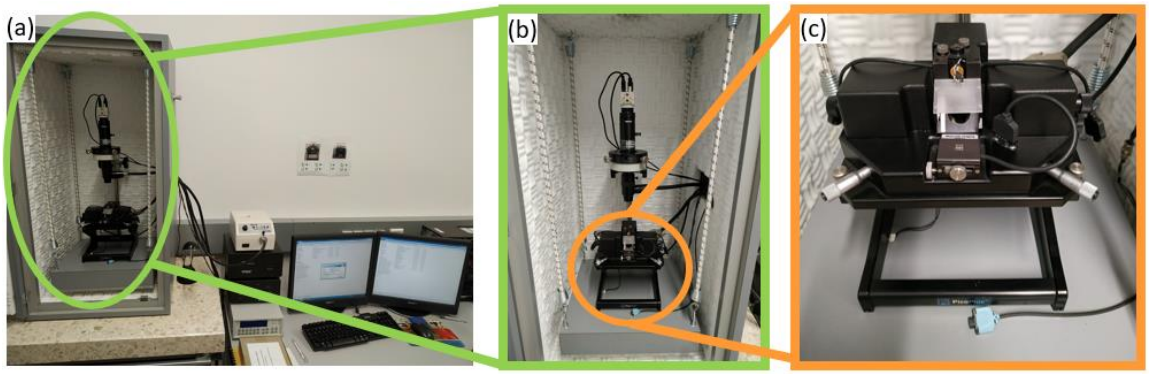

Figure 3.2-3: SFM used in this thesis whole set up with analysis PCs and control units (a); sound proof box in which sample mounting is kept with microscope for tip positioning (b); sample mounting with laser and sensor (c).

In this thesis, a Molecular Imaging Pico Plus SFM was used in tapping mode, with SSS-NCHR tips from Nanosensors™.

Scanning an area with a SFM is time consuming due to the necessity of mechanical movement of the tip over the surface. The scan speed must be adjusted that vibrating tip can change its height fast enough without touching the surface.

A faster method to achieve larger surface topographic images is confocal laser scanning microscopy (CLSM). The higher speed during measurements comes for the cost of losses in resolution. In CLSM a laser scans pointwise the surface of the sample. To achieve a 3-dimensional image of the surface,

multiple images with different focuses were taken at the same point and depicted by a computer software. Laser confocal microcopy images were taken with an Olympus LEXT 3D OLS4100.
SFM and CLSM measurements were analyzed with the open software Gwyddion.

Profilometry

A profilometer measures the surface topography of a material but with a far lower lateral resolution than the SFM. Main parts are a cantilever with a needle, an electrical coil for vertical measurements and a moveable sample stage. The measurement is done by a needle which is scratching over the surface while the sample stage is moved underneath. The vertical displacements of the needle are measured inductively with an electrical coil attached to the cantilever. The lateral position and the vertical amplitude are mapped. In this research, the profilometer was only used to measure line profiles to determine film thicknesses. Figure 3.2-4 shows the used Profilometer set up. The profilometer is located on a shock absorbing table. To reduce measurement noise, the transparent part covers the substrate holder (black plate). The PC controls the measurements and offers analysis software for step height analysis.

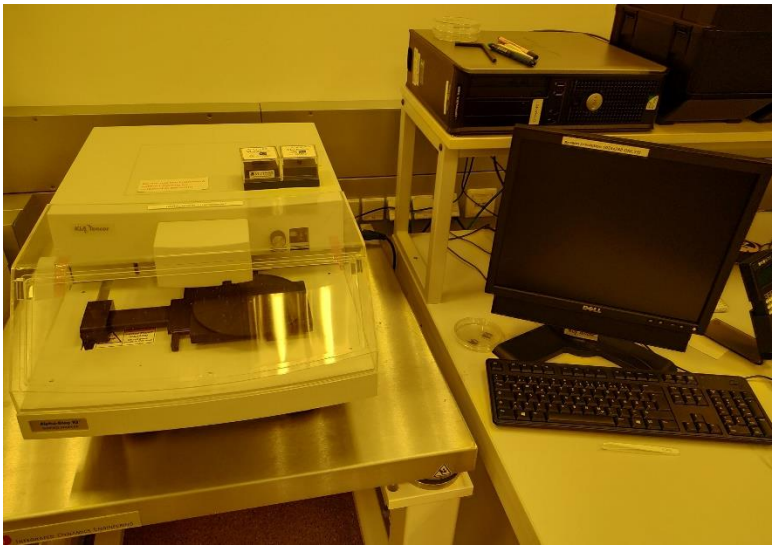

Figure 3.2-4: Profilometer on metallic table (air suspended to avoid vibrations) with black sample stage behind Perspex for noise cancelling; to the right control PC.

Mechanical bending tests

To test the conductivity changes of the TE as a function of multiple bending cycles, bending tests were performed. Figure 3.2-5 shows a scheme of the sample geometry and setup. Bending tests were performed with a MARK 10 ESM 3 tension/compression force setup at a speed of 1 m/min. The bending radius was 4 mm for compressive and 4 mm for tensile stress. The electrical resistance of the samples during the bending tests was measured from one edge to the opposite edge of the sample along the strain direction. Ag paste combined with Cu adhesive tape was used as contacts. The resistance was measured at the relaxed state after a certain number of bending circles.

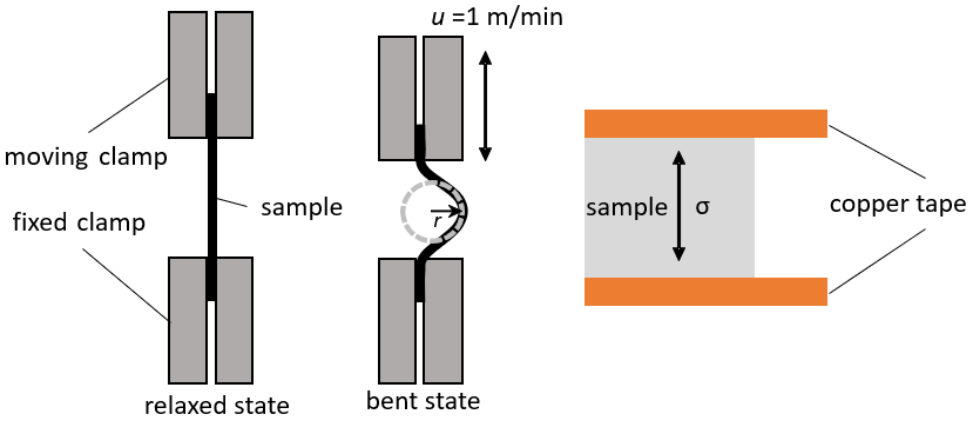

Figure 3.2-5: Sample geometry and experimental setup used for the bending tests. Taken from [121] and modified.

3.2.2 Optical characterization

To characterize the optical properties of the transparent electrodes, transmittance and reflectance were measured. To measure the transmittance of a sample, the light intensity without the sample is measured first and then the light intensity through the sample. As described in section 2.1.3 (Eq. 19), the ratio of these two intensity values gives the transmittance. Transmittance and reflectance are wavelength dependent properties; therefore the wavelength of the light must be tuned during the measurement to measure the part of interest of the electromagnetic spectrum. As a result, most spectrometers use a broad band light source which emits all wavelengths. Wavelength tuning is than either done by a prism or a grating.

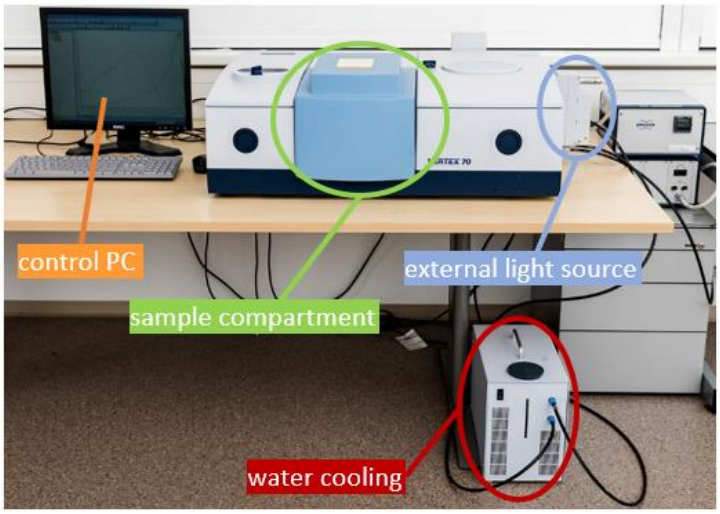

Figure 3.2-6: Spectrometer unit with control PC used in this thesis. © AIT, Sophie Menegaldo

Figure 3.2-6 shows the whole spectrometer set up used in this thesis. It is a Bruker Vertex 70 Fourier transform (FT) equipped with an additional visible light source. Figure 3.2-7 shows the different mountings for the different measurements.

Specular transmission is measured with the light going through the sample with an incident angle of 90° between light and sample surface (Figure 3.2-7 (a)). For samples with a high haze, the specular transmittance would yield too low values, thus an integration sphere can be used to measure the total transmittance of a sample.

Figure 3.2-7 (b) shows the used integration sphere tool. The light passes the sample at 90° like in the specular measurement. Instead of putting the detector in a straight line behind the sample, the light enters the integration sphere. It is a Teflon sphere which scatters the light evenly distributed into the whole sphere. With this method, any light which is transmitted but maybe deflected by the sample can be measured.

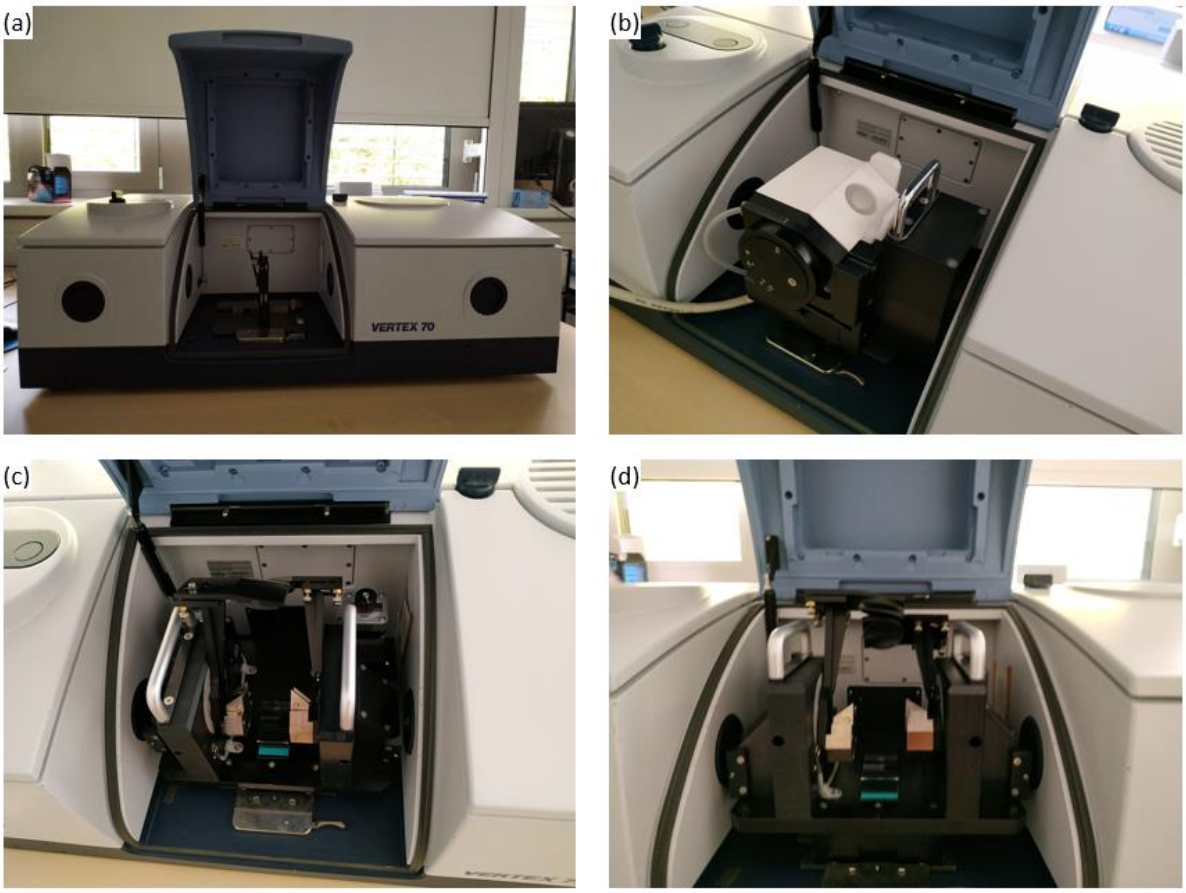

Figure 3.2-7: Different measurement units for the spectrometer: specular (a); integration sphere (b); reflectance (c)-(d).

Figure 3.2-7 (c-d) show the reflectance unit of the used spectrometer. Light enters from the right as in all the other measurements. The mirrors reflect the light to the center where the substrate holder is located. The light which is reflected from the substrate is collected by the other mirror and passed on to the detectors. After measuring the incident light over the mirror, the mirror is replaced by the sample of interest. The relation of both measurements gives the reflectance as shown in Eq. 20.
For the wavelength range of 330-550 nm, a GaP-detector was used and for the range of 550-1150 nm a Si detector. Transmittance measurements are referenced to air while for reflectance measurements, a STAN-SSH-NIST mirror from Ocean Optics was used as reference. Transmittance measurements were acquired at 0° incidence angle, reflectance measurements were performed at 13° incidence angle. To measure the total transmittance (specular- plus scattered transmittance), an integration sphere coated with Teflon provided by Bruker was used.

3.2.3 Electrical characterization

The scope of the thesis is the development of a transparent electrode. To quantify the electrical conductivity of the developed electrode types, different resistance measurements, which will be explained in the following sections, were performed.

Sheet resistance

To measure the sheet resistance as explained in section 2.1.1, 4-point measurements were performed. In a 4-point measurement set up, 4 probes are applied in line on the material as the name implies. Between the outer two probes, a current is applied while between the inner two probes, the voltage drop is measured. R_{sh} is calculated according to Eq. 25. This set up leads to higher accuracy of the measurement especially for low resistances as different probes are used for current and voltage.

$$R_{sh} = \frac{\pi}{\ln(2)} \frac{U}{\mathrm{I}} \qquad \text{Eq. 25}$$

R_{sh}...sheet resistance

Sheet resistance of the samples was measured with a 4-point in-line probe (Nagy SD – 600). Figure 3.2-8 shows the used equipment. In Figure 3.2-8 (a), the whole system with the wired probe tip is visible while in Figure 3.2-8 (b), a magnification of the 4-point probe is visible. These 4 tips are pressed on the thin film and the sheet resistance is measured.

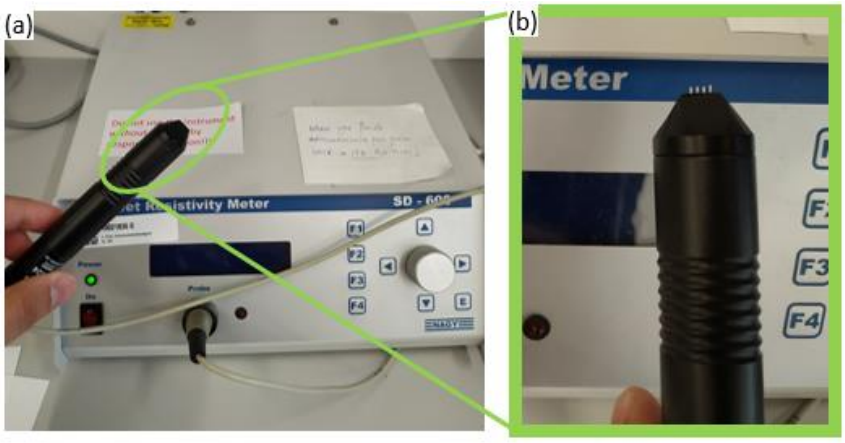

Figure 3.2-8: 4-Point measurement system to obtain sheet resistance values of thin films (a). Magnification of the 4-point tip (b).

Local conductivity measurements (Conducting SFM)

The SFM was not only used in tapping mode but also in the so-called contact mode. As the name implies, the tip is in mechanical contact with the substrate surface. In this case the contact mode was performed in the so called constant force mode, which means that the force on the cantilever is kept constant and adapted according to morphological changes. These adaptions are mapped over the surface and give a morphological image.

In the case of c-SFM measurements, contact mode measurements were performed with a conductive tip and a closed electric circuit. For these measurements, a bias was applied to the SFM tip while the sample was grounded. The maximum current that can be recorded is 10 nA. Therefore, it was possible to measure the microscopic morphology simultaneous to the microscopic surface conductivity. This was important for the embedded nanowires to map the surface conductivity distribution. Tips from Nanoworld (CONT Tips), which were sputter-coated in house with 5 nm Ti, followed by 20 nm Au were used for this purpose.

3.3 OLED fabrication

The finalized electrodes needed to be implemented in a device to proof their concept and study possible design flaws. OLEDs are widely applied in consumers electronics and more susceptible to inhomogeneous charge carrier injection than photovoltaic cells. This is the reason why OLEDs were chosen as a testing device.

The first step of OLED manufacturing on designated TE electrodes was to structure the TE on the substrate. The structuring of the electrode needed to be done to match the electrical contact scheme of the measurement set up. Figure 3.3-1 shows the process of structuring TEs for OLED fabrication. First, the 15 x 20 mm^2 PET or glass substrates were sputter coated. To achieve a defined 5 mm wide strip in the middle of the substrate, a 5 mm wide Kapton® tape strip was applied (Step II). After covering the middle strip, the remaining area was cleaned with a cotton swab dipped in 2 % HCl solution (Step III). To avoid unwanted removal of TE material on the strip area, the substrates were rinsed with ultra-pure water before removing the Kapton® strip.

In the case of NW electrodes, the sides of the substrates were covered with two Kapton® strips to achieve a 5 mm wide NW strip in the middle of the substrate.

To match the electrode structure of the measuring set up, Cr/Au electrodes were evaporated at the sides of the strip (Step V). This was done for the sputtered and the sprayed electrode samples. On this structure the OLED layers were spin coated. The counter electrodes of the OLED (MoO_3/Ag) were evaporated through a shadow mask. This connects the Au fingers with the middle strip of the TE material. The overlap of TE and counter electrode is the 2 x 2 mm^2 active OLED area.

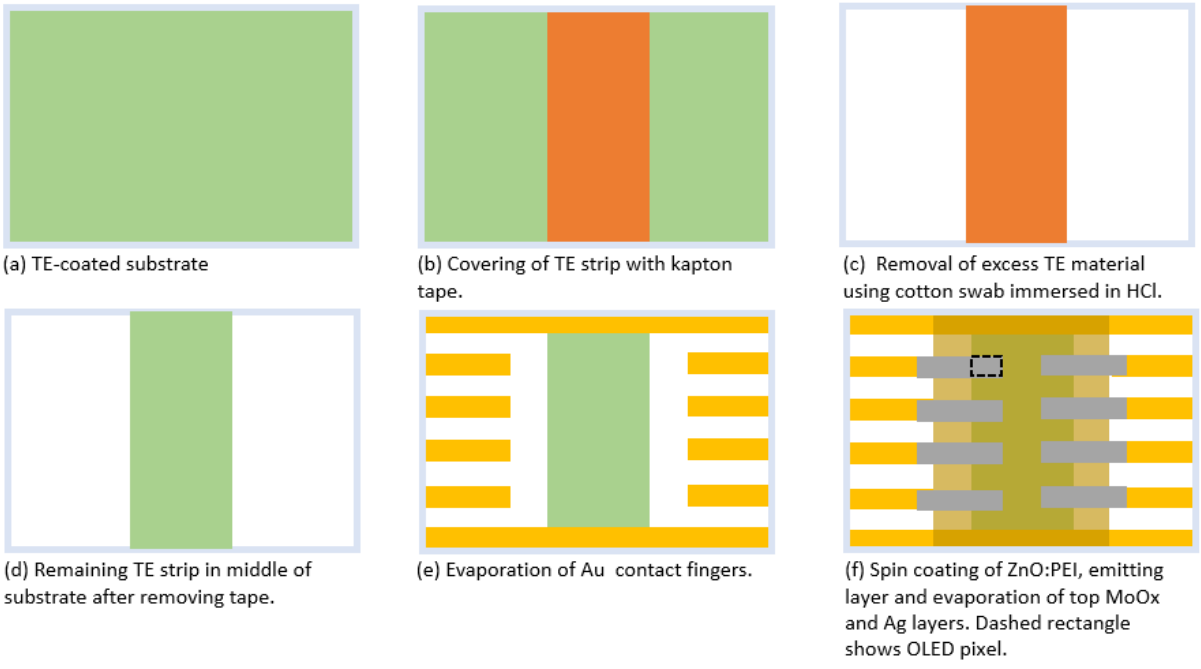

Figure 3.3-1: Process of structuring TEs for OLED manufacturing. Drawing submitted at *Adv. Eng. Mat.* and modified.

3.3.1 Plasma treatment

Plasmas consist of ions in gaseous phase and free electrons; an example is shown in section 3.1.2 for the case of a sputter plasma. In the case of sputtering, the charged particles bombard the target surface with high enough energy to extract target particles.

In general, the energy of the particles in the plasma can be lowered to avoid material abrasion. In this case, plasmas can be used to remove adatoms from a surface. In addition to the physical bombardment, chemical reactions can be created if a plasma contains reactive atoms. For example: in the case of reactive sputtering, the ionized gas atoms react with target atoms. Regarding this thesis, oxygen was added to the sputter gas to create metal oxides. Using these reactions, a plasma can manipulate a surface in many ways, such as removal of adatoms, activation of chemical surface groups or roughening. All these influences modify the surface energy and hence the wettability of a surface. Furthermore, the work function of the material is influenced by surface dipoles created by the plasma.[122] As explained in section 3.1.1, wettability and surface energy are important factors in thin film deposition to achieve homogenous, closed and smooth layers.

Plasma cleaning is widely applied in the semiconductor industry. For instance: O_2 plasma treatment leads to the formation of OH groups on the surface of the treated sample; this increases the surface wetting.

In this research, the plasma oven (FEMTO DIENER PLASMA) was used to accomplish two tasks. On the one hand the described surface modification of TEs for OLED production and on the other hand the welding of the nanowire thin films.

As described in section 2.2.2, NWs have an organic capping around them which needs to be removed. It was decided to use the plasma oven to fulfill this task for the following reason: Plasma treatment for nanowire welding is faster than conventional ovens or hotplates, because the wires are inductively heated by the oscillating electric field in the plasma oven. As will be shown in detail in section 5.1, inductive heating of the nanowires is beneficial over conventional hot plates since it offers the possibility to weld the NWs if they are embedded in an insulating material on a heat sensitive substrate.

The process for welding NWs in the plasma oven goes as follows: the NW-coated substrates are brought in the chamber through the door (Figure 3.3-2, plasma chamber with window). After the samples were put in the plasma chamber, the chamber was evacuated, until the pressure in the chamber reached 0.3 mbar. The residual gas in the reactor chamber was ambient air. For sintering, NWs no process gas was turned on. The generator was set to 100 W with a stimulating plasma frequency of 2.45 GHz. An integrated timer stopped the process after the time set. After that, the chamber was vented and the samples were taken out. NW samples for OLED manufacturing were spin coated with ZnONP:PEI directly after this step to use the enhanced surface wetting from the plasma treatment.

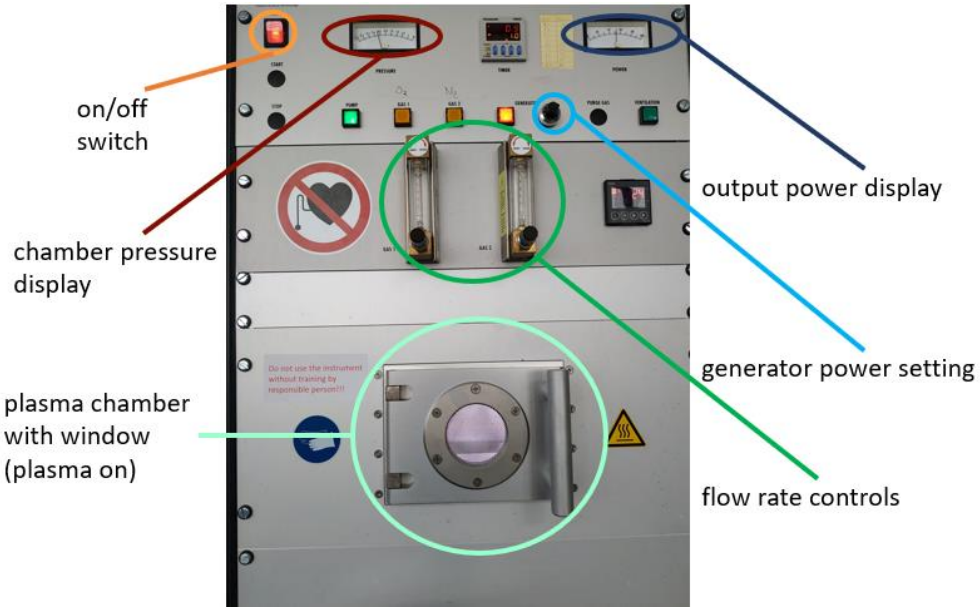

Figure 3.3-2: Image of the used Plasma tool for this thesis.

Glass and PET substrates were O_2 plasma etched before spin coating with Ormoprime®. To do so, the samples were brought in the chamber. At that point, the chamber was evacuated to 0.3 mbar. To use O_2 plasma, the process gas O_2 was turned on and controlled via the flow rate controls (Figure 3.3-2). The generator was set to 80 W and the timer to 5 minutes. All DMD and ITO substrates were Ar plasma etched before spin coating them with ZnONP:PEI. Samples were plasma treated at 500 W with 0.35 mbar Ar for 5 minutes.

3.3.2 Spin coating

A widely used technique to achieve solution processed thin films besides spray coating is spin coating. Spin coating is a fast method to achieve solution processed thin films. For spin coating, a substrate is coated with a solution of the desired material. After that, the substrate is rotated to spin of excess material which is pulled of the substrate radially. The faster the spin speed the thinner the solution processed thin film gets. Moreover, film thickness is influenced by the concentration of the dissolved material in the solution and the wetting behavior of the substrate surface, as discussed earlier. The higher the material concentration in the solution the thicker the film and the better the wetting the thicker the film.

Figure 3.3-3 shows the used spin coater. The sample is placed on the chuck (blue circle) with a rubber O-ring placed underneath. Under the O-ring, a vacuum is applied which keeps the substrate in place during spinning.

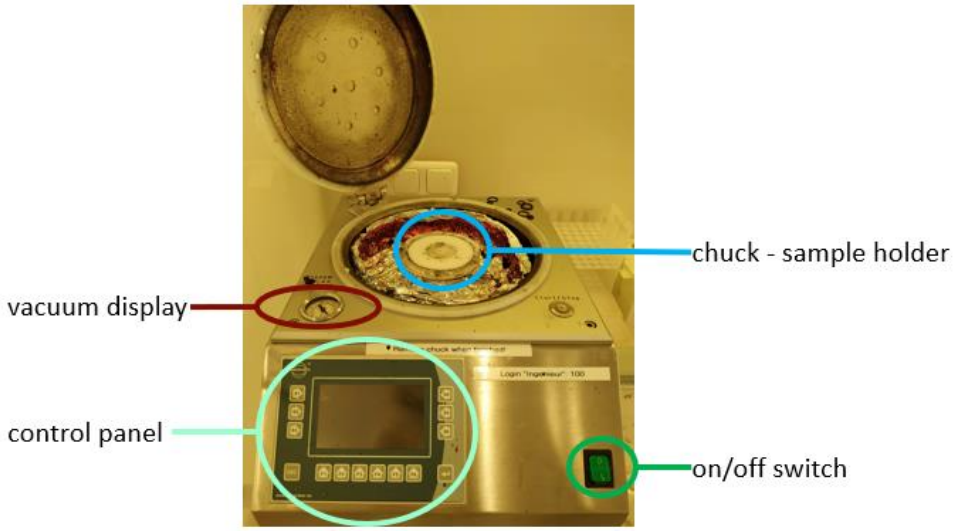

Figure 3.3-3: Spin coater used for this thesis.

With the control panel (turquoise circle), the desired rounds per minute and spinning time can be set. Before starting the process, the vacuum needs to be checked (red circle) to ensure a safe substrate positioning during spinning.

Spin coating was used in this thesis for applying thin films of Amonil®, PMMA, Ormoprime® and for OLED manufacturing. Amonil® (from AMO GmbH, Germany) MMS10 was spin coated with 6000, 3000 and 1000 rpm to obtain film thickness of 80, 100 and 250 nm, respectively. For 550 and 800 nm thickness, Amonil® MMS1 was spin-coated at 6000 rpm and 3000 rpm, respectively. All Amonil® samples were spin coated for 120 seconds.

The reference material PMMA (Sigma Aldrich, with average molecular weight 350,000) was spun from a 2 wt. % solution in acetone at 1000 rpm for 120 seconds.

PET and glass substrates for embedding NWs were spin coated with Ormoprime at 4000 rpm for 60 seconds.

For OLED production, samples were first spin coated with a ZnONP:PEI (2:1) in IPA solution with 2500 rpm for 60 seconds and heated for 10 minutes at 110 °C. The PEI solution was prepared according to the recipe of Zhu et al.[110], with PEI purchased from Sigma Aldrich. The ZnO nanoparticle solution was purchased from Genesink. Following the spin coating step, the samples were put on a hot plate at 110 °C for 10 minutes. On the ZnONP:PEI layer, the emitting layer PDY-132 (Super Yellow, Merck) was spun at 2500 rpm for 60 seconds from a 5 mg/mL toluene solution, no heating was applied after the spin coating step.

3.3.3 Physical vapor deposition

Evaporation offers a less technologically complex way of vacuum based thin film deposition than sputtering. In a vacuum chamber, materials are heated until they evaporate. After that, the vapor covers the desired substrate. The vacuum is necessary to assure that the mean free path of the evaporated particles is long enough to reach the substrate.

In general, evaporation is possible for organic and inorganic materials. However, in this study only inorganic metals were evaporated. Figure 3.3-4 shows the used evaporation chamber for this thesis. On the bottom, the tungsten boat which contains the desired process material is visible (green circle). Atop the boat, a source shutter is mounted to avoid contamination of the chamber during pre-heating.

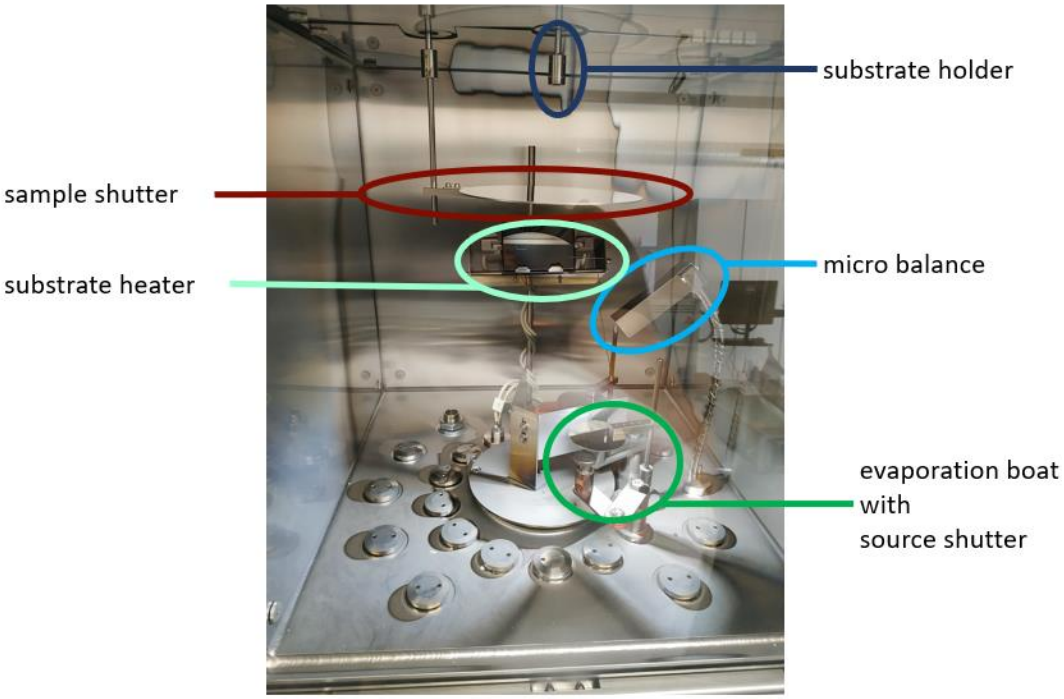

Figure 3.3-4: Physical vapor deposition chamber used for this thesis.

Above the source, a microbalance is mounted (light blue circle). The microbalance controls the evaporation rate and the film thickness via an oscillating crystal. The substrates are mounted to the substrate holder on the top of the chamber (dark blue circle). To deposit materials with a desired rate (atoms arriving on the substrate per unit time), the evaporation boat is pre-heated until the desired rate is achieved. When the desired rate is achieved, the sample shutter (red circle) is opened and the atoms can reach the substrate. To influence film growth, a substrate heater which was not used in this work, is mounted underneath the sample shutter (turquoise circle).

The evaporator was used for the last step of OLED production. After spin coating the ZnONP:PEI and Super Yellow layer, 10 nm of MoO_3 and 200 nm of Ag were evaporated to finish the OLED. Furthermore,

the evaporator was used to evaporate 10 nm of Cr and 50 nm of Au as contacts on the in-house manufactured TEs for OLED production.

3.3.4 OLED characterization

The implementation of the developed electrode in a functional device like an OLED is the final proof of concept. To characterize the quality of an OLED, current density-voltage-luminance (JVL) characteristics were measured as described in section 2.3.1. With the JVL characteristics it is possible to calculate the power and current efficacies of the device, which are besides the maximum luminance the key features of an OLED.

JVL characteristics were measured using a Keithley 2450 source measurement unit together with a Konica Minolta LS-160 luminance meter in a custom setup. The EL spectra were measured with an Ocean Optics CS2000 spectrometer and recorded with Ocean View software.

4 Transparent dielectric/metal/dielectric electrodes

The scope of the thesis is the development of flexible transparent electrodes (FTE). As explained in section 2.2.1., DMD electrodes are a promising candidate to realize a FTE since they reach R_{sh} < 10 Ω/sq on glass and on PET. Furthermore, no substrate heating is necessary. In DMD structures, the refractive indices and thicknesses of the dielectrics below and atop the metal layer can be optimized to maximize the transmittance of the whole electrode as shown in section 2.1.4.

The most common DMD electrode is ITO/Ag/ITO. This electrode is already commercially available with a reported maximum transmittance of 83.5 % (at 6.7 Ω/sq) on glass[123] and 82.4 % (at 9 Ω/sq) on PET.[63] The aim and scope of this thesis consists of finding an ITO free alternative with higher performance values if possible.

The theory behind dielectric metal dielectric electrodes was explained in section 2.1. In the end of the section, the transfer matrix algorithm to calculate the dielectric layer thicknesses to maximize transmittance was described. With the theoretical background and the help of the algorithm, different DMD combinations could be calculated first and afterwards, the most promising ones were sputtered. In all cases, silver was used as metal while differently doped metal oxides with adjusted layer thicknesses were used as dielectrics. At first, the different DMD combinations were tested on glass.

Glass is widely used as transparent substrate as it offers a flat surface, chemical and temperature stability as well as excellent optical properties. However, it is not suitable for flexible and light weight applications. As an alternative, PET is widely studied. It is cheap, light weight and offers also good optical properties.[124] A drawback of PET is its higher surface roughness compared to glass which can influence sputter deposition as will be shown in this chapter.

Different ways of PET planarization to overcome roughness issues are presented and investigated in the chapter at hand. In the end, the most promising candidate of DMD electrode is tested in an OLED. It will be shown that the developed electrode outperforms the commercial industry standard electrode ITO in terms of luminance, efficacy and mechanical flexibility while simultaneously offering an indium free, non-toxic and cheap material composition.

4.1 DMD electrode types, properties and morphologies

One of mankind's oldest used materials is glass. Vulcanic glass was used long before humans found out to produce glass on their own.[125] Glass making dates back to 3600 BCE as discoveries of archeologists in Egypt and Mesopotamia suggests.[126,127] Nowadays, glass is an everyday component of modern living. The word glass describes a solid which is formed by rapid melt cooling.[128] By doing so, the atoms in the melt do not get the chance to form a crystalline solid but an amorphous. Hence, the atoms in the glass show no long-range periodicity but a high degree of short range order.[129]

The used glasses in this thesis were soda lime float glasses. Soda lime glass contains about 70 to 74% silica by weight and the rest is made up by Na_2CO_3 (soda) and CaO (lime). Other additives in the melt include MgO and Al_2O_3.[130] The term float glass describes the making of the glass. This process was developed in the 1950s by the British glass manufacturer Pilkington, who pioneered the technique. During the process, the glass melt is poured on a tin bath on which the melt forms a floating ribbon. Due to the surface tension of the liquid glass melt and the tin bath, a smooth surface forms on both sides of the glass.[131] Figure 4.1-1 (a) shows an SFM image of a glass substrate used in this thesis. The glass surface features a RMS roughness of 1.5 nm.

In contrast to one of mankind's oldest used materials, one of mankind's younger materials was used in this thesis as flexible transparent substrate. PET was patented in 1941 by Whinfield et al.[132] Since then, PET became a material used in a lot of every day live products such as clothing and food packaging.

One special form of PET is biaxially-oriented PET (BoPET). During the production of BoPET, PET is melted and then extruded onto a chill roll. This step is similar to the process of glass production in terms of achieving a rapid cooling to freeze the liquid into the solid state. In contrast to glass production, the BoPET is then drawn by heated rollers first in machine direction, followed by orthogonally drawing in a heated oven. These steps are the biaxially orienting steps. In contrast to amorphous glass, BoPET is recrystallized after drawing in an oven under tension. The crystallites in BoPET form so rapid, that they reach the boundaries of neighboring crystallites fast enough so that the crystallite size is smaller than the wavelength of visible light, resulting in excellent transmittance despite BoPET being semi crystalline.

By producing BoPET in the described way, it would form a perfectly smooth surface like glass. If BoPET would be rolled up with such smooth surfaces, individual layers would strongly adhere to each other. To avoid this, BoPET foils are artificially roughened by adding silica gel or TiO_2.[133,134] The PET foil used in this thesis features a RMS roughness of 15 nm (Figure 4.1-1 (b)).

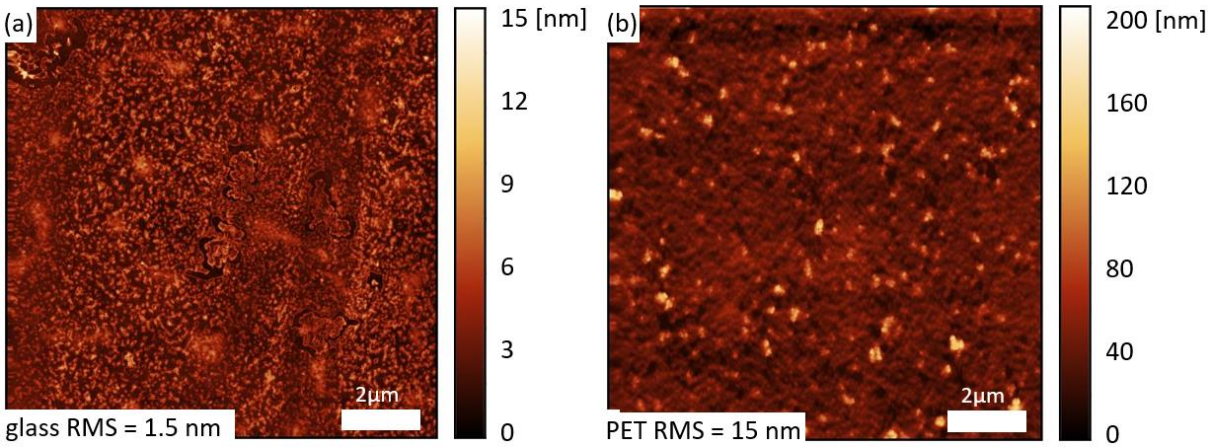

Figure 4.1-1: SFM images of the used substrate materials in this thesis, showing that glass (a) has a much smoother surface than PET (b).

After explaining surface morphology of glass and PET, optical properties are discussed in detail to understand the different optical behavior which may arise if the same sort of thin film is applied on either glass or PET. The refractive indices of glass and PET are shown in Figure 4.1-2 (a). Glass has a relatively constant refractive index of 1.5 in the visible spectral range while its extinction coefficient is zero over the same spectral range. In the same wavelength range, PET has an average refractive index of 1.64 but also an extinction coefficient equaling zero. This leads to the transmittance spectra shown in Figure 4.1-2 (b). Due to the lower refractive index of glass compared to PET, it has a higher transmittance and a lower reflectance than PET. Both substrates show zero absorbance due to the same extinction coefficient, which is equaling zero.

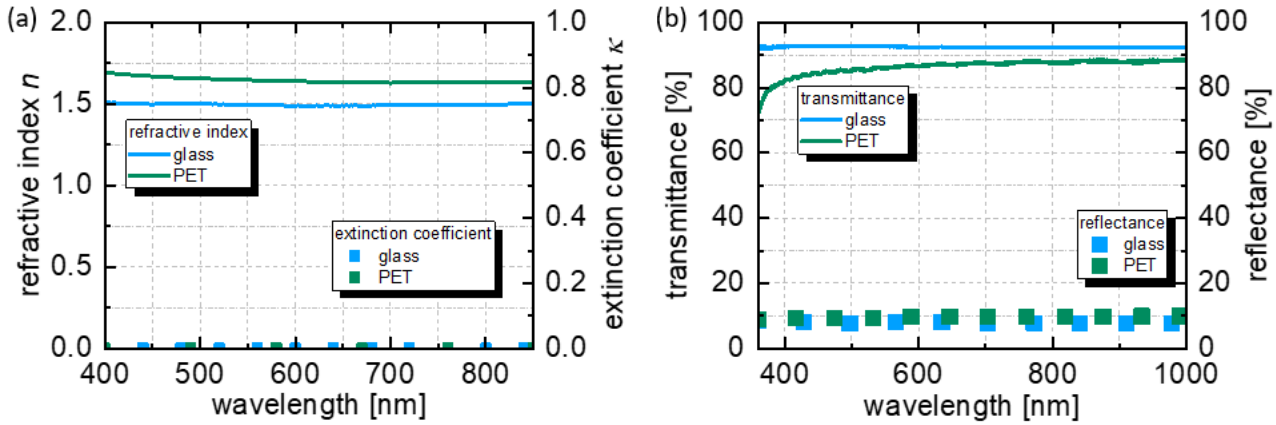

Figure 4.1-2: Refractive index and extinction coefficient of glass and PET (a). Transmittance of used glass and PET substrates (b).

4.1.1 DMD electrodes using the same top and bottom dielectric

Zinc oxide is a widely studied material for its application in TCOs. It features many positive aspects. Especially its direct wide band gap (E_g ~ 3.3 eV) makes it suitable for optoelectronic applications.[135] Furthermore, it is nontoxic, abundant and cheap, key features for a sustainable and low cost transparent electrode.[136]

Unlike ITO, ZnO is chemically and thermally stable under hydrogen plasma processes that are commonly used for the production of solar cells.[136] ZnO films offer a work function of 3.74 eV[137] in comparison to ITO which has a work function of 4.26 up to 5.24 eV depending on post deposition treatments.[138] Therefore, ZnO based devices are more suitable for inverted device architectures.

First studies of ZnO/Ag/ZnO layers on glass were done in 1985.[139] It took until 2008 when Han et al. published the first ZnO/Ag/ZnO electrode study on PET.[136] In this study, the Ag layer thickness was varied and a constant ZnO layer thickness of 35 nm for top and bottom dielectric was used.

To further optimize Han's approach, ZnO/Ag/ZnO multilayers were fist simulated for the optimal ZnO layer thicknesses. The refractive indices and extinction coefficients used for the simulation are shown in Figure 4.1-3. All materials - except for silver - show an extinction coefficient equal to zero. The extinction coefficient of silver rises constantly from lower to higher wavelength ranges in the visible spectrum. For Ag, the complex refractive index was extracted from the literature while all other refractive indices were measured in house.[140]

The simulation shown in Figure 4.1-3 (b-c) yielded optimum thicknesses of 42 nm ZnO in contact with the substrate and 40 nm ZnO on the top, for glass and PET substrates. Maximum average (400 -700 nm) simulated transmittance values for the layers on glass is 88 %, the same layers on PET only yield 86 %. The simulated 2 % lower maximum transmittance value for the PET substrate derives from the higher reflectance at the air/PET interface in the simulation. It is noteworthy that for both substrates, the thickness deviation of the bottom ZnO layer is less critical than the thickness deviation of the top ZnO layer.

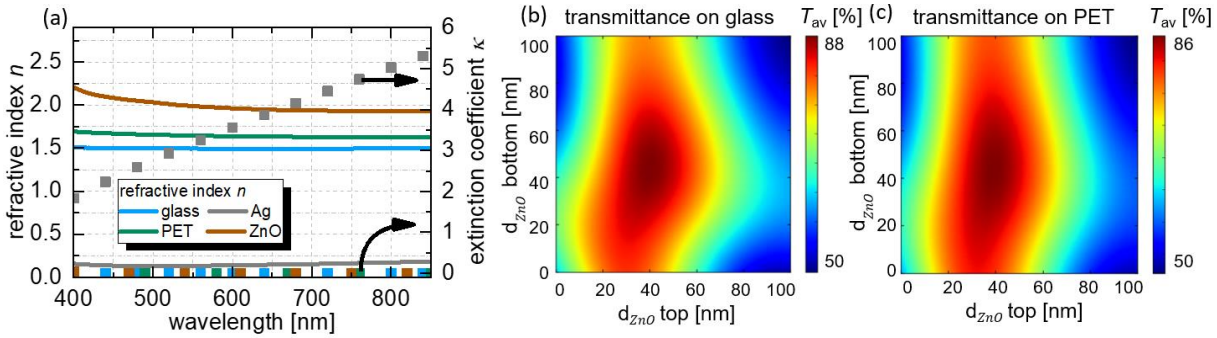

Figure 4.1-3: Refractive indices and extinction coefficients of glass, PET, Ag and ZnO (a) used for the simulations to yield the heat map of transmittance on glass (b) and PET (c).

With the simulated ZnO thickness values, first sputter experiments were started on glass and on PET to investigate the film morphology, depending on the used substrate. Figure 4.1-4 show SEM images of the ZnO/Ag/ZnO layers on glass (a) and PET (b). On glass (a), a much smoother film is achieved compared to PET (b). Nevertheless, it is also visible that the approximate grain size is in the same range. Therefore, the roughness must result from the initial PET roughness of 15 nm, as shown in Figure 4.1-1.

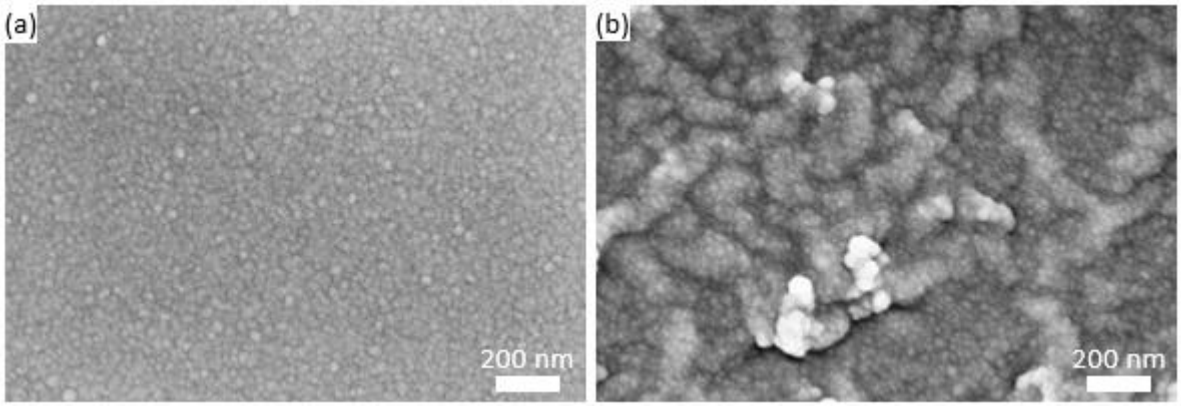

Figure 4.1-4: SEM images of ZnO/Ag/ZnO electrode on glass (a) showing a smooth closed layer without pinholes and PET (b), also showing a closed layer but a high background roughness caused by the PET substrate roughness.

SFM measurements (Figure 4.1-5) confirm the SEM observations. On glass, the layer system features a roughness of 1.1 nm (Figure 4.1-5 (a)) while on PET, a RMS roughness of 4.7 nm is extracted (Figure 4.1-5 (b)). This difference in roughness mainly derives from the initial substrate roughness as shown in Figure 4.1-1. The sheet resistance is 7 Ω/sq for the electrode on glass and 6 Ω/sq for the electrode on PET. An almost similar R_{sh} for both substrates results from the constant silver layer thickness and the closed film morphology.

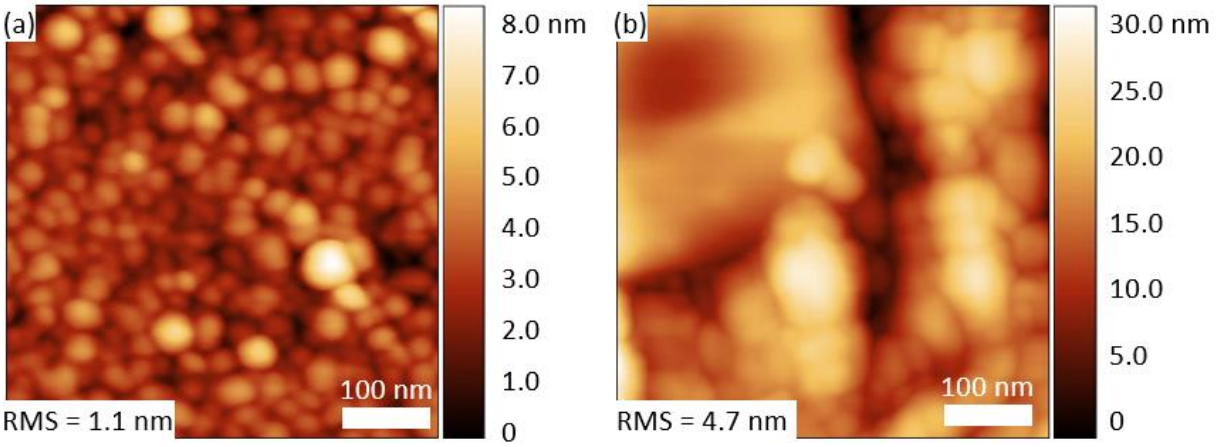

Figure 4.1-5: SFM images of ZnO/Ag/ZnO electrode on glass (a) and PET (b) confirming the SEM images and quantifying the roughness observations.

Transmittance spectra of ZnO/Ag/ZnO are shown in Figure 4.1-6. The deposition of the ZnO/Ag/ZnO on the substrates on glass (orange) and on PET (blue) lowers the transmittance drastically in the range

below 400 nm (Figure 4.1-6 (a)), compared to the bare substrates. As the reflectance does not increase drastically in this area, this decrease is related to absorption.

Although the simulation predicted similar results, T_{av} on glass equals 86.0 % and on PET 75.1 %. The differences are caused by higher reflectance (Figure 4.1-6 (b) and higher absorbance of the PET based electrode. The higher absorbance is caused by the higher film roughness while the higher reflectance must relate to the PET/air and PET/ZnO interfaces.

The decrease of transmittance, starting on both substrates at approximately 700 nm, is related to the reflectance losses since the layer thicknesses were optimized for minimum reflectance only in the range from 400 to 700 nm. Still, these electrodes are more transparent compared to the electrodes published by Han et al..[136]

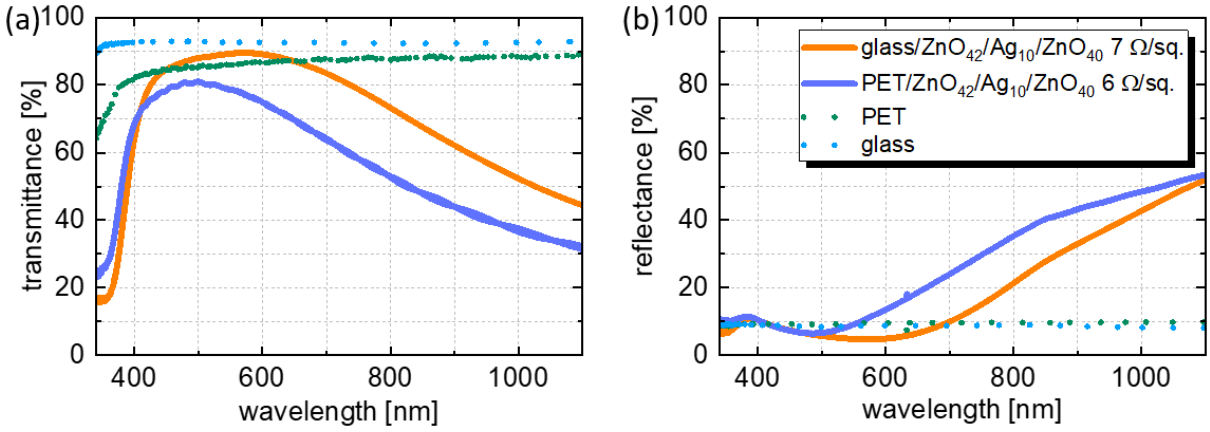

Figure 4.1-6: Transmittance measurements of ZnO/Ag/ZnO electrodes on glass and PET showing higher transmittance for the electrode on glass (a). Reflectance measurements of ZnO/Ag/ZnO electrodes on glass and PET showing that the transmittance losses of the electrodes stem mostly from reflection rather than absorption (b).

ZnO as dielectric for DMD electrodes already delivered reasonable results. Doping intrinsic ZnO with Al (Al:ZnO (AZO)) would lead to even better performances as Al enhances the ZnO conductivity and the stability.[141] Furthermore, doping shifts the work function to 3.7 eV and the band gap to 3.6 eV, compared to undoped ZnO.[142]

Detailed studies of AZO/Ag/AZO electrodes were carried out to see if enhanced performance in comparison to the undoped ZnO could be achieved. First simulations to determine the optimized AZO layer thicknesses were carried out. The used *n* and *k* values are shown in Figure 4.1-7 (a). The values are in general the same as in the previous dispersion relation except for AZO. Due to doping, AZO shows a lower refractive index than ZnO but the same extinction coefficient.

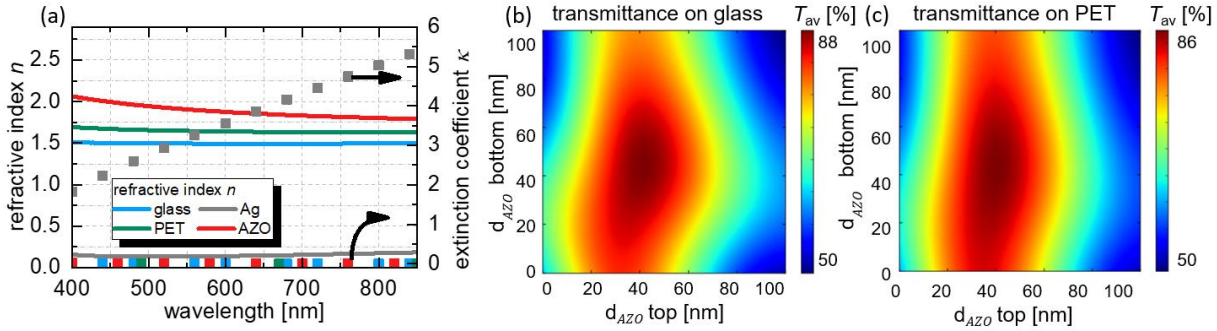

Figure 4.1-7: Refractive indices and extinction coefficients of glass, PET, Ag and AZO (a) used for the simulations to yield the heat map of transmittance on glass (b) and PET (c).

Optimum layer thicknesses were taken from the simulations shown in Figure 4.1-7 (b-c). For glass, d_{AZO} = 44 nm at the bottom and d_{AZO} = 42 nm at the top was obtained, while the simulation for PET yielded d_{AZO} = 42 nm at the bottom and d_{AZO} = 40 nm at the top. These values are similar to the values of the ZnO based DMD because of the similar refractive indices.

Following the simulation, glass and PET substrates were sputter coated with the calculated AZO layer thicknesses sandwiching the 10 nm thick silver layer. As a starting point, the morphology of the electrodes was studied. Figure 4.1-8 shows SEM images of the AZO/Ag/AZO electrode on glass (a) and on PET (b). For both cases the same growth mode can be observed. A closed layer structure with small grains was achieved. The closed films lead to sheet resistances of 6 Ω/sq for glass and 6 Ω/sq for PET. Although the same approximate grain size is obtained, one can clearly see the influence of the substrate on the film surface roughness like in the case of ZnO/Ag/ZnO. On PET (Figure 4.1-8 (b)), larger wave-like structures are observable compared to the morphology of the electrode on glass (Figure 4.1-8 (a)). To quantify these larger structures in terms of roughness, SFM measurements were carried out.

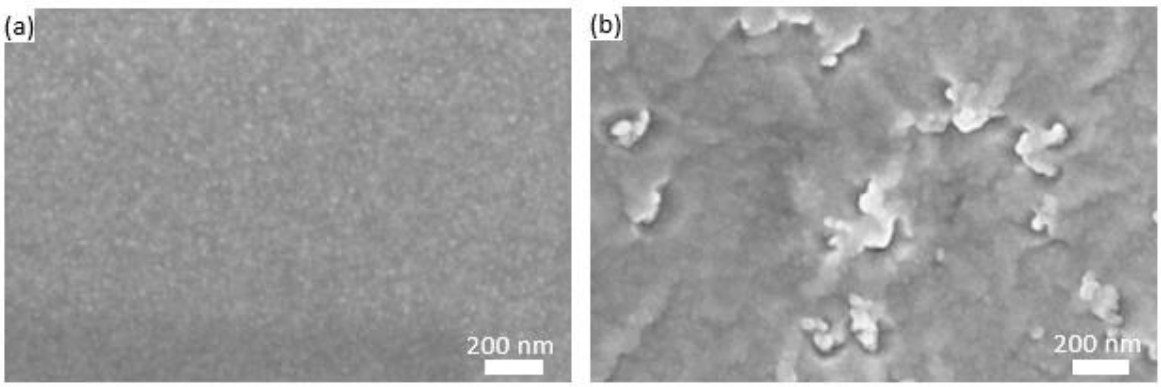

Figure 4.1-8: SEM images of AZO/Ag/AZO electrode on glass (a) and PET (b), showing the same behavior as the previous ZnO/Ag/ZnO electrode.

Figure 4.1-9 shows SFM images of the AZO/Ag/AZO electrode on glass (a) and PET (b). For glass, the same closed layer morphology as in the SEM images is observed (Figure 4.1-8 (a)). The small grains yield a roughness of 1.0 nm. On PET (Figure 4.1-9 (b)) the larger roughness of the initial substrate is observed as in the SEM images (Figure 4.1-8 (b)). The larger initial substrate roughness (Figure 4.1-1) leads to a RMS roughness of 4.7 nm.

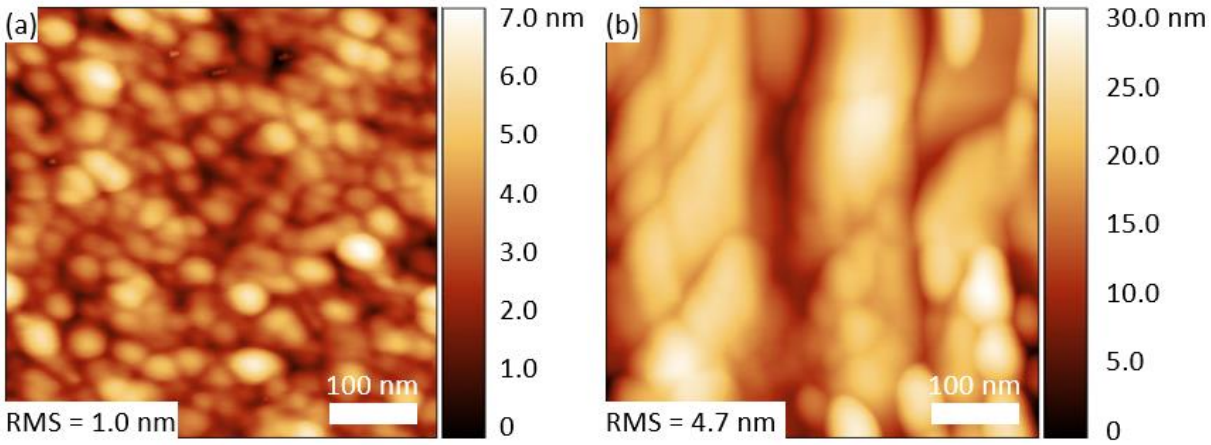

Figure 4.1-9: SFM images of AZO/Ag/AZO electrode on glass (a) and PET (b), showing the same behavior as the previous ZnO/Ag/ZnO electrode.

Figure 4.1-10 shows the transmittance spectra of the AZO/Ag/AZO electrodes on glass (a) and PET (b). In general, a similar behavior as for the undoped ZnO/Ag/ZnO electrode is observed. The observed roughness difference between glass and PET seems to influence the transmittance because T_{av} on glass equals 85.9 % which is close to the simulated value. However, T_{av} on PET is 78.7 % since this difference in transmittance is not caused by reflectance as Figure 4.1-10 (b) shows. It can be concluded that this amount of light is absorbed due to the roughness of the electrode.

The similar reflectance of glass and PET can be explained by a better refractive index matching of the PET/AZO interface compared to the PET/ZnO interface.

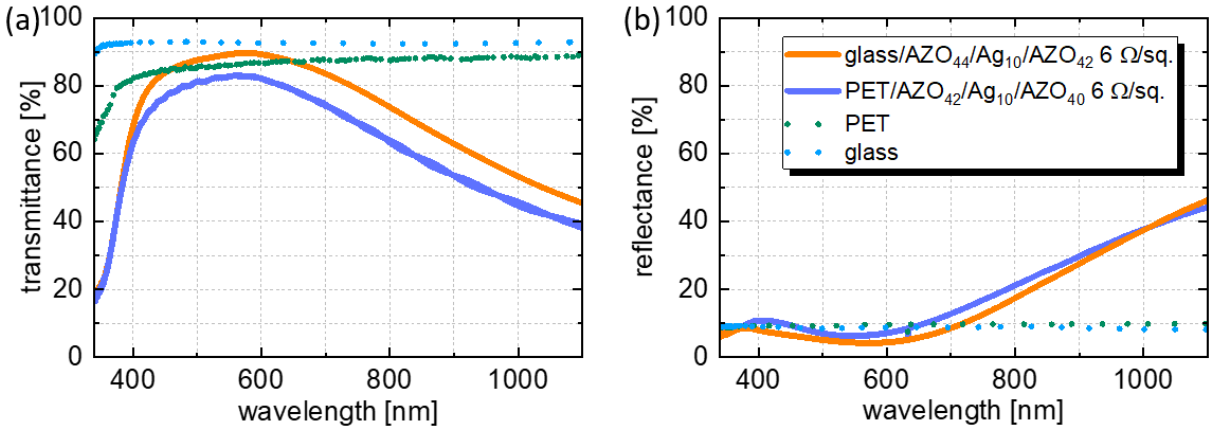

Figure 4.1-10: Transmittance measurements of AZO/Ag/AZO electrodes on glass and PET showing higher transmittance for the electrode on glass (a). Reflectance measurements of AZO/Ag/AZO electrodes on glass and PET showing that the losses of the electrode stem mostly from reflection rather than absorption (b).

Table 1 summaries the key features of the first ZnO based DMD electrodes. Due to the constant silver layer all DMDs show the same R_{sh} on glass and PET. The transparency of the DMDs is in general higher on glass than on PET. On PET, all DMD architectures delivered lower transmittance values as on glass due to the initial PET roughness causing a rougher metal film (Table 1) what causes higher absorbance. Compared to ITO/Ag/ITO with a transmittance of 83.5 % (at 6.7 Ω/sq) on glass[123] and a transmittance of 82.4 % (at 9 Ω/sq) on PET[63], similar results were achieved on glass but not yet on PET.

Table 1: Summary of Transmittance, sheet resistance and roughness values of different ZnO based DMD electrodes:

DMD	**T_{av} [%]** **glass/PET**	**R_{sh} [Ω/sq]** **glass/PET**	**RMS [nm]** **glass/PET**
ZnO/Ag/ZnO	86.0/75.1	7/6	1.1/4.7
AZO/Ag/AZO	85.9/78.7	6/6	1.0/4.7

4.1.2 DMD electrodes using TiO_x/Ag/AZO on bare PET substrates

Part of the content of this chapter is based on work that has been published and was partly modified: Kinner, L. *et al.:* Polymer interlayers on flexible PET substrates enabling ultra-high performance, ITO-free dielectric/metal/dielectric transparent electrode. *Mater. Des.* **168**, 107663 (2019).

As shown in the previous section, ITO/Ag/ITO on PET was not yet outperformed by the tested DMD electrodes on PET in terms of transmittance and conductivity. Hence, a further improved approach is needed to achieve higher transmittance than the previous presented ZnO/Ag/ZnO and AZO/Ag/AZO electrodes.

Further improvement of transmittance can be achieved by using higher refractive index materials to further suppress reflection from the metal.[10] The use of TiO_x would be beneficial as interlayer between substrate and metal. Optimal transmittance of 89 % with R_{sh} < 6 Ω/sq was recently achieved for a sputtered TiO_2/Ag/AZO (TAA) electrode deposited on glass.[62] The reported T_{av} for the TiO_2/Ag/AZO electrode on PET is 82.4 % (no value was given for the R_{sh}). However, no specific information was given about the processing of these electrodes on a PET substrate.[62] In this section, it is shown that the processing of this electrode on PET is problematic due to the morphology of the reactively sputtered TiO_x.[143] A detailed investigation on the design, fabrication and properties of a TiO_x/Ag/AZO electrode on a (modified) PET substrate is presented.

The simulations were used to extract the dielectric layer thicknesses that maximize T_{av}, in the range of 400-700 nm. The Ag layer thickness was again kept constant at 10 nm in the simulations. Figure 4.1-11 (a) shows the dispersion relations of the used materials. In comparison to the previously shown dispersion relations TiO_x shows the highest refractive index so far. Figure 4.1-11 (b) and (c) show heat maps of the simulated T_{av} in the range of 400-700 nm in dependence of the TiO_x (bottom) and AZO (top) thickness for glass and PET substrates. On glass, maximum T_{av} of 90 % is achieved for a TiO_x and AZO thickness of 27 nm and 51 nm, respectively. Optimum dielectric layer thicknesses on PET are the same as for glass, with the maximum T_{av} 88 %. Lower maximum T_{av} is caused by the slightly higher refractive index of PET (n = 1.647 at 550 nm) compared to glass (n = 1.525 at 550 nm). Simple calculation of the reflectance losses for normal light incidence using the Fresnel equations yields approximately 4 % losses for the air/glass and 6 % for the air/PET interface.

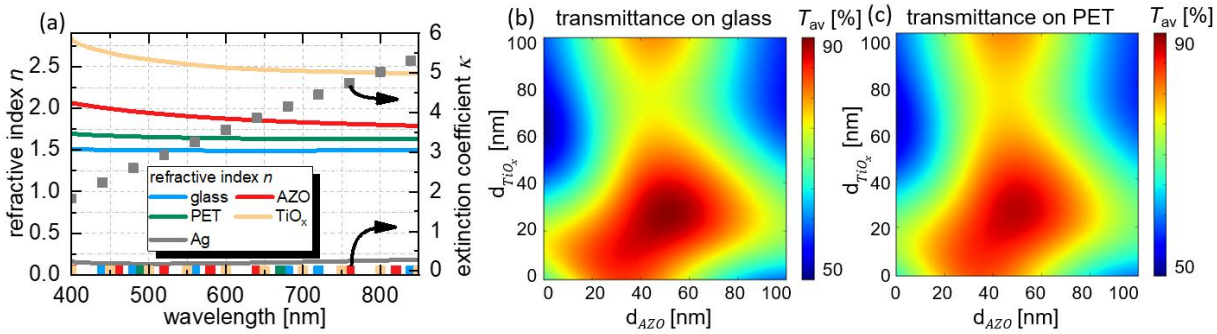

Figure 4.1-11: Refractive index and extinction coefficients of glass, PET, Ag, TiO_x and AZO (a) used for the simulations to yield the heat map of transmittance on glass (b) and PET (c). Taken from [61] and partly modified.

Glass and PET substrates were sputter-coated with the TiO_x/Ag/AZO layers, implementing the simulated, optimal dielectric layer thicknesses of 27 nm for TiO_x and 51 nm for AZO. Figure 4.1-12 (a) shows the transmittance spectra for the 27 nm TiO_x layer on glass and PET. The transmittance of the layer on the PET substrate is higher than on glass. This can be attributed to differences in the refractive index contrast between TiO_x (2.530 at 550 nm) and the substrate (1.525 and 1.647 for glass and PET respectively). Hence, reflectance at the glass/TiO_x interface is higher than on the PET/TiO_x interface while absorption is equal.

Figure 4.1-12 (b) illustrates that the deposition of Ag on TiO_x causes significant transmittance losses that are far more pronounced on PET than on glass. On glass, the transmittance at 550 nm, (T_{550}), is 70 % and the R_{sh} 9.4 Ω/sq. On PET, T_{550} = 40 % and the sheet resistance lies in the kΩ range. The low transmittance values and the high sheet resistance of the bilayer on PET strongly suggest, that the Ag layer is not continuous as will be confirmed later. This is not the case for the glass substrate. Figure 4.1-12 (c) shows the spectra for the complete TAA on glass and PET. It is noted that the bilayers and tri-layers were deposited without any vacuum break, degradation of the silver layer can be excluded as reason for the low R_{sh}.

Although the simulations predicted similar transmittance values, the experimental data shows a large difference between glass and PET. T_{av} on glass is 88.1 %; this fits with the simulation. On PET, T_{av} = 44.8 % and therefore approximately half of the simulated value. Sheet resistance is 5.7 Ω/sq on glass and 29.9 Ω/sq on PET. The significantly lower sheet resistance of the triple layer on PET compared to the bilayer is attributed to the electrical connection of isolated Ag islands by the top AZO layer.

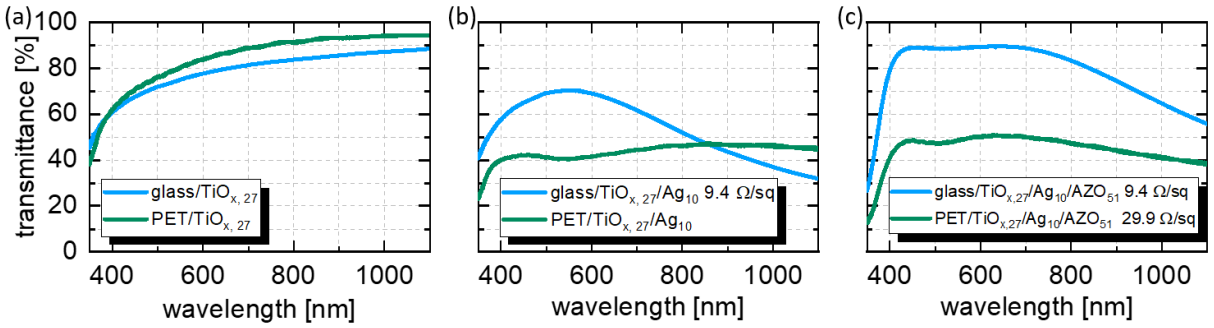

Figure 4.1-12: Transmittance spectra of: substrate/TiO_x (a) showing a higher transmittance for PET/TiO_x due to better refractive index matching. Substrate/TiO_x/Ag showing high losses on PET due to the non-closed Ag film (b). Substrate/TiO_x/Ag/AZO showing perfect reflection suppression on glass and strong transmittance losses on PET (c). Taken from [61] and modified.

The reason for low transmittance and simultaneous high R_{sh} on PET substrates in comparison to glass substrates may result from PET specific properties. As it has been shown in the previous section, PET in general causes a rougher thin film formation due to its higher initial roughness.

Many different PET types are available on the market which may show different film growth behavior, influenced by different surface properties depending on the provider of PET. Further PET can be treated with different surface treatments by the manufacturer to modify surface properties - for instance the wetting behavior. To investigate whether the observations depend on the specific PET type or PET surface type, PET substrates from different providers with either their “treated” side up or not were used and sputtered with TiO_x/Ag. Unfortunately, no exact specification of the treatment was given by any provider.

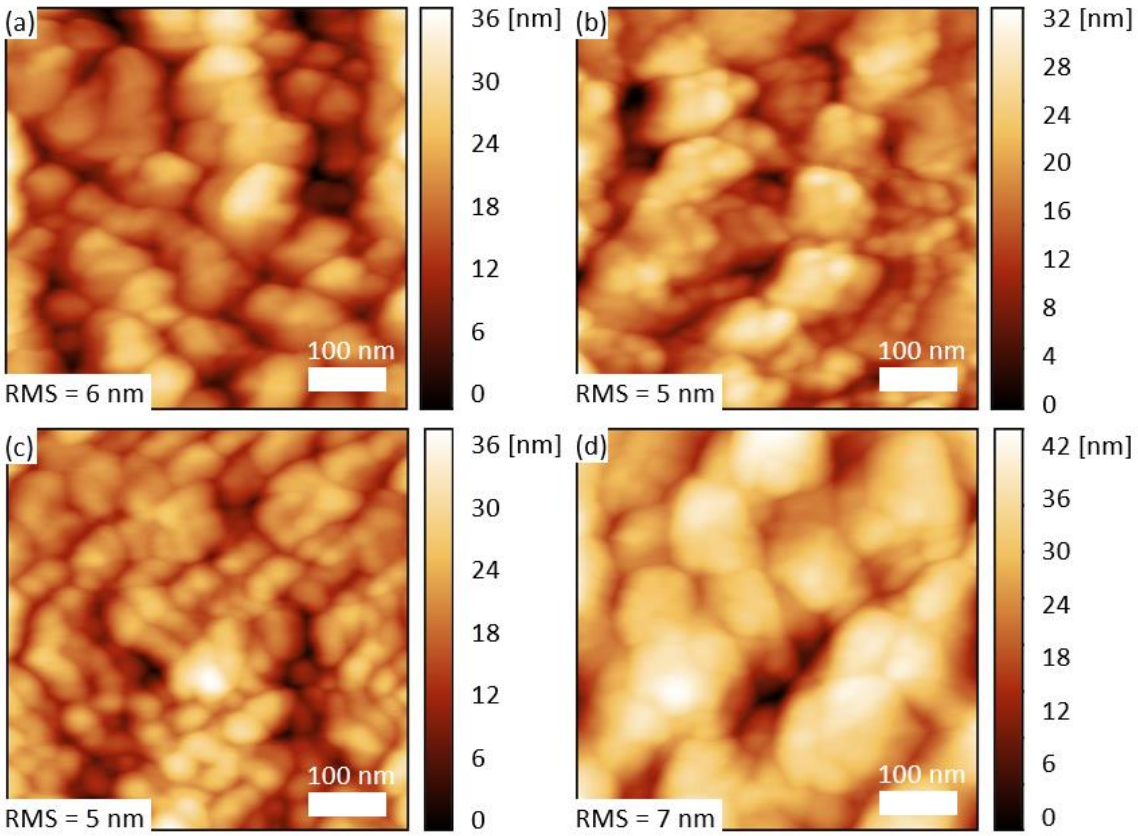

Figure 4.1-13: Bare substrate surfaces of tested PET foils: Lumirror 4001 (untreated) (a); Lum422irror 4231 front (treated) (b); Lumirror 4231 back (untreated) (c); Melinex back (untreated) (d). Taken from [61] and partly modified.

Figure 4.1-13 shows SFM images of the bare surfaces of the tested PET foils from different providers. All surfaces show similar roughness values, inhibiting a closed layer growth. Nevertheless, TiO_x/Ag-layers were sputtered on the different PET types. SEM and SFM images of the corresponding thin films on the same substrates as in Figure 4.1-13 are shown in Figure 4.1-14 and Figure 4.1-15, respectively. Similar growth behavior of the layers can be observed on all PET types and surface treatments. No sample shows a closed layer growth of the TiO_x/Ag. This non-closed, fibrous film formation leads to low transmittance because the film morphology of the silver leads to absorption.

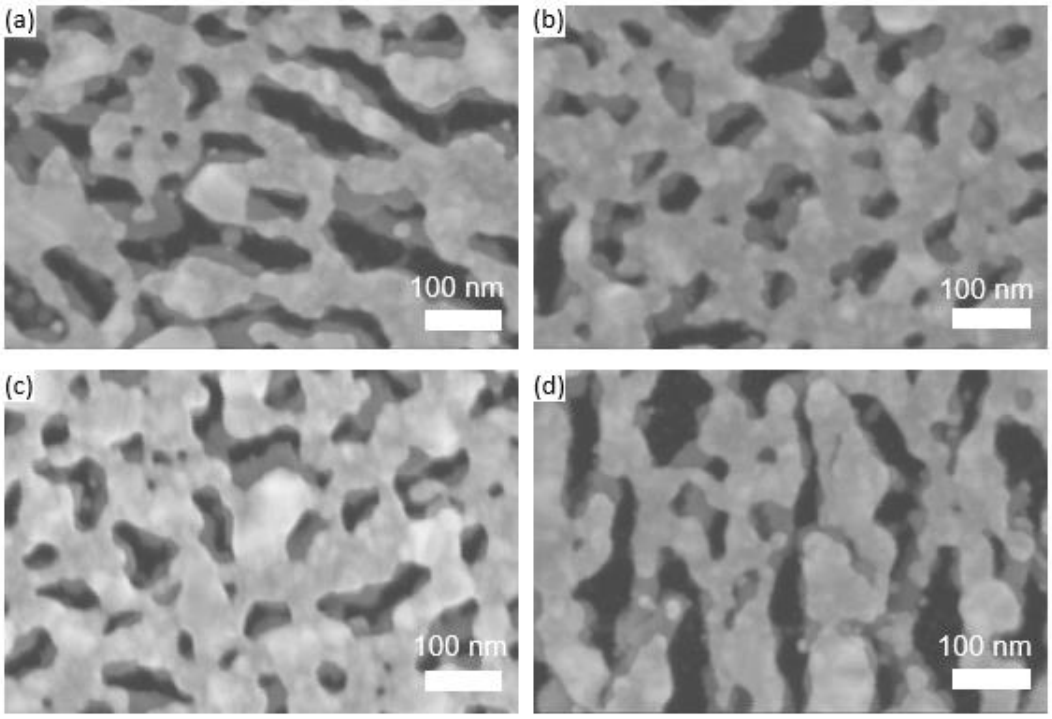

Figure 4.1-14: SEM images of: TiOx/Ag on Lumirror 4001 (untreated) (a); Lum422irror 4231 front (treated) (b); Lumirror 4231 back (untreated) (c); Melinex back (untreated) (d), a fibrous non-closed film morphology is visible independent of substrate. Taken from [61] and partly modified.

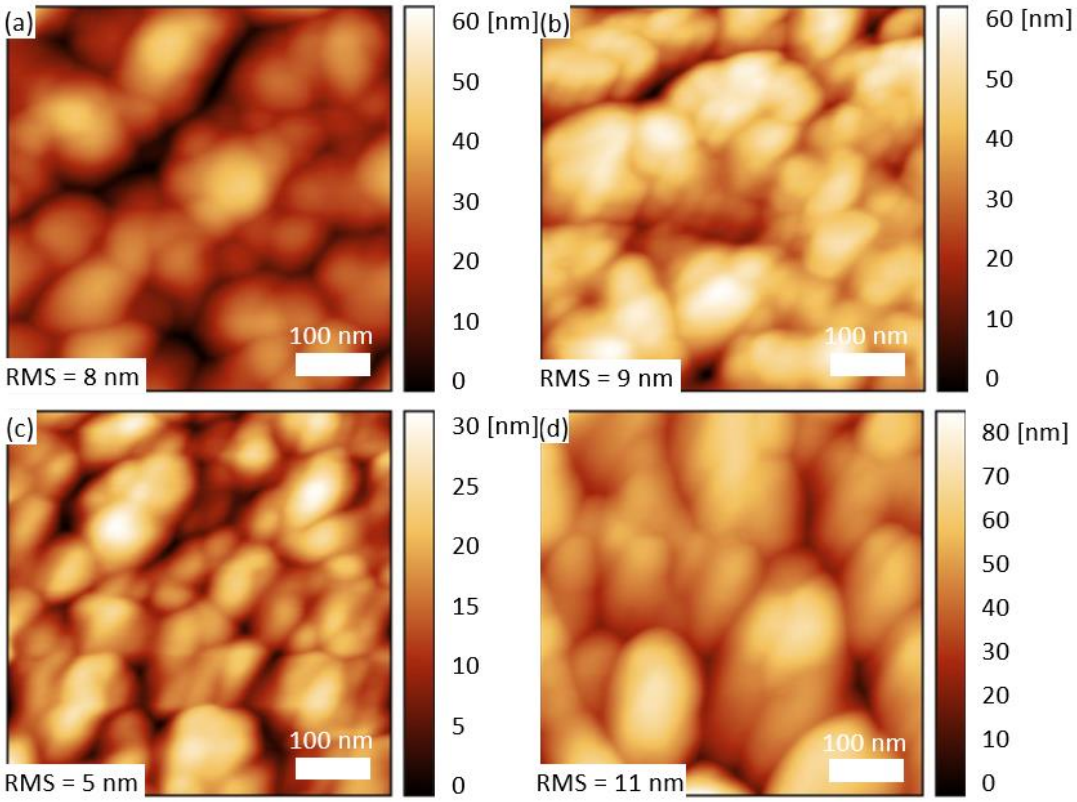

Figure 4.1-15: SFM images of TiOx/Ag on: PET Lumirror 4001 (untreated) (a); Lumirror 4231 front (treated) (b); Lumirror 4231 back (untreated) (c); Melinex back (untreated) (d), independent of substrate is a fibrous non-closed film morphology visible. Taken from [61] and partly modified.

Transmittance measurements of the TiO_x/Ag bilayer on the different PET substrates (Figure 4.1-16 (a)) showed the same behavior as in Figure 4.1-12 (b). Figure 4.1-16 (b) shows the transmittance of the TiO_x/Ag/AZO electrode on the tested PET samples, corresponding to Figure 4.1-12 (c). Although some PET samples show higher transmittance than others, the transmittance is still not as high as expected.

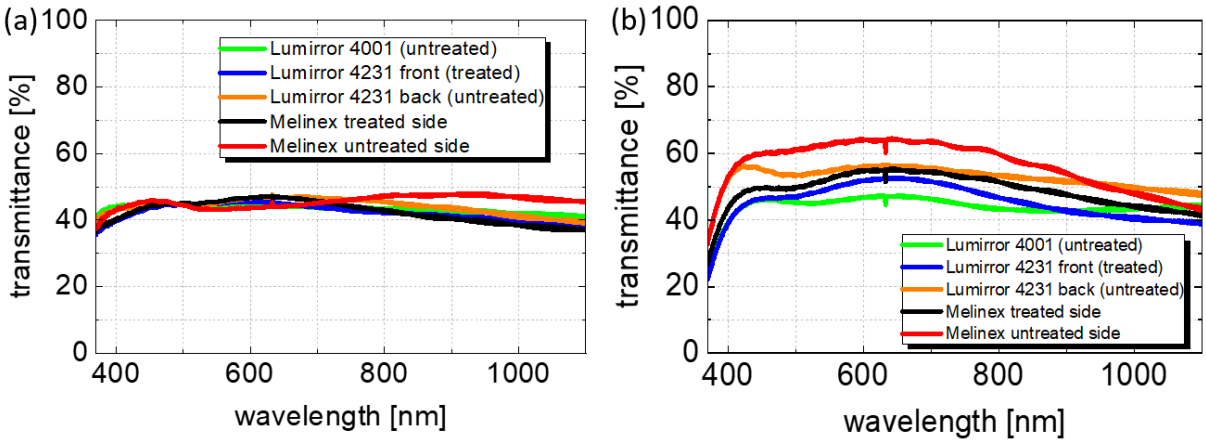

Figure 4.1-16: Transmittance spectra of TiO_x/Ag bilayer on various PET-substrates and surfaces (a) and TiO_x/Ag/AZO tri-layer on various PET-substrates and surfaces (b), a high transmittance electrode is not achieved independent of substrate or treatment type. Taken from [61] and partly modified.

So far, it can be concluded that no matter which PET or treatment type is used, non-closed and fibrous TiO_x/Ag films are formed; this leads to a low transmittance and a high sheet resistance.

TiO_x on PET grows as a non-closed, fibrous structure with wide voids and sharp edges ash shown in Figure 4.1-14. Such a film morphology can be associated with the "hit and stick" (or ballistic) type of film growth, classified as "zone Ia" by Mahieu[144]. This occurs when the substrate is not heated and the arriving particles on the substrate have low kinetic energy. In this case, the diffusion on the substrate is very limited and the nucleation is sparse. Resulting films attain a columnar and rough structure with low density and no preferential orientation as dictated by statistical roughening and self-shadowing effects.[144]

Similar film morphology has been shown in the literature for a radio frequency (RF) reactively-sputtered TiO_x film on a PET substrate.[145] Comparable film morphology was also observed for DC-sputtered TiO_x from an oxide target in pure Ar atmosphere on glass.[146] No substrate heating was applied in both cases. In these reports, the gas pressure was 2 and 1.4 Pa, respectively, which is 20 and 14 times higher than the pressure used in the present work. Large pressure favors the ballistic type of growth due to pronounced scattering of the incoming particles in the plasma. This leads to the conclusion, that pressure can be dismissed as influencing factor in this case, sputter power can be adjusted to foster closed film growth of TiO_x layers.

Generally, an increase of the sputter power causes an increase in the kinetic energy of the particles, which fosters film compactness and less voids. To test this, TiO_x films on PET were sputtered at 160

and 200 W DC power, yielding sputter rates of 0.022 nm/sec and 0.031 nm/sec, respectively. SEM images of the tri-layers and the corresponding transmittance spectra are shown in Figure 4.1-17. Despite the decrease in the roughness of the TiO_x films, the optical transmittance of the tri-layers remained low (Figure 4.1-17 (a)), as the island-like morphology of the film was preserved. Figure 4.1-17 (b) shows the SEM image of the TiO_x/Ag/AZO electrode, where the TiO_x layer was sputtered with 160 W, while in Figure 4.1-17 (c) it was sputtered with 200 W. It can be therefore concluded that although the TiO_x morphology can be improved, it is still inadequate to promote a continuous Ag film, thus compromising the optical property of the electrode.

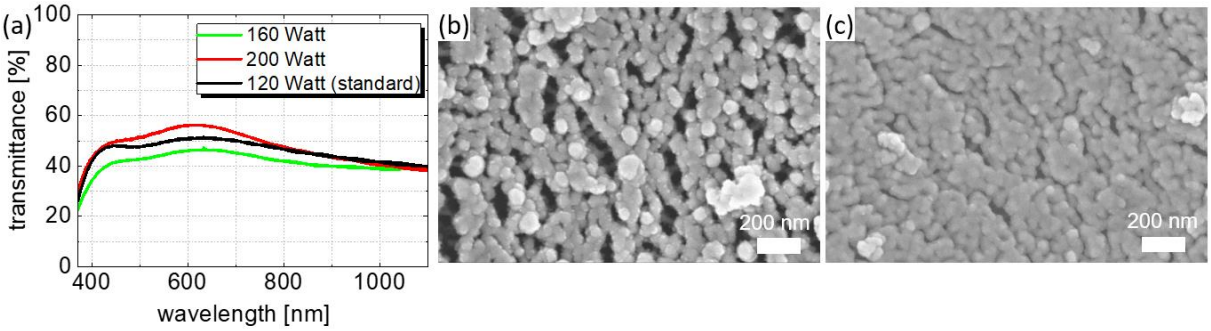

Figure 4.1-17: Transmittance spectra of tri-layer on PET with 120 W (standard), 160 W and 200 W sputter power for the basic TiO_x layer (a), independent of sputter power is the transmittance lower than expected. Scanning electron images of tri-layer on PET with 160 W (b) and 200 W (c) sputter power for the TiOx layer, showing a slightly more closed film for 200 W, but still the transmittance is low. Taken from [61] and partly modified.

The TiO_x film growth may be influenced by surface diffusion of the arriving particles during sputtering. Surface diffusion can be influenced by surface dipoles of the material or adsorbed molecules with an electric dipole like water. Hence, adsorbed water on the PET surface or water contained in the PET bulk may play a role in the obtained TiO_x morphology. To test this hypothesis, the following experiments were conducted: A PET substrate was immersed for 3 days in water, then shortly dried in a nitrogen stream before being transferred in the sputter tool. A second PET substrate was put for 3 days in a dry-oven (at 70°C) before sputtering. The TiO_x/Ag/AZO electrodes on both samples showed similar properties as the previous ones described above. The transmittance measurements in Figure 4.1-18 (a) demonstrate that the film morphology in both cases is not causing transmittance changes; this is confirmed by the SEM images. In Figure 4.1-18 (b), the SEM image of the “wet” PET sample is shown. A more discontinuous morphology on the “dried” PET (Figure 4.1-18 (c)) is visible. Still, one can conclude that different exposures to water do not influence significantly enough to enhance the TiO_x growth.

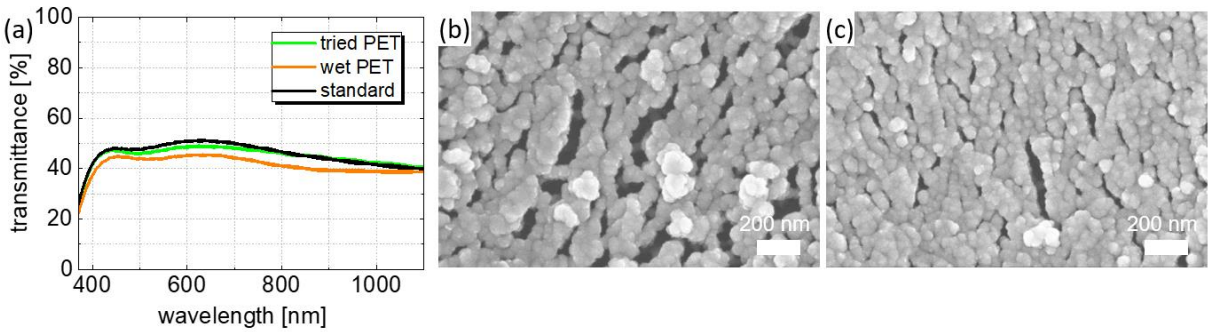

Figure 4.1-18: Transmittance spectra of tri-layer on wet and tried PET, with normal PET as reference (a), showing that water content does not influence transmittance, scanning electron images of tri-layer on wet (b) and dried (c) PET showing that water content does not influence the morphology significantly. Taken from [61] and partly modified.

It is possible that the different morphology of the TiO_x film on PET and glass is due to differences in the sticking coefficients (that depend on the number of dangling bonds on the substrate and the bonding strength) of the sputtered particles and their diffusivities on the substrates. When the chemical bonding is weak, the particles can diffuse onto the substrate and form clusters.[113] On the other hand, when the chemical bond is strong, diffusion and cluster growth are hindered. Functional groups of -COOH, -OH, -C=O are expected on the PET substrate.[147]

To investigate the surface group theory in detail, XPS measurements (Figure 4.1-19 and Figure 4.1-20) where conducted to provide a qualitative chemical analysis of the films grown on glass and PET. 1, 3 and 27 nm thick TiO_x layers were sputtered on glass and PET. The evolution of XPS survey of the different thicknesses are shown in Figure 4.1-19 (a-b). No significant difference can be observed, which indicates no chemical influence on the growth mode. Due to the insulating nature of the substrates employed in these experiments, the spectra measured suffer of charging effects. Even if the samples were grounded during measurement, the charging process occurs since the (photo-) holes left in the samples are not efficiently restored upon the removal of the electrons due to the photoemission process itself. Therefore, all the spectra positions are aligned in binding energy according to the expected value of literature.

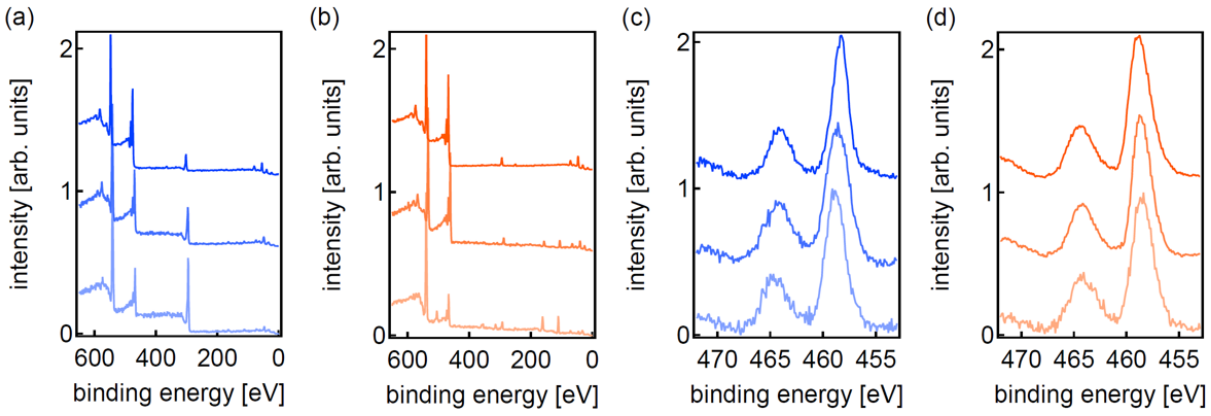

Figure 4.1-19: Evolution of XPS survey on PET (a) and on glass (b) Evolution of Ti2p core level signal on PET (c) and on glass (d) for the TiO_x film grown on PET and glass, respectively. Special thanks go to Dr. Giovanni Ligorio who performed this XPS measurements. Taken from [61] and partly modified.

All the spectra of Ti2p (see Figure 4.1-19 (c) and (d)) for both substrates and for all three TiO_x thicknesses (1, 3 and 27 nm) are very similar and to do not reveal any chemical difference between the films grown on PET or on glass.

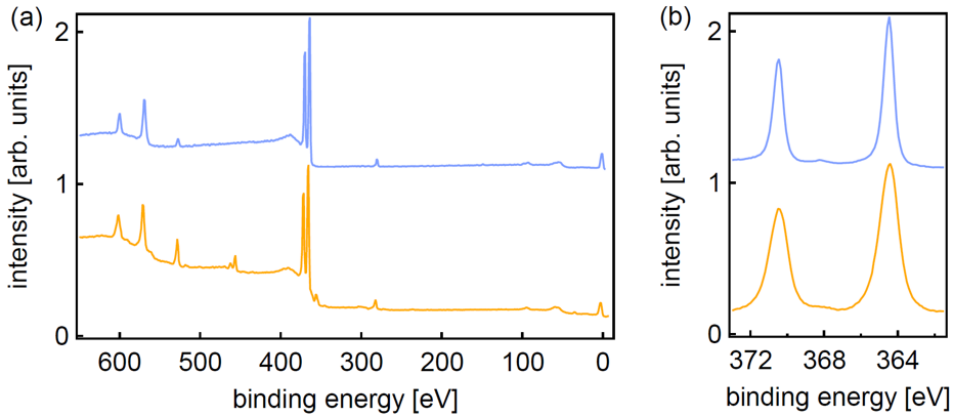

Figure 4.1-20: XPS survey signal (a) and Ag3d core level spectra (b) measured on 10 nm Ag sputtered on 27 nm TiO_x grown on PET (orange spectra) and glass (blue spectra). Special thanks go to Dr. Giovanni Ligorio who performed this XPS measurements. Taken from [61] and partly modified.

On both substrates, onto the 27 nm of TiO_x a film of Ag was grown with a nominal thickness of 10 nm. The XPS survey signal Figure 4.1-20 coming from the sample on PET displays a peak at 460 eV related to Ti2p. Considering the high surface sensitivity of photoemission spectroscopy, the XPS signals suggest that the Ag film is not homogeneous and do not form a complete metallic layer on the TiO_x film. This is further confirmed looking at the Ag3d core level spectra: the signal from the sample on PET displays an evident broadening with respect to the spectra collected on glass. Furthermore, the binding energy position of the Ag3d on PET has been shifted of approximately 9 eV in order to be aligned properly to the value expected for a metallic Ag film. This demonstrates the charging effects occurring on Ag (although the sample was grounded) and hence depicts a film which is not complete. Despite the

shifting of the peaks due to the not closed Ag layer, no chemical difference in growth mode could be observed between glass and PET.

Morphology differences between TiO_x on glass and PET may be caused by etching of the PET substrate in the oxygen containing plasma. This can happen as a result of the low sputter rate of TiO_x, which does not cover the PET surface fast enough to save PET from etching.[148–152] Tilted-angle SEM images (Figure 4.1-21 (a)) confirm the non-closed, fibrous growing of the TiO_x film. In Figure 4.1-21 (b), the larger magnification shows that Ag (light grey) only is agglomerating on the pillar like grown TiO_x (dark grey).

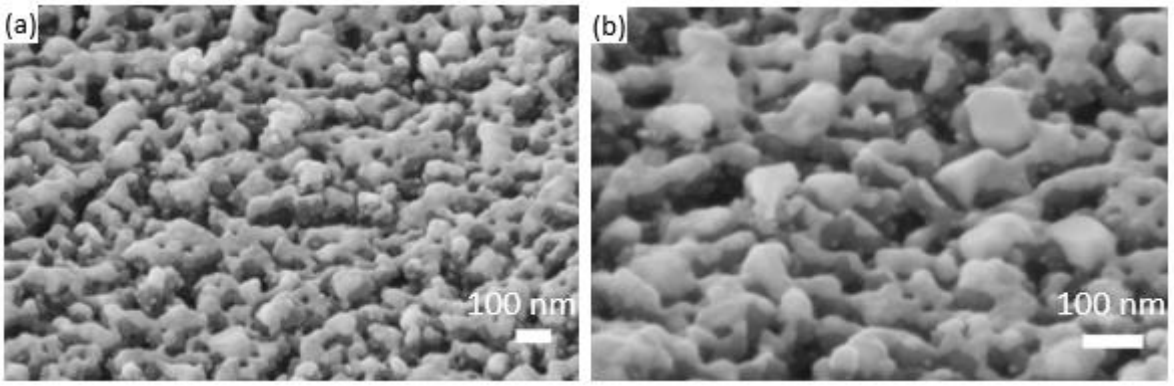

Figure 4.1-21: Tilted-angle SEM images of TiO_x/Ag on PET. Tilting angle was 52.2°. Two different magnifications are shown (a) and (b), showing that TiO_x (dark grey) grows in a non-closed film, which forms a non-closed base for the Ag film (white). Taken from [61] and partly modified.

So far, intrinsic PET composition, different sputter powers, different water contents, surface wettability and surface etching by the sputter plasma can be excluded from influencing the different growth mode of TiO_x between PET and glass.

The differences in the substrate roughness between glass and PET, combined with the low kinetic energy of the sputtered species during TiO_x deposition, is the most plausible explanation for the distinctive morphological features between PET and glass. Bare glass has a roughness of 1.5 nm RMS, while bare PET shows a RMS roughness of 15 nm, as measured by SFM. It can be anticipated that the particle diffusion length is limited by the high substrate roughness, which can explain the observed differences in the film growth. This is supported by the work of Assis et al.[153] on the roughness evolution of thin films as a function of the initial substrate roughness.

To back up the theory of the influence of initial roughness on sputtering, a comparison of different PET/metal-oxide/Ag layers in a SEM study is shown in Figure 4.1-22. Figure 4.1-22 shows ZnO/Ag (a), AZO/Ag (b), ITO/Ag (c) and TiO_x/Ag (d). It is observable that there are “long-range” wave like background contrast differences in Figure 4.1-22 (a-c). Still, a closed layer is formed by the ZnO, AZO and ITO films on PET. The wave like background contrast differences are in the same size relations as the inhomogeneous grown TiO_x/Ag islands on Figure 4.1-22 (d).

This implicates that arriving TiO_x molecules cannot overcome this surface roughness to form a homogeneous film, while all other tested materials could.

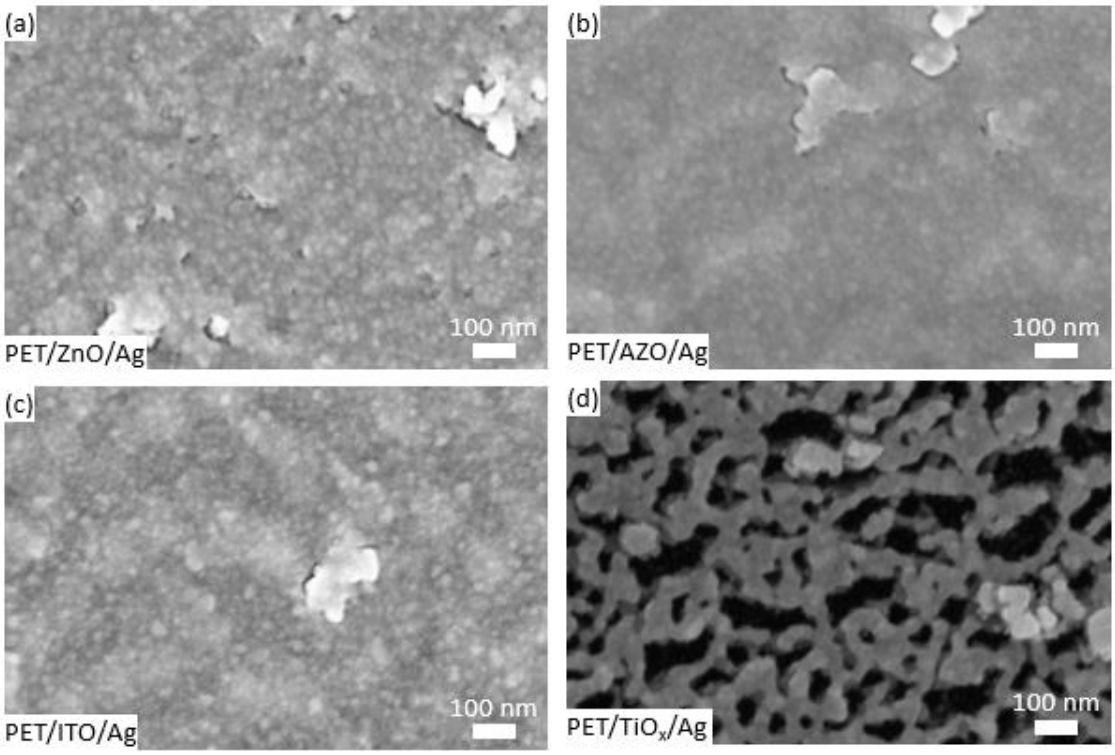

Figure 4.1-22: Comparison of growth modes of different metal oxides on PET, ZnO/Ag (a), AZO/Ag (b), ITO/Ag (c), TiOx/Ag (d), showing that only TiO_x does not grow in a closed layer on PET.

4.1.3 DMD electrodes using TiO_x/Ag/AZO on PET with different polymer interlayers

In the previous section it was observed that TiO_x films which form the basis of the most promising DMD electrode do not form a closed layer on PET during sputtering. Nevertheless, the TAA electrode performance on PET lacked far behind the performance on glass. Different experiments to find out the influencing factor for this growth behavior were carried out and different approaches to foster closed film growth of the TiO_x layer on PET were presented. However, a closed film structure of TiO_x was not achieved. The most plausible explanation of the different film morphologies on glass and PET was the intrinsic roughness of the PET substrates.

To influence TiO_x growth on PET by flattening the PET surface on a microscopic scale, PET was coated with Amonil® or PMMA. Influencing the TiO_x morphology should lead to improved optical and electrical properties of the electrode. UV-crosslinked organic-inorganic composite materials like Amonil® show enhanced chemical and mechanical stability and are therefore expected to withstand plasma processes.[154,155] Further, they show a similar refractive index to glass and a similar expected adatom surface diffusion.[156] According to the manufacturer, Amonil® is a hybrid organic/inorganic composite material. The organic part includes non-polymerized methacrylate groups with matrix formation via methacrylic polymerization and polycondensation with silicic acid. The inorganic part contains silicic acid ester and other metal alkoxides (e.g. zirconium alkoxide). Additives include silanes with perfluorinated alkyl groups and photo-initiator for free radical cross-linking. A solvent appropriate for layer thickness adjustment is used. In terms of optical properties, the refractive index is similar to glass (1.55 at 400 nm to 1.50 at 900 nm), with negligible extinction coefficient in the spectral range of interest.[156]

PMMA was also tested as an alternative polymer. PMMA is widely used as a positive tone electron beam resist, which can be modified only by high energy electron beams (>3 keV)[157] and is stable in O_2 plasma[158,159]. For the optical constants we find a refractive index of 1.30 at 400 nm rising to ~.50 at 900 nm, but with a decrease to 1.20 at 600 nm.[160] The extinction coefficient of PMMA is negligible within the wavelength range of interest.[161]

Figure 4.1-23 (a) shows a SEM image of the TiO_x/Ag bilayer on glass. Film morphology is compact with no distinctive and abrupt topographic features. On PET (Figure 4.1-23 (b)), a very different picture is observed. The glass/TiO_x/Ag stack (a) shows a low RMS roughness of 1.0 nm, due to the closed layer morphology. The SFM image of the PET/TiO_x/Ag stack Figure 4.1-23 (b) corroborates the previous SEM observation, as it shows high RMS roughness of 17.3 nm and terraces with height in the order of 70 nm. This height is larger than the total equivalent film height of the TiO_x and Ag and is due to the incomplete coverage of the substrate surface. Figure 4.1-23 (e-f) present SEM images of the TiO_x/Ag/AZO stack on glass and PET. On the PET substrate voids in the film can be observed, which are nevertheless less

pronounced than in the bilayer case, as the AZO film partially fills the voids. Figure 4.1-24 (a-b and e-f) depict the corresponding SFM images. On glass, the RMS roughness is 1.1 nm. On the PET substrate, the addition of AZO reduces the RMS roughness to 8.4 nm. AZO connects the Ag islands and hence a drastic drop of the sheet resistance takes place, as shown earlier. These morphological observations once more explain the low transmittance and the high sheet resistance on bare PET shown in the previous section.

SEM images in Figure 4.1-23 (c-d) show that Amonil® (250 nm thickness) and PMMA (300 nm thickness) promote glass-like film growth of TiO_x. The SFM images in Figure 4.1-24 confirm the SEM observation and quantify the roughness values. On PET/Amonil® the TiO_x/Ag bi-layer has a RMS roughness of 3.2 nm and a peak-to-peak height of 20.0 nm. On PMMA the RMS roughness is 4.1 nm and the peak-to-peak height is 31.0 nm. Adding AZO to the bilayer does not change much in terms of roughness, as confirmed by SFM images (Figure 4.1-24).

RMS roughness of the TiO_x/Ag/AZO stack on Amonil® is 1.7 nm with a peak-to-peak height of 12.4 nm. The same stack on PMMA yields values of 3.7 nm and 28.5 nm, respectively. On both interlayers, the TiO_x/Ag/AZO stack has similar morphology as on glass. (Figure 4.1-23 and Figure 4.1-24 (g-h))

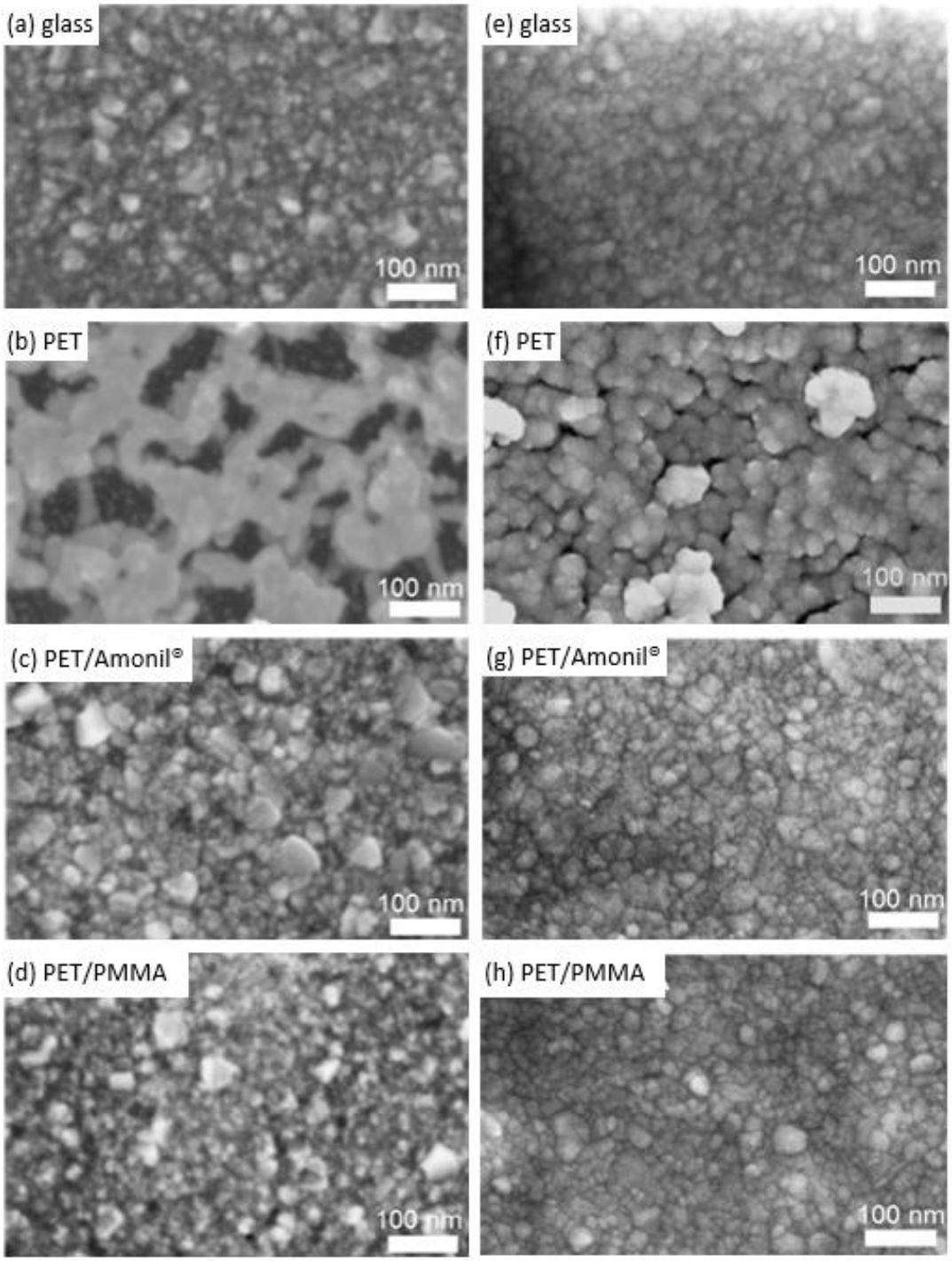

Figure 4.1-23: SEM images of TiOx/Ag and TiOx/Ag/AZO on glass (a) and (e), PET (b) and (f), PET/Amonil® (c) and (g) and PET/PMMA (d) and (h). Showing that a glass like morphology is achieved on PET if Amonil® or PMMA is used as interlayer. Taken from [61] and modified.

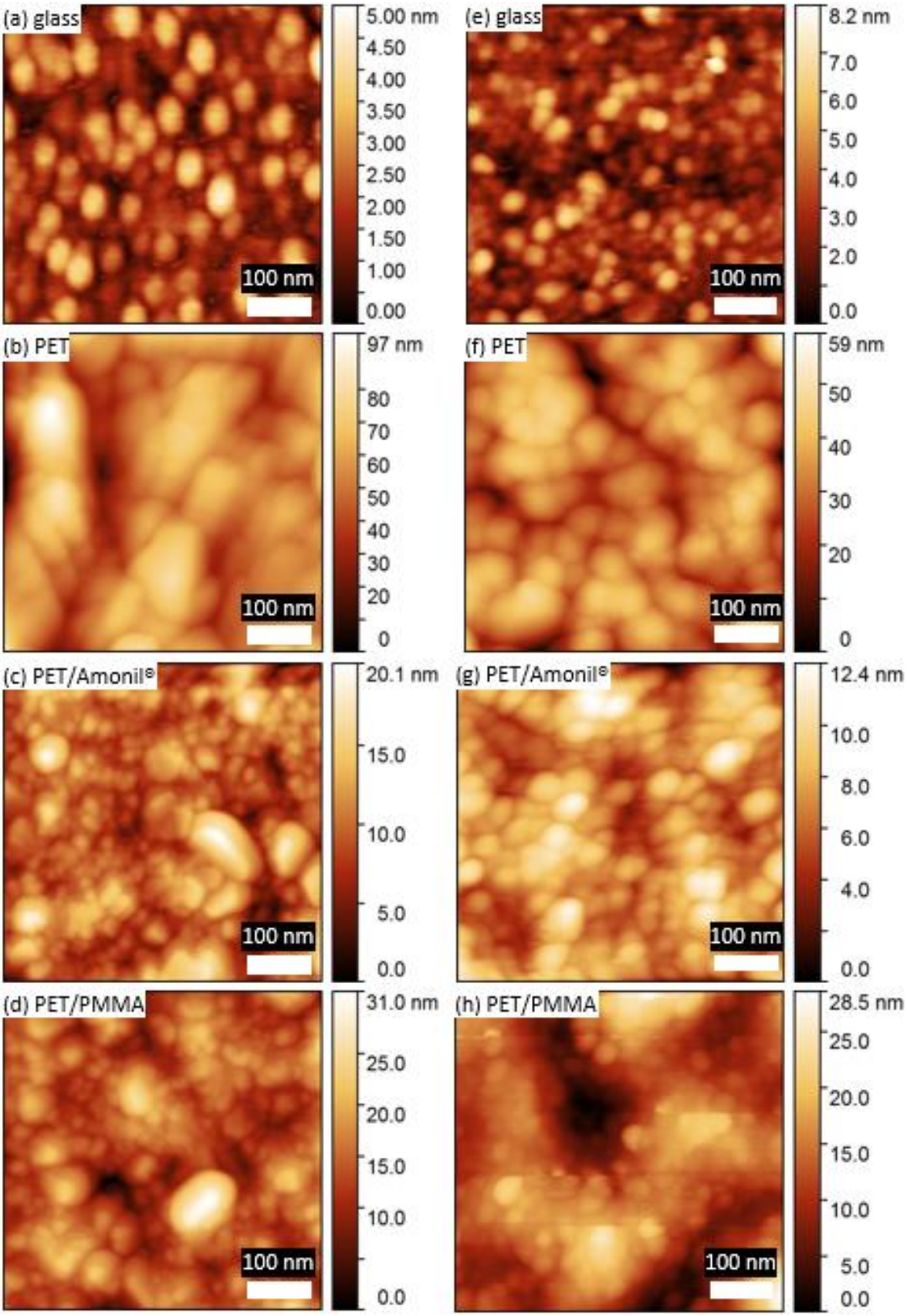

Figure 4.1-24: SFM images of TiO_x/Ag on: glass (a), PET (b), PET/PMMA (c) and PET/Amonil® (d). SFM images of TiOx/Ag/AZO on: glass (e), PET (f), PET/PMMA (g) and PET/Amonil® (h). Showing that a glass like morphology is achieved on PET if Amonil® or PMMA is used as interlayer. Taken from [61] and modified.

It is expected that the closed TiO_x and subsequent closed Ag layer show higher transmittances due to less absorption and lower R_{sh} as the non-closed layers. To quantify this morphological impact on optical performance, optical characterization of the TiO_x/Ag/AZO stacks on glass, bare PET, PET/Amonil® and PET/PMMA was performed. Figure 4.1-25 (a) presents the transmittance spectra. Owing to the Amonil® layer, T_{av} increases from 44.8 % to 85.1 %. The developed electrode has a higher transmittance than the bare PET substrate in the range from 483 nm to 622 nm. Achieved T_{av} surpasses the highest value reported for a TiO_x/Ag/AZO electrode on PET in the literature, which is 82.4 % in the 400-700 nm range.[62] T_{550} also rises from 47 % on bare PET to 87 % with the interlayer. Additionally, a significant decrease in sheet resistance is observed, from 29.9 Ω/sq to 5.7 Ω/sq. Performance of the TiO_x/Ag/AZO electrode on glass (blue line, Figure 4.1-25 (a)) is not reached, due to the larger refractive index of PET, causing higher reflectance losses at the PET/air interface (uncoated side of the substrate) compared to the glass/air interface. With the PMMA interlayer, a rise in transmittance is also achieved compared to the bare PET. Although the TiO_x/Ag/AZO electrodes on PMMA underperform compared to those on Amonil®, the former could be used as a lower-cost alternative.

Figure 4.1-25 (b) displays the reflectance spectra. Bare PET has an average reflectance of 10 %. PET/TiO_x/Ag/AZO yields an average reflectance of 14 %. Through the use of Amonil® and PMMA, the reflectance of the electrode is decreased to 7 % and 8 %, respectively, thus obtaining lower reflectance than bare PET. This confirms the proper design and fabrication of the flexible TiO_x/Ag/AZO electrode. For comparison, the TiO_x/Ag/AZO on glass yields reflectance of 6 %.

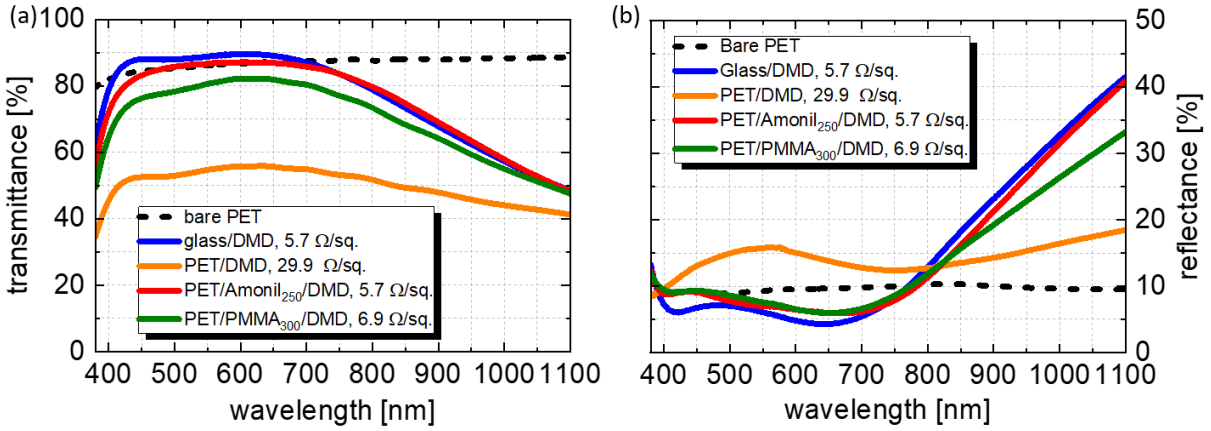

Figure 4.1-25: Transmittance (a) and reflectance (b) spectra of bare PET, glass/TiO_x/Ag/AZO, PET/TiO_x/Ag/AZO, PET/Amonil®$_{250}$/TiO_x/Ag/AZO and PET/PMMA300/ TiO_x/Ag/AZO. Showing that the glass like morphology achieved on PET with Amonil® or PMMA as interlayer leads to higher transmittance values. Taken from [61] and modified.

Figure 4.1-26 (a) and (b) show the effect of the Amonil® thickness on the electrode's optical performance. The 550 and 800 nm thick interlayers lead to a pronounced interference pattern in the spectra. It is observed that the interlayer thickness can be reduced to 80 nm without significant reduction of the transmittance. That said, the optimum interlayer thickness that yields maximum *T*

(T_{max}) of 85.1 % (87.0 %), is 250 nm. Sheet resistance stays practically constant for all thicknesses ranging from 4.9-5.9 Ω/sq. Key performance values for the electrodes are summarized in Table 1. Haacke's figure-of-merit, $\Phi=(T^{10}/R_S)$, for transparent electrodes, is also included in the table, using either the average transmittance $T=T_{av}$ (Φ_{av}) or the one at 550 nm $T=T_{550}$ (Φ_{550}).[162]

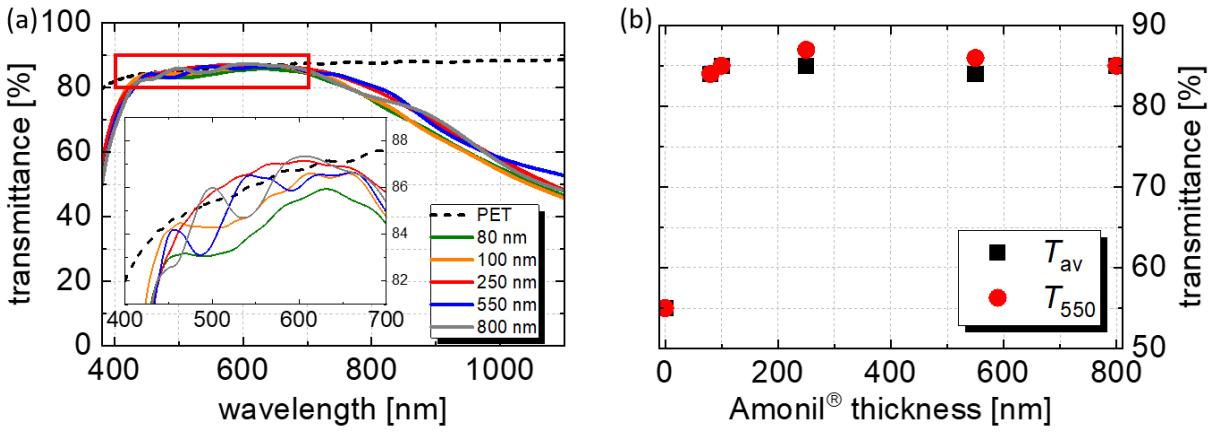

Figure 4.1-26: Transmittance spectra for various Amonil® layer thicknesses (a), the inset shows a zoom in the visible range. T_{av} and T_{550} versus interlayer thickness indicating an optimum layer thickness of 250 nm for Amonil® (b). Taken from [61] and modified.

Table 2 sums up the transmittance and conductivity increase of the TAA electrode on PET due to the use of hybrid and organic interlayers. Although Haacke's figure of merit suggests high differences in the performance, the transmittance and R_{sh} values of the PET/Amonil® are outstandingly high.

Table 2: Summary of TiO_x/Ag/AZO electrode properties on different substrates.

substrate	**RMS [nm]**	**T_{av} [%]**	**T_{550} [%]**	**R_{sh} Ω/sq]**	**Φ_{av} [10^{-3}/Ω]**	**Φ_{550} [10^{-3}/Ω]**
glass	1.1 ± 0.1	88.1	90	5.7	49	61
PET	8.4 ± 1.5	44.8	47	29.9	0.011	0.018
PET/AMONIL®$_{250}$	1.7 ± 0.1	85.1	87	5.7	35	44
PET/PMMA$_{300}$	3.7 ± 2.3	79.0	81	6.9	14	18

The TiO_x/Ag/AZO electrodes on glass and PET (with and without interlayer) were characterized by XRD. The diffractograms are shown in Figure 4.1-27. No peak can be assigned to TiO_x indicating that in all cases, the TiO_x is amorphous. On the flexible substrates, the Ag (111), (200), (220) and (311) peaks can be observed, while on glass, only the (111) peak is prominent. Also, the intense (002) and weak (013) peaks of wurtzite ZnO are identified in all samples.

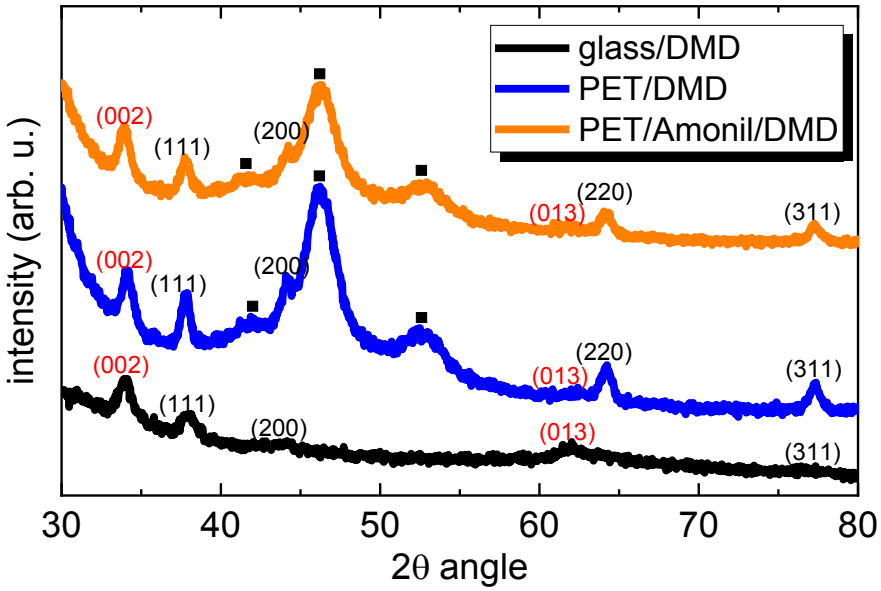

Figure 4.1-27: X-ray diffractograms of the TiOx/Ag/AZO electrodes on glass, PET and PET/Amonil®. Peaks marked with a black rectangle belong to the PET substrate. Taken from [61] and modified.

The scope of the thesis is the development of a flexible TE. The last bottleneck for the developed TE is mechanical stability.[163] For rollable or foldable applications, as in this case where many bending cycles are expected, cyclic bending tests are necessary.[164] To determine the tensile strain ε (film on the outside of the bending curvature) during bending, the formula $\varepsilon = d/2r$ was used.[164] PET substrate thickness d equals 175 µm. By bending the substrate to a radius of 4 mm, a 2.2 % tensile film strain was applied on the TE. Additional to tensile bending, compressive bending (film inside the curvature) was carried out at the same diameter.[165] The change of R in relation to the initial resistance R_0 was measured after the given amount of bending cycles to quantify the conductivity changes. Figure 4.1-28 shows the results of the tests. As stated in the introduction, ITO shows a dramatic R_{sh} increase. Within 10 compressive bending cycles, R_{sh} increases more than 70 times. The R_{sh} of the TAA electrode increases only 3 times over 10000 tensile bending cycles and shows almost no R_{sh} change for compressive bending for 10000 cycles. The larger change of R_{sh} in tensile bending compared to compressive bending is because tensile bending is more strenuous for the film.[164–166]

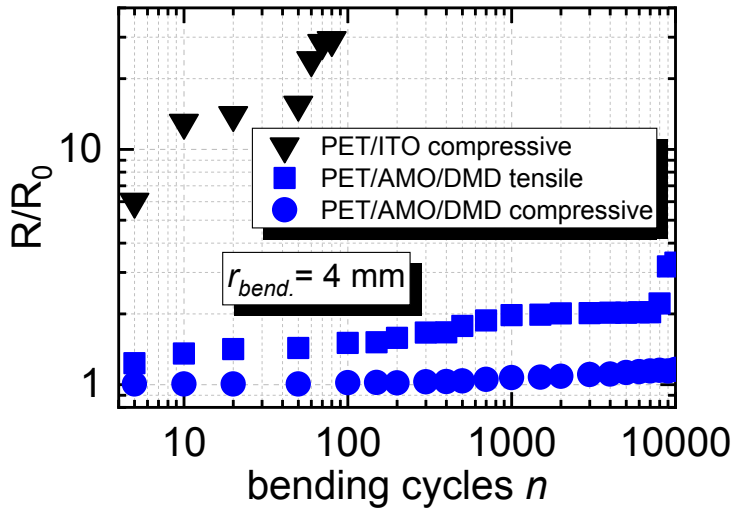

Figure 4.1-28: Bending tests of TAA electrodes showing its superior stability (no change in R_{sh}) over standard PET/ITO substrates (70 times increase).

4.2 OLEDs on selected DMD electrodes

Part of the content of this section is based on work that has been submitted to Advanced Materials Technology and was partly modified: Kinner, L. *et al.*: ITO-free high performance flexible TiO_x/Ag/AZO electrodes for organic light emitting diodes. *Adv. Eng. Mat.* (2020)

In the former section, the TAA electrode was identified as the most promising candidate as a flexible TE. It featured the highest figure of merit of all tested DMD layer sequences as well as the necessary flexibility. To test the device processability and performance of the TAA electrodes, OLEDs were built on the TAA electrode. OLEDs were chosen as test thin film devices as they show a high susceptibility to electric field homogeneity as stated in section 2.3.[92,105–107]

A DMD transparent electrode applied in an OLED device was already presented 2013 by Yun et al..[167] The flexible OLED featured a ZnS(25 nm)/Ag(7 nm)/MoO_3(5 nm) electrode on a polyethylene naphthalate substrate. DMD layers, hole-injection layer (N,N0-bis(1-naphthyl)-N,N0-diphenyl-1,10-biphenyl-4,40-diamine (NPB) and emitting layer tris(8-hydroxyqui-nolinato)aluminum) (Alq3) were thermally evaporated. Power- and current efficacies as well as luminance values showed similar behavior to reference ITO-based devices.

Later work compared the performances of a MoO_3/Al/MoO_3 electrode on glass and on polyethersulfone.[168] Although the same evaporated OLED architecture (NPB/Alq3) as in Yuns work was used, the maximum luminance values are 4 times higher. However, external quantum efficiency values are 30 % lower. This may derive from worse sheet resistance and worse transmittance caused by non-optimized layer thicknesses and Al as metal in the DMD, which lead to higher electrical and optical losses.

In order to improve the MoO_3/Al/MoO_3 electrode, Xu et al. presented a MoO_3/Ca:Ag/MoO_3 electrode.[169] The use of Ag instead of Al enhances the conductivity and the transmittance by itself, but additional adding a thin Ca interlayer between MoO_3 and Ag enhances the Ag film morphology even more. It features a sheet resistance of 27.1 Ω/sq and a transmittance close to 80 % at 550 nm. The evaporated OLED features a 2.7 times higher power efficacy than the ITO reference.

Up to this point, the presented OLED heterostructures from the literature on DMD TEs were fabricated using evaporated organic light emitters, transport layers, (doped) ZnO, MoO_3 and ZnS as dielectrics and Ag or Al as metals.[170]

However, sputtered DMD layers would be a further development, because sputtering features a lot of benefits: lower process vacuum, higher adhesion, higher homogeneity and stochiometric independent target material composition are few to mention.[112] Therefore sputtered DMDs are preferential over

evaporated DMDs. Additional to sputtered DMD layers, solution processed injection and emitting layers are of special interest since the trend in industry marches steadily towards solution processing. An approach with a sputtered AZO/Ag/AZO architecture was published by Gentle et al. in 2016.[171] As hole injection, layer a 10 nm thick evaporated MoO_3 layer was evaporated on the AZO/Ag/AZO films. The emitting layer consisted of the spin coated polyphenylene vinylene copolymer PDY-132 "super yellow" (from Merck, Germany) layer. The layer stacks were tested on glass and compared to ITO. A 50 % higher external quantum efficiency compared to the ITO reference was achieved. One can see that sputtered DMD electrodes with solution processed active layers were successfully implemented in OLEDs in the past.

Before any OLED manufacturing could start, first experiments to test the electrode stability during solution processing were conducted. The following section explains why the approach for a regular architecture OLED failed and gives details on the design and transmittance parameters of the final electrode for the chosen inverted architecture OLED.

4.2.1 Optical properties of TiO_x/Ag/AZO electrodes with electron injection layer

The most promising TAA electrode presented in section 4.1.3 features AZO as a top layer. This features some drawbacks for solution-based device processing because AZO is highly prone to acidity. As explained in section 2.3.2, the most widely used hole injection layer in regular architecture OLEDs is PEDOT:PSS. It features a pH value of 1.5 – 2.5 which causes etching of AZO. Although pH neutral versions of PEDOT:PSS exist, first tests of spin coating different pH neutral solutions on the TAA electrode showed partial removal of the electrode material.

Therefore, it was decided to use a mixture of ZnO nanoparticles and Polyetherimide (PEI) (ZnONP:PEI) as electron injection layer on the AZO layer and create an inverted architecture OLED.[111] The ZnONP:PEI solution was dissolved in IPA. This solution did not attack the sputtered AZO layer. As shown in section 4.1.3, the optimized layer thickness of AZO to achieve maximum transmittance is 51 nm. The used ZnONP:PEI solution yields a layer thickness of 30 nm. To compensate for this 30 nm thick layer, TAA electrodes with AZO layers of 21 and 10 nm thickness were sputtered for comparison in device performance.

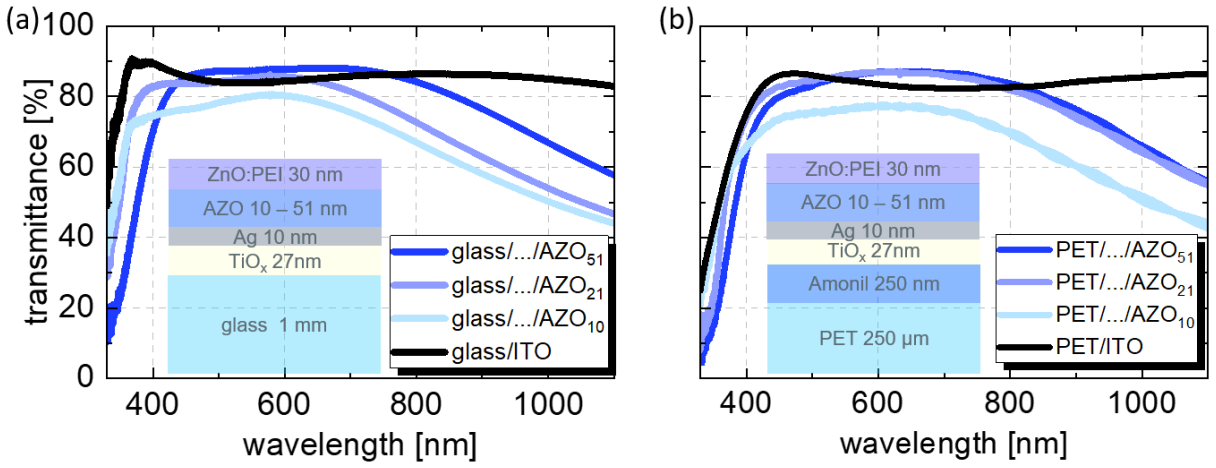

Figure 4.2-1: Transmittance of the used electrode stacks with varying AZO thickness and on ITO on glass (a) and PET (b), the insets show the corresponding schematics of the electrode with the electron injection layer applied, not to scale. Due to the reduction of AZO thickness to compensate for the ZnONP:PEI layer thickness similar transmittance values as in section 4.1.3 are achieved. Submitted at *Adv. Eng. Mat.* and modified.

Figure 4.2-1 shows the transmittance of the TAA electrodes with different AZO thicknesses on glass and modified PET in comparison to ITO, the insets show the different layer sequences of the electrodes (not to scale). All transmittances spectra were measured with the ZnONP:PEI layer spin coated on the different electrode types. Figure 4.2-1 (a) shows the transmittance of the electrodes on glass. The transmittance in the visible wavelength of the DMD with d_{AZO} = 51 nm (dark blue line) is higher than the transmittance of ITO (black line), comparable to the transmittance spectra in section 4.1.2. With the reduction of d_{AZO} to 21 nm (blue line), transmittance losses occur. Still, the transmittance is in the range of ITO. Further reduction d_{AZO} to 10 nm (light blue) leads to further transmittance losses. All DMD samples show a R_{sh} value < 6 Ω/sq, while glass/ITO features R_{sh} values of 15 Ω/sq.

Figure 4.2-1 (b) shows the transmittance values of the same TAA electrodes with varying AZO thicknesses on modified PET in comparison to PET/ITO. The DMD electrode with the optimized AZO thickness of 51 nm shows the same transmittance spectra as in section 4.1.3, although the ZnONP:PEI layer is applied on the electrode. Lowering d_{AZO} to 21 nm does not change the transmittance behavior. Lowest AZO thickness shows again the lowest transmittance as on glass (Figure 4.2-1 (a)). The DMD electrodes on modified PET show the same low sheet resistances as on glass, while PET/ITO features R_{sh} values of 60 Ω/sq. Sheet resistance is independent of AZO thickness and substrate due to the constant 10 nm thick silver layer.

The transmittance key values are summed up in Table 3. Besides the average transmittance in the optical wavelength range (400 to 700 nm), the average transmittance of the emission relevant spectral part for super yellow from 500 to 700 nm ($T_{500\text{-}700}$) and the transmittance at 550 nm (T_{550}) is given.

The relevant transmittance values of the TAA electrode with the ZnONP:PEI layer are higher or equal to ITO/ZnONP:PEI on glass and on PET, except for the TAA electrodes with AZO_{10}.

Table 3: Transmittance key factors of TEs for OLEDs on glass and modified PET

	glass			PET		
thin film	T_{av} **[%]**	$T_{500\text{-}700}$ **[%]**	T_{550} **[%]**	T_{av} **[%]**	$T_{500\text{-}700}$ **[%]**	T_{550} **[%]**
AZO_{51}	86.24	87.67	87.39	83.56	86.29	85.78
AZO_{21}	84.23	84.58	85.37	84.81	86.35	86.22
AZO_{10}	78.15	79.03	80.09	75.28	76.65	76.63
ITO	85.08	84.57	83.97	83.90	83.70	84.60

Since a proper electron injection layer for the TAA electrodes was found to realize an inverted OLED, devices were manufactured on the TAA and ITO electrodes to compare the electrode performance in the OLEDs.

4.2.2 OLEDs implementing TiO_x/Ag/AZO electrodes on glass

It was decided to start with devices on the TAA electrodes on glass, to eliminate any possible errors which may derive from the use of PET as substrate. Figure 4.2-2 shows the current-density-voltage- and luminance characteristics (JVL) of the devices based on glass/TAA electrodes with different AZO thicknesses and on glass/ITO. In Figure 4.2-2 (a) one can see that the OLEDs on TAA electrodes show similar electrical characteristics as the ITO reference electrode from -3 to 4.5 V. The low dark currents of the AZO_{21} and AZO_{51} device is in the same range as the ITO device.

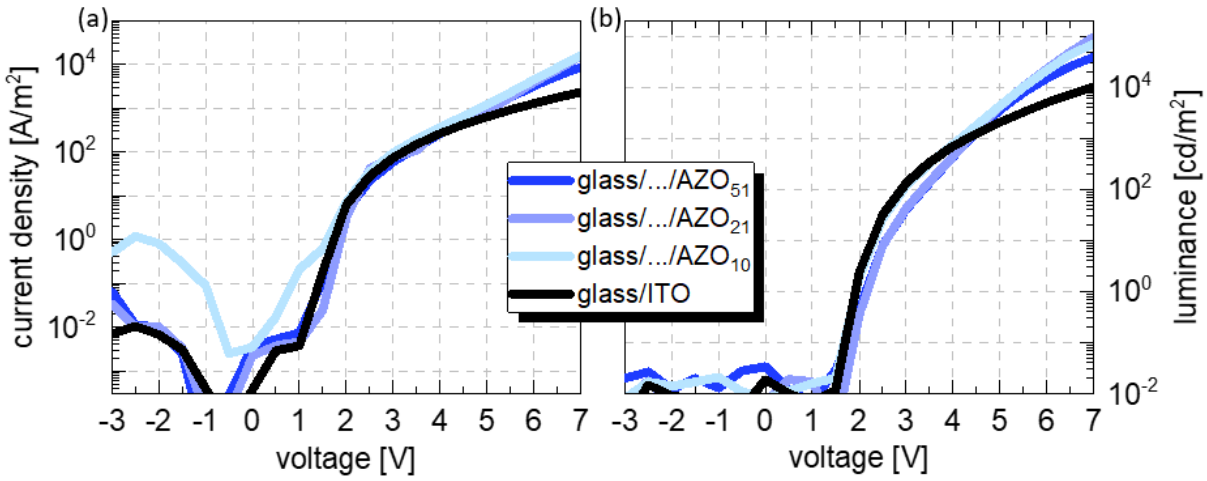

Figure 4.2-2: JV-characteristics of OLEDs on tested DMD electrode with varying AZO thickness and on ITO on glass (a), DMD based devices show higher currents than the ITO based device. Luminance-voltage characteristics of OLEDs on tested DMDs with varying AZO thickness and on ITO on glass (b), showing higher luminance values for the DMD based devices. Submitted at *Adv. Eng. Mat.* and modified.

At 4.5 V, the DMD electrode-based OLEDs start to show higher currents than the ITO reference OLEDs, which derives from the 3 times lower R_{sh}. The luminance characteristics of the devices (Figure 4.2-2 (b)) show that the higher electrical current results in higher luminance values, also starting at approximately 4.5 V.

Luminance record is achieved for d_{AZO} = 21 nm with almost 100000 cd/m^2. Highest luminance with an AZO thickness of 51 nm is 56000 cd/m^2 and for an AZO thickness of 10 nm 70000 cd/m^2. The OLEDs on the ITO reference electrode achieves a considerably lower maximum luminance of 49000 cd/m^2.

The 3 times higher R_{sh} value of the ITO based devices lead to a faster ohmic heating of the electrode, which cause thermal failure of the emitting layer at lower luminance values compared to the TAA based devices.[111] After realizing outstanding OLEDs on glass, the process was directly tested on PET as will be shown in the next section.

4.2.3 OLEDs implementing TiO_x/Ag/AZO electrodes on PET

The promising results of OLEDs built on the TAA electrodes on glass led to further experiments on PET, to follow the scope of the thesis in finding a flexible transparent electrode. As shown in section 4.1.3, the developed TAA electrode on modified PET features similar roughness and R_{sh} values as on glass. The transmittance of the TAA electrode on modified PET with the added electron injection layer is also in the same range as on glass. Since essential parameters for TE are similar on glass and modified PET, similar device performance is to be expected.

The JV characteristics of the OLEDs on TAA on modified PET (Figure 4.2-3 (a)) show a similar picture to the ones on glass (Figure 4.2-2 (a)). In comparison to the ITO device on PET, the current density of the devices on TAA is immediately higher, caused by the in this case 12 times lower R_{sh} of the TAA based devices. The luminance values (Figure 4.2-3 (b)) in combination with the JV characteristics (Figure 4.2-3 (a)) of the PET samples show a similar picture as on glass. The higher current densities at lower voltage levels are transferred to higher luminance output, as well as the TAA device luminance values diverge to higher values from the ITO device values around 4.5 V.

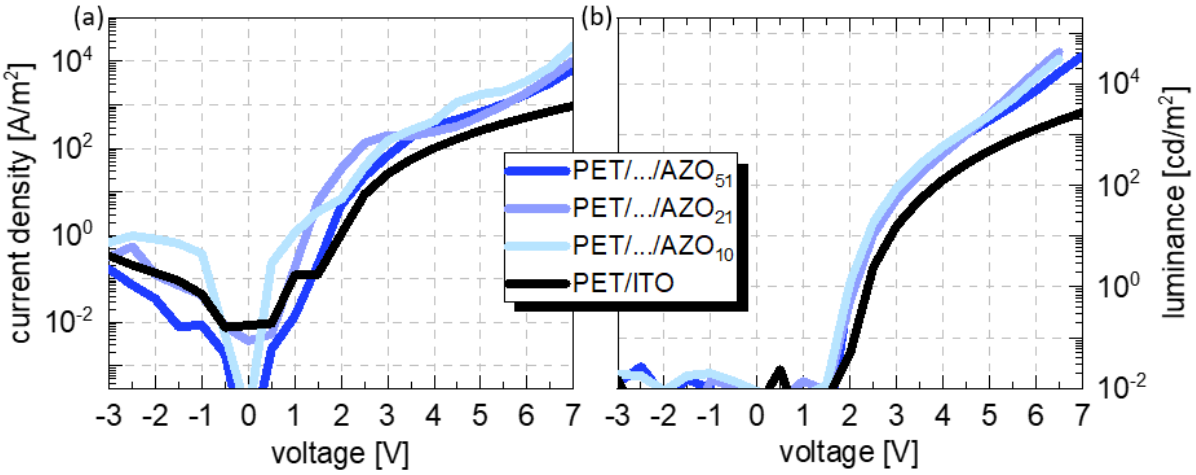

Figure 4.2-3: JV-characteristics of OLEDs on tested DMD electrode with varying AZO thickness and on ITO on modified PET (a), DMD based devices show higher currents than the ITO based device. Luminance-voltage characteristics of OLEDs on tested DMDs with varying AZO thickness and on ITO on modified PET (b), showing higher luminance values for the DMD based devices. Submitted at *Adv. Eng. Mat.* and modified.

Albeit, the JV and luminance characteristics are like on glass, the maximum luminance values on PET are lower. The device with AZO_{51} shows a luminance of 43000 cd/m^2, the same as the OLED on AZO_{21} with a maximum luminance of 43000 cd/m^2. AZO_{10} shows the lowest luminance with 31000 cd/m^2. Still all TAA sample devices display higher luminance values than ITO which shows a maximum luminance of 18000 cd/m^2. The difference in maximum luminance between glass and PET samples, independent of electrode type (TAA or ITO) and basically with the same RMS roughness as shown earlier, is caused by residual individual spikes on the PET which lead to a higher device failure rate at higher voltages and hence lower absolute luminance values.[172]

4.2.4 Comparison of OLEDs on TiO_x/Ag/AZO electrodes on glass and PET

The TAA electrode presented in section 4.1.3 proofed high performance in the presented OLEDs on glass and on PET. It was shown that the current density of ITO based reference devices have a less steep increase than compared to TAA devices independent of substrate material. This leads to the conclusion that the TAA electrodes do not lose as much current by ohmic resistance than ITO, caused by the lower R_{sh} of the TAA electrodes.

It was further shown that in the case of the TAA electrodes it is possible to convert the higher currents to higher luminance values, caused by a better charge carrier injection balance and light outcoupling of the TAA based devices. Higher possible currents combined with lower ohmic losses, higher light outcoupling and balanced charge carrier injection lead to highly efficient devices as shown in Figure 4.2-4. In Figure 4.2-4, the current efficacies are plotted versus the luminance values of the OLEDs on different TAA electrodes as well as ITO on glass (a) and on PET (b). On glass (Figure 4.2-4 (a)), the TAA based devices show different current efficacy behavior, depending on the AZO thickness.

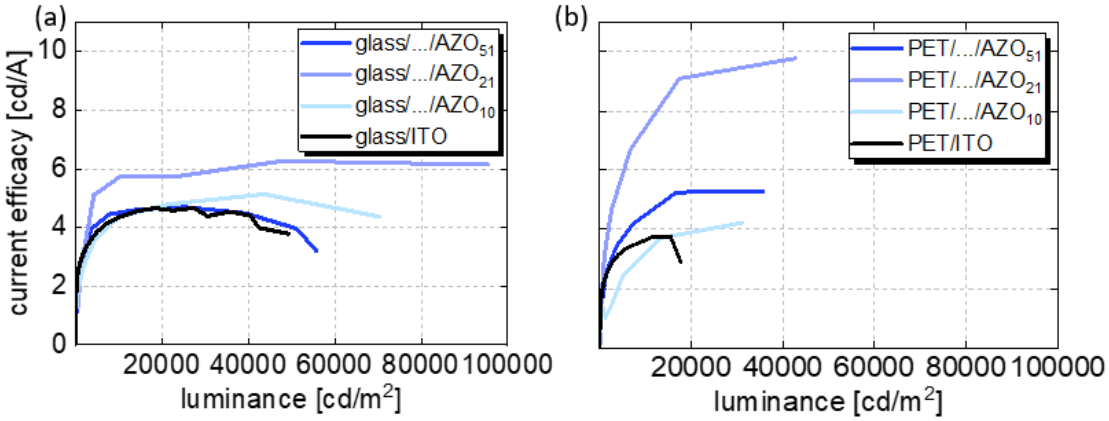

Figure 4.2-4: Current efficacy of tested OLEDs on DMDs with varying AZO thickness and on ITO on glass (a) and PET (b). Showing highest efficacies for the AZO_{21} samples which indicates the best charge carrier injection balance for this thickness. Submitted at *Adv. Eng. Mat.* and modified.

Outstanding performance is achieved for the device with d_{AZO} = 21 nm. This electrode features a current efficacy at 10000 cd/m² of 5.74 cd/A, while the ITO reference device has an efficacy of 4.36 cd/A. In contrast to the ITO device, the AZO_{21} device shows increasing efficacy from that luminance value, up to almost 100000 cd/m² with a maximum efficacy of 6.27 cd/A at 50000 cd/m². At 99910 cd/m² it shows 6.14 cd/A, which is only slightly less although twice as bright.

On PET (Figure 4.2-4 (b)), the device with d_{AZO} = 21 nm also shows the highest current efficacy, which equals 9.78 cd/A. At 10000 cd/m², the device with AZO_{21} on PET shows slightly higher current efficacy of 7.60 cd/A compared to glass (5.74 cd/A). The devices with AZO_{51} show efficacies higher than on glass, 5.48 cd/A. The AZO_{10} device shows a maximum current efficacy of 4.22 cd/A which is below its

counterpart on glass. Still, AZO_{51} and AZO_{21} show higher efficacies than ITO (max. eff. 3.75 cd/A) on PET.

Figure 4.2-5 compares the power efficacies of the same devices as in Figure 4.2-5. Power efficacy takes the voltage necessary to achieve a certain current into account. Power efficacy (lm/W) of the devices was determined by calculating the electrical power consumed by the OLED ($P = IU$) and calculating lm from cd according to Forrest et al. by assuming a Lambertian light source: $1\ lm = \pi\ (1\ cd)$.[173] On glass (Figure 4.2-5 (a)), the same efficacy behavior as in in Figure 4.2-5 (a) is visible. Devices with TAA electrodes outperform the ITO references. In this case, the sheet resistance difference between TAA and ITO based devices leads to a more pronounced separation than in the current efficacy case. The device with the AZO_{21} electrode outperforms all the other two TAA devices. This indicates an optimum charge carrier injection balance for the AZO_{21} device over the AZO_{51} and AZO_{10} devices.

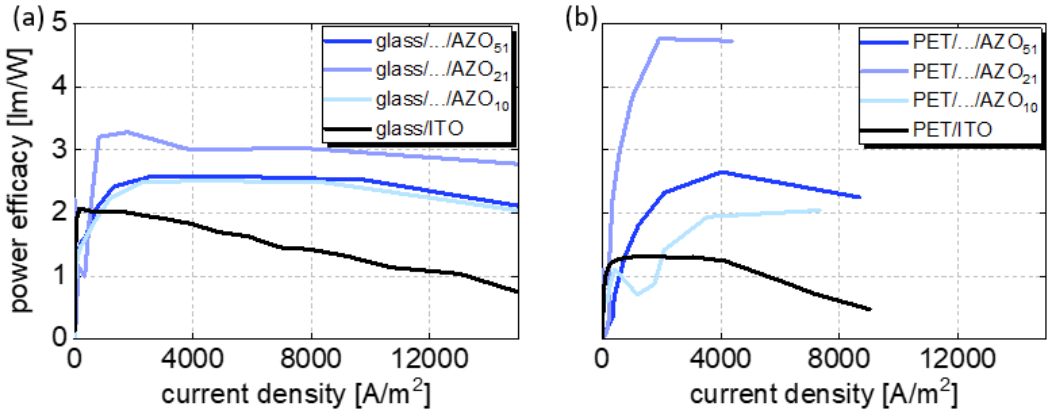

Figure 4.2-5: Power efficacy of tested OLEDs on DMDs with varying AZO thickness and on ITO on glass (a) and PET (b). Showing highest efficacies for the AZO_{21} samples which indicates the highest charge carrier injection balance for this thickness. Higher power efficacies for DMD electrodes in general are achieved due to the lower R_{sh} which is taken into account in power efficacies. Submitted at *Adv. Eng. Mat.* and modified.

On PET (Figure 4.2-5 (b)), the sheet resistance difference between TAA and ITO based OLEDs is also visible. The ITO based device shows a lower efficacy than on glass, resulting from the 4 times higher sheet resistance. The TAA based devices show similar efficacies as on glass for the AZO_{10} and AZO_{51} case. As on glass, the AZO_{21} device outperforms all other devices, again indicating an optimized layer thickness for AZO to get an optimized charge carrier injection balance.

Table 4 gives the key performance values of the OLEDs on glass and PET with varying AZO thickness and the ITO reference. One can identify that devices with AZO_{21} outperform in terms of luminance and efficacy on glass and modified PET, indicating the best charge carrier injection balance and the highest light outcoupling independent of substrate. Devices with AZO_{10} have a lower light outcoupling and a less ideal charge carrier injection balance. The OLEDs with AZO_{51} may have the highest light outcoupling, but the layer too thick to optimally balance the charge carrier injection as the numbers in Table 4 imply.

Table 4:Comparison of Key features of DMD electrodes with varying AZO thickness and ITO on glass and PET:

	glass				PET			
	V_{on} @ 10 cd/m^2 [V]	max. lum. [cd/m^2]	max. eff. [cd/A]	eff. @ 10000 cd/m^2 [cd/A]	V_{on} @ 10 cd/m^2 [V]	max. lum. [cd/m^2]	max. eff. [cd/A]	eff. @ 10000 cd/m^2 [cd/A]
AZO$_{51}$	2.30	75729	5.23	4.52	2.56	43410	5.48	4.54
AZO$_{21}$	2.58	99910	6.27	5.74	2.48	42629	9.78	7.60
AZO$_{10}$	2.32	70294	5.14	4.36	2.38	31025	4.22	3.37
ITO	2.28	49314	4.67	4.36	2.88	17650	3.75	3.64

In Figure 4.2-6, the electroluminescence spectra of the OLEDs on the TAA- and on the ITO electrode on glass are shown. The typical emission peak for Super Yellow at 560 nm can be identified for both electrode types. Due to the higher transmittance of the TAA electrode, a higher relative luminance is visible from approximately 600-700 nm. The CIE coordinates are: x = 0.4665; y = 0.5155 for the NW device and: x = 0.4624; y = 0.5238 and for the ITO device.

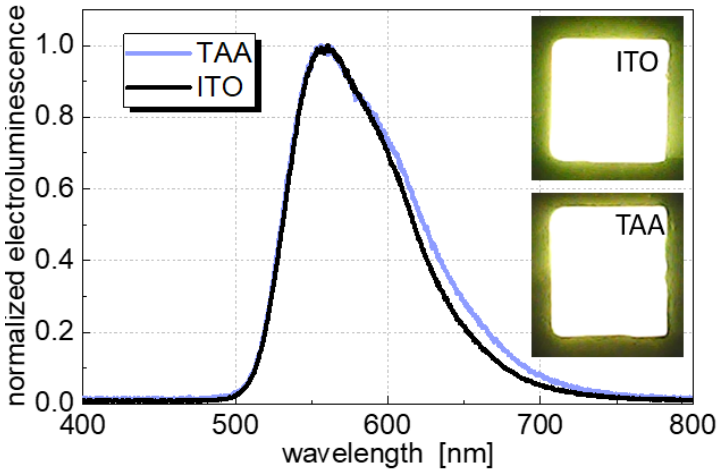

Figure 4.2-6: Electroluminescence spectra of OLEDs on the TAA electrode and on ITO on glass, showing the color independence of electrode type.

4.3 Summary on DMD electrodes

To reach the scope of developing flexible transparent electrodes, DMD electrodes were identified as a promising candidate to achieve this goal. A variety of different DMD electrodes were simulated and investigated for transmittance and conductivity performance. In the simulations, silver was chosen as metal and kept at constant thickness of 10 nm. With the constant metal film, the simulation yielded optimized thickness parameters for the chosen dielectric variations.

First, different combinations of (un)doped ZnO were used as dielectrics sandwiching the Ag film. In general, all DMD electrodes showed a similar sheet resistance on glass and PET due to the constant silver layer. In terms of transmittance, it was observed that doping ZnO with Al increases average transmittance, hence AZO/Ag/AZO proved to have a higher average transmittance than ZnO/Ag/ZnO electrodes. In both cases, the average transmittance on glass was higher than on PET. The difference resulted from the higher roughness of the electrodes on PET, caused by the higher initial PET roughness.

The most promising simulated DMD electrode on glass, a TiO_x/Ag/AZO stack, showed poor performance on PET due to the initial PET roughness. To overcome this issue, the effect of inorganic/organic composite interlayers on sputtered TiO_x/Ag/AZO electrodes on PET was presented. Average transmittance of the electrode on bare PET is very low (44.8 %) and the sheet resistance is high (30 Ω/sq), which is in sharp contrast with its performance on glass, where we find a T_{av} of 88.1 % and a sheet resistance of 5.7 Ω/sq. With the use of a UV-crosslinked organic-inorganic composite layer (Amonil®) between the PET and TiO_x, the electrodes yield an average transmittance of 85 % and sheet resistance of 5.7 Ω/sq. The electrodes also present a low root-mean-square roughness of 1.7 nm. The improved electrode performance could be explained by the growth modification of TiO_x on the interlayer, making it similar to TiO_x growth on glass. The presented TAA electrodes showed that their superior transmittance, conductivity and flexibility outperform the industrial ITO standard.

To proof the concept of the TAA electrodes, the implementation in OLED devices on glass and PET was studied. On glass, a 34 % higher current efficacy of the tested TAA electrodes compared to ITO was achieved, while on PET a 260 % higher current efficacy was achieved. The device on the TAA electrode on glass did furthermore achieve an outstandingly high luminance of almost 100000 cd/m^2.

It can be concluded that DMD electrodes proofed to be a promising candidate for an ITO alternative in terms of optical and electrical performance. Moreover, the presented electrode offers ITO free material compositions and no need for substrate heating during sputtering to achieve high performances.

5 Silver nanowire based transparent electrodes

"Size matters not…" – Master Yoda

As stated in the introduction, this thesis presents two approaches to develop flexible transparent electrodes. The approach with sputtered DMD electrodes was presented in chapter 4. This chapter presents the approach with silver nanowire thin films.

Silver nanowire thin films offer the possibility for solution processing, which would be preferential over sputter coating in terms of process cost. Challenges in silver nanowire thin film fabrication are their need for post deposition treatments, which can damage the substrate and their high roughness as explained in section 2.2.2.

In this thesis, plasma curing was chosen as a fast and effective post deposition curing method. On glass, first experiments showed good results. However, the process could not be transferred to PET because the nanowires are heated up inductively by the oscillating electric field during the plasma process and melt the heat sensitive substrate.

Since nanowire film roughness is also an issue, it was decided to use an embedding and transferring process to flatten the electrode and work around the heat sensitive substrate. It was found that plasma curing could be done on heat stable Polyimide (Kapton®) and the NW film could later be transferred to PET while simultaneously flattening the surface.

This process came at the cost of losing NWs on the Kapton® surface due to the plasma treatment. The process needed to be adapted by simply reversing the process order of curing and embedding. By exchanging the embedding and curing process, a thermal stability enhancement of PET by the embedding material was achieved. The enhanced thermal stability offers the possibility to inductively weld the NW on PET during the plasma process.

In the following sections, a detailed literature research on embedding and curing NW films and an in-depth analysis of NW films processed with the different process orders on glass, Kapton® and PET is given. NW electrodes are implemented in solution processed OLEDs to proof the concept in device manufacturing. The devices perform similar to ITO based reference devices in terms of power efficiency. Regarding the luminance, devices on the NW electrode outperform the ITO reference devices. It will further be shown that the NW electrodes on PET offer a far higher mechanical flexibility than the ITO reference.

5.1 Embedding and transferring of silver nanowire thin films

Part of the content of this chapter is based on work that has been published and was partly modified: Kinner, L. *et al.*: Gentle plasma process for embedded silver-nanowire flexible transparent electrodes on temperature-sensitive polymer substrates. *Nanotechnology* **31**, (2020).

To work around heat sensitive PET substrates in NW thin film manufacturing, different transferring techniques have been presented in the literature. The idea is to do the thermal processing of the NWs on a thermally stable host substrate before the NWs are transferred to the final substrate.

Xie et al. developed a process where NWs are deposited on mixed cellulose ester (MCE) substrates via vacuum filtration.[174] The NWs were dried for 30 minutes at 80°C before the MCE/NW was mounted to the PET substrate and further processed in acetone vapor. Afterwards, the MCE was dissolved in acetone to obtain the PET/NW electrode. This yielded an electrode with 73 % transmittance at 550 nm (including the substrate) with an R_{sh} of 130 Ω/sq.

Instead of vacuum filtration, wire bar coating was used in a float transfer process. Al-coated PET was used as substrate and the NWs treated for 1 hour in a plasma. The Al-coating was then etched for over 8 h in NaOH and the floating film was then transferred to the final substrate. The free-standing NW films yielded 91 % transmittance and 13 Ω/sq. It is further mentioned that these NWs had a mean diameter of about 120 nm and a length of 20–70 µm.[175]

A similar approach was shown using anodized aluminum oxide (AAO) membranes and vacuum filtration to coat the membranes with NWs. The membranes withstand the heat treatment at 200 °C for 20 minutes, after which the NW films were transferred via a polydimethylsiloxane (PDMS) mold to a PET substrate.[176,177] The process yielded electrodes with 10 Ω/sq and 85 % transmittance (excluding the substrate).

Technological further developed techniques include not only a transfer process but also embedding of NWs to smoothen the surface roughness and increase adhesion. Nam et al. reported such a technique in 2014.[178] A glass substrate was coated with NWs and cured for 5 minutes at 100°C. After that, the UV-curable Polymer NOA63 (from Norland Products) was spin-coated over the NWs. The NWs/NOA63 layer was then peeled off the substrate. This yielded an embedded NW electrode with 82 % transmittance (including the substrate), an RMS roughness of 0.4 nm and a R_{sh} of 16 Ω/sq. In this case the used wires featured a large aspect ratio (average diameter of 35 nm and an average length of 25µm).

Li et al. also used this transfer technique in 2017, using a silicon waver as host substrate.[56] The NWs were spin-coated and cured in an Ar plasma for 15 minutes. After this procedure, the conductive NW

films were coated with NOA63 and peeled off the wafer. A transparency of 78.6 % (including the substrate), an RMS roughness of 1.58 nm and a sheet resistance of 7.2 Ω/sq was obtained.

Alternatively to NOA63, polyurethane (PU) was used in a peel off process from a PET host substrate instead of a silicon wafer.[179] The NWs were treated on PET with heat, NaCl and HCl. This yielded an electrode with PU as substrate with 85 % transmittance (including the substrate), an RMS roughness of 6.7 nm and 15 Ω/sq. However, the PU curing needs 40 minutes, which hampers fast processing.

The described peel-off processes show the potential of reverse embedding and transferring of silver nanowire films to work around sensitive substrates and smoothen the roughness. In the described processes, the embedding material works directly as new substrate material. An extension to the aforementioned processes would be the embedding of the NWs in a material while adding a new substrate material on top of the embedding material. This would offer a more stable TE, as the embedding material would have for example a piece of PET foil underneath it. With this kind of process, which includes embedding and transferring to a new substrate, R2R production would be easier.

The most relevant process for embedding NWs and transferring them to a new substrate was reported by Jung et al..[180] Thermally stable polyimide was used as initial substrate for the NW deposition, followed by infrared (IR) flash light curing of the NWs. Afterwards, the NWs were simultaneously embedded in NOA63 and transferred to a PET substrate, similar to the works from Nam and Li. The roughness was 2.3 nm while the transmittance was 74.7 % (including the substrate) and the R_{sh} 8.3 Ω/sq. High aspect ratio NWs were used with 27 µm length and 32 nm diameter.

The embedding process used in this thesis was first described by Burgeos et al. for embedding inkjet printed silver grids.[181] The initial process order - in this case for sprayed NWs instead of inkjet printed grids - is shown in Figure 5.1-1 (old). In step I, the host substrate (HS) is spray coated with NWs. In step II the wires are plasma cured on the HS which results in the need of a thermal stable substrate - in this case glass or PI. Step III shows the drop coating of the cured NWs with Ormocomp® and then the final substrate (FS) - coated with OrmoPrime 08® - is placed on the HS.

Ormocomp® is a UV curable hybrid polymer. Hybrid polymers are polymers with added inorganic elements, for example silicon. UV curable polymers are polymers which change their chemical structure or cross link with neighboring molecules under UV radiation. After UV radiation, the films show glass like but still mechanical flexible properties. Ormocomp® belongs to the material class of Ormocers®, which were developed by the Fraunhofer Institut für Silicatforschung and manufactured and distributed by micro resist technology GmbH.[182] Additionally to OrmoComp®, its adhesion promoter OrmoPrime 08® was used (from micro resist technology GmbH).

The stack of HS/NW/Ormocomp®/OrmoPrime 08®/FS is cured under UV light for 10 seconds. In the end, a mechanical lift-off is performed, transferring the embedded NWs from the HS to the FS, with

the NWs being now on the top of the FS. This process is shown for the case of HS=glass and FS= glass (G2G), as well as for the HS=Kapton® and the FS=PET (K2P).

To further develop the initial process by getting rid of the thermal sensitive HS, a new process order was introduced (Figure 5.1-1 (new)). NWs are sprayed directly on PET (or glass as reference). From there, they are firstly embedded and then transferred to the final PET foil before being cured in the plasma. In this case, it is shown that the polymer matrix acts as a thermal buffer to enable the plasma curing of the NWs without damaging the PET substrate. Both variants lead to high performance electrodes with differences in the roughness and optical haze. It is also shown that the same electrode performance can be obtained as the one achieved for embedded NW electrodes using glass as host and final substrate.

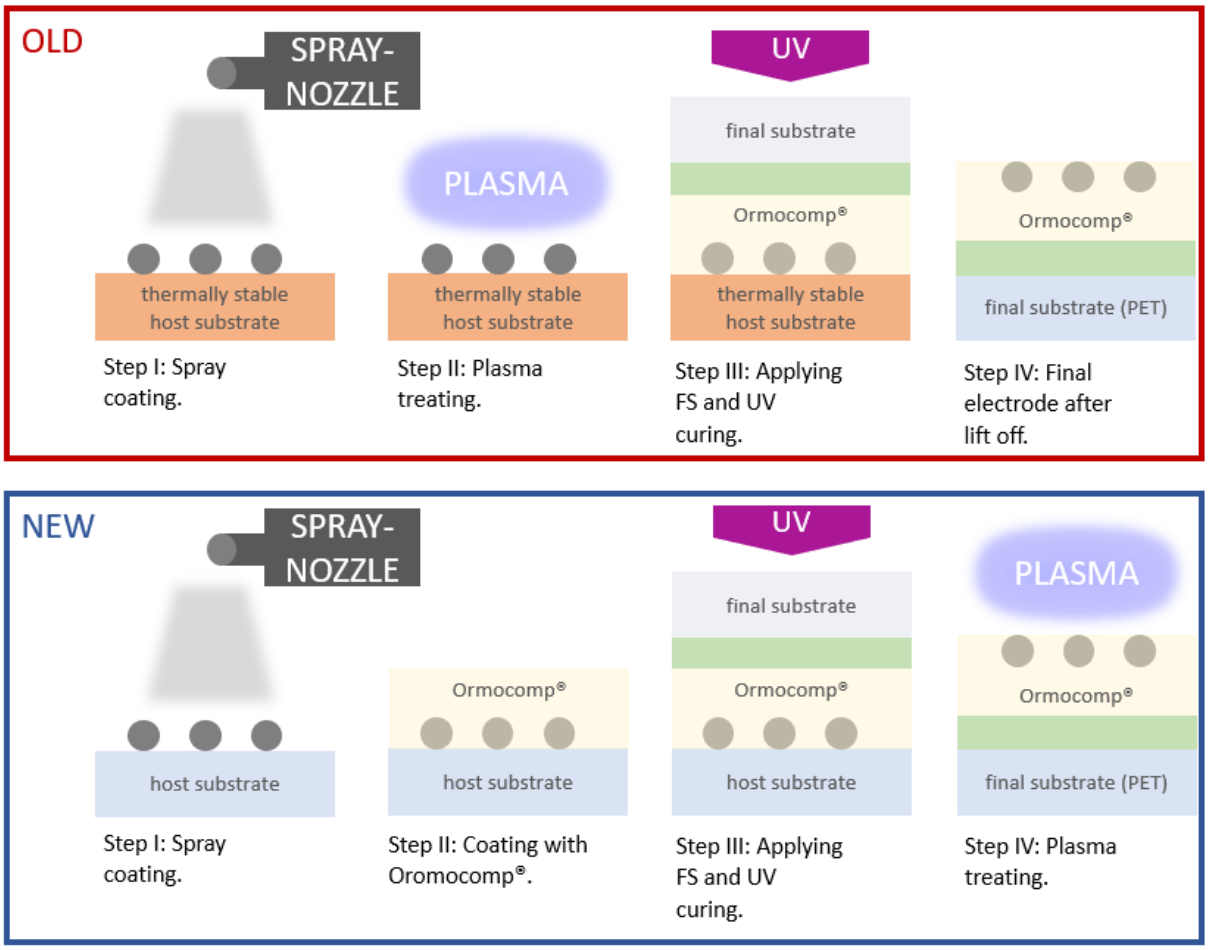

Figure 5.1-1: Schematic representation of initial (old) and developed (new) process, showing the necessary exchange of process steps for the use of PET as host substrate (new). Taken from [52] and modified.

5.1.1 Morphology of NW electrodes on glass and PET

First experiments to study NW film formation during spraying and the influence on NWs by plasma treatment were carried out on glass to avoid unwanted interactions with heat sensitive PET. Figure 5.1-2 and Figure 5.1-3 show SEM images of the NW films obtained at different process stages, using glass as HS and as FS. This is denoted as glass-to-glass, or "G2G" process. In the standard process, the NWs are sprayed (Figure 5.1-2 (a) and Figure 5.1-3 (a)) and then plasma-cured (Figure 5.1-2 (b) and Figure 5.1-3 (b)) on the HS. Then, the NWs are embedded and transferred to the FS (Figure 5.1-2 (c) and Figure 5.1-3 (c)). In the standard process, the curing step does not seem to lead to significant morphological changes apart from the location of the NW junctures, where a close contact is formed. A significant drop of the sheet resistance from 200 kΩ/sq for the as-sprayed films to 13 Ω/sq is observed after curing. The sheet resistance remains unchanged after the transfer process.

The long-term goal of this study was to find a way to process NW thin films on PET only. The idea was born to inverse the process so that heat sensitive PET could be reinforced with Ormocomp® to withstand the plasma treatment. To verify if the NWs can be welded within the Orcmocmp® and if inversing the process would cause any other issues, first inverse process tests were carried out on glass.

In the inverse process - after the spraying of the NWs on the HS (Figure 5.1-2 (d) and Figure 5.1-3 (d)) and after their embedding - the transfer on the FS takes place (Figure 5.1-2 (e) and Figure 5.1-3 (e)), followed by the plasma curing (Figure 5.1-2 (f) and Figure 5.1-3 (f)). One can see that in any case the sprayed NWs form a homogeneous film which is not influenced by the curing or embedding process.

Both the standard and inverse process give rise to the same sheet resistance for the final embedded NW electrode. The effect of curing the NWs after being embedded and transferred on the FS are visible in Figure 5.1-2 (f) and Figure 5.1-3 (f). The arrows mark holes in the Ormcomp® film due to etching in the O_2 containing plasma.[183] The induced porosity in the Ormocomp® layer increases the RMS roughness but does not influence the optical transmittance, as will be shown later.

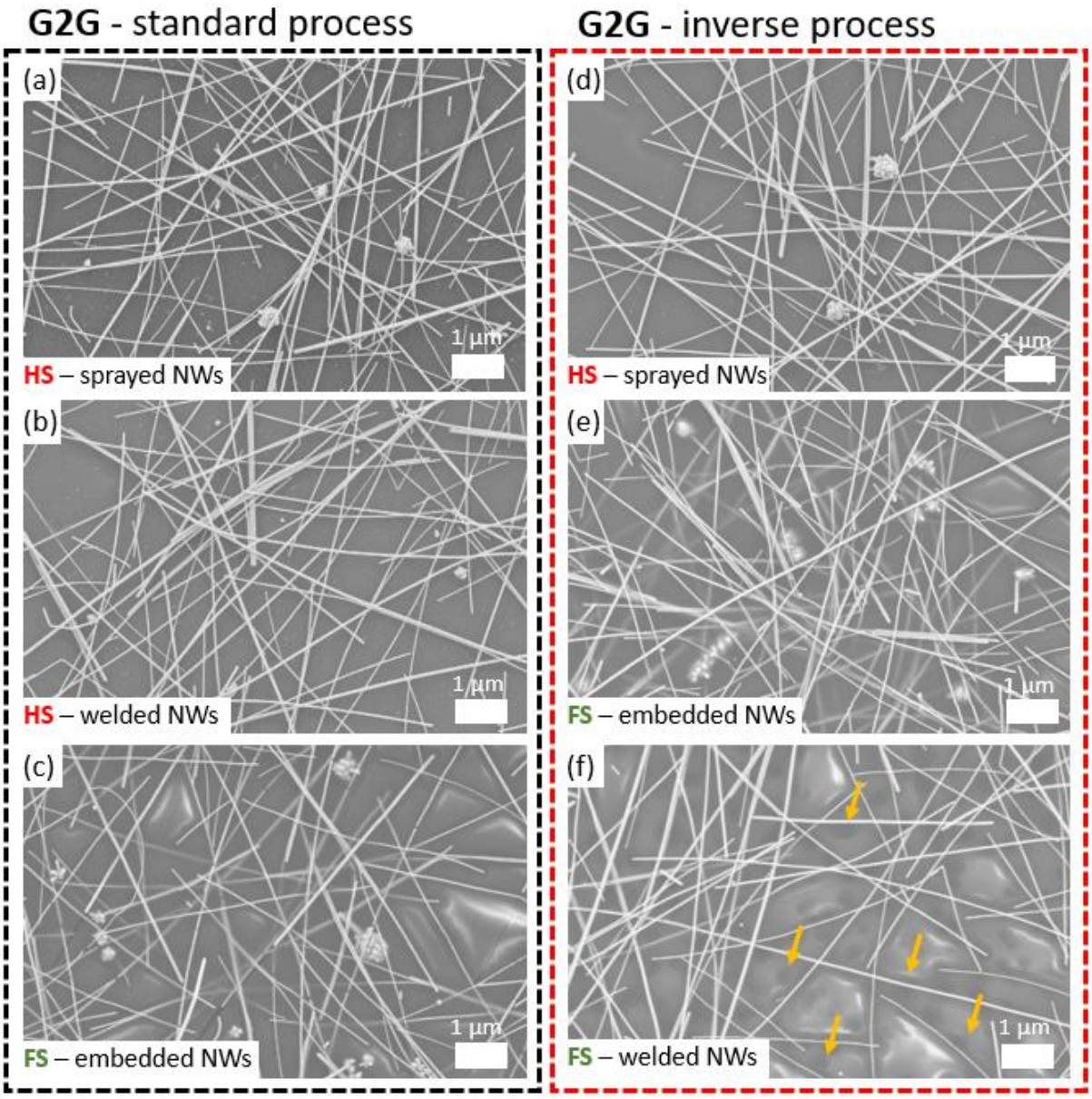

Figure 5.1-2: SEM images of the electrode surface at different process stages on glass as-sprayed Ag-NWs on the HS (a); welded NWs on the HS (b); embedded and welded NWs on the FS (c); as sprayed NWs on the HS (d); embedded NWs on and the FS (e); welded and embedded (f). Due to spray deposition a homogenous NW distribution is achieved in both processes, small holes occur in the Ormocomp ® due to the plasma treatment (yellow arrows). Taken from [121] and modified.

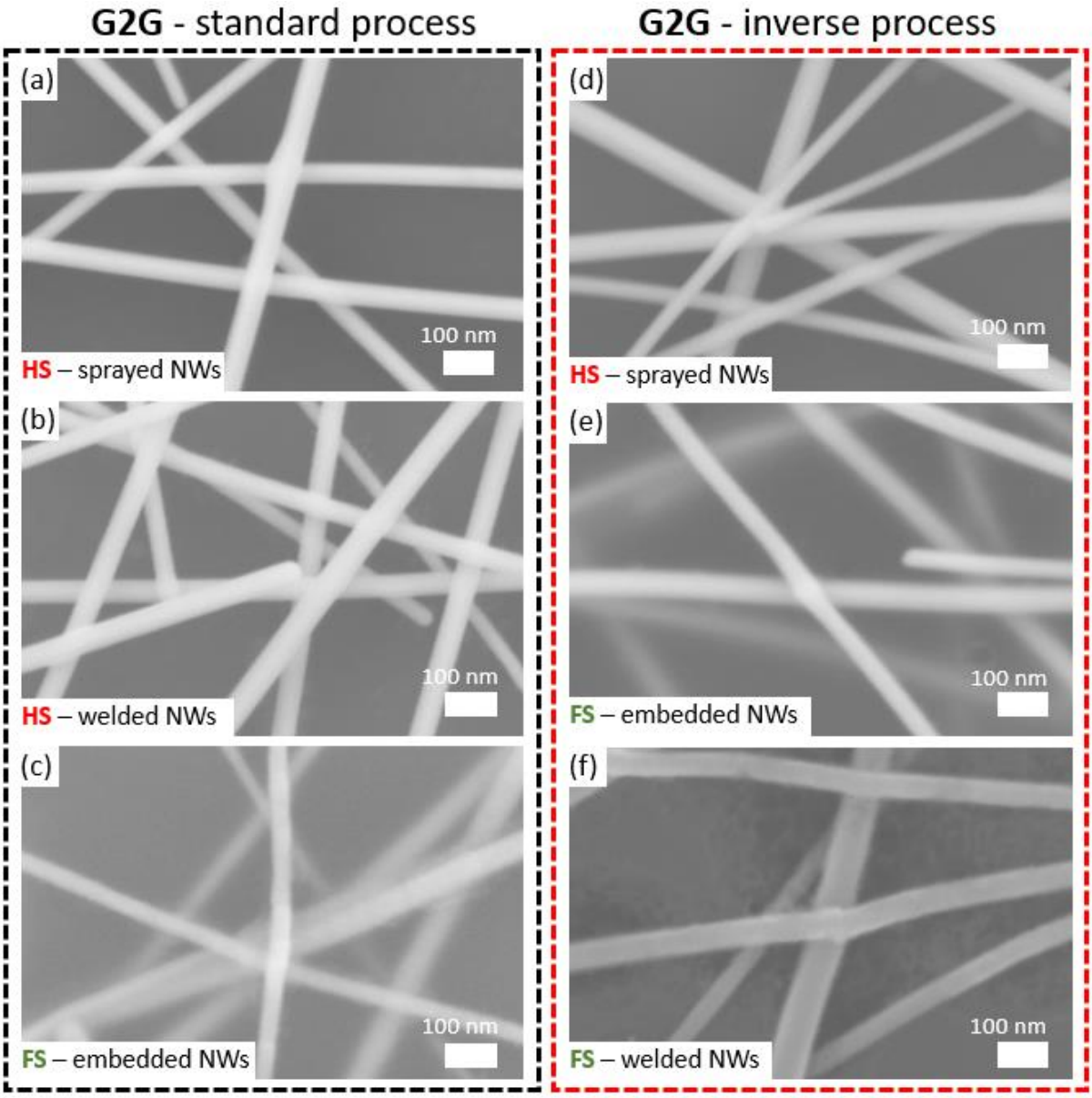

Figure 5.1-3: SEM images of the electrode surface at different process stages on glass as-sprayed Ag-NWs on the HS (a); welded NWs on the HS (b); embedded and welded NWs on the FS (c); as sprayed NWs on the HS (d); embedded NWs on the FS (e); welded and embedded (f). The close up of the previous image shows that the nanowires are in physical contact in both process versions and hence form a conducting micromesh.

To quantify the topographic properties of the previously shown SEM images, SFM measurements were performed. Figure 5.1-4 (a) and (b) show the embedded NW electrode fabricated with the standard and inverse process on glass. The RMS roughness is significantly larger for the inverse processed sample, namely 28 nm compared to 5 nm for the standard process. The difference is caused by the occurrence of holes in the Ormocomp® due to the plasma treatment.

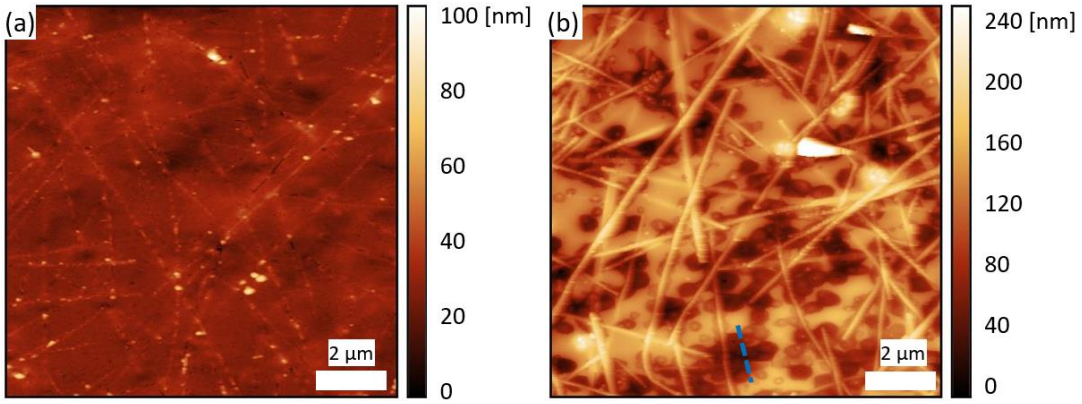

Figure 5.1-4: SFM images of the embedded NW electrodes. G2G in standard process (a), showing a low roughness due to embedding and the slightly elevated NWs. G2G in inverse process (b) showing holes in the Ormocomp® due to the plasma curing and relatively elevated NWs due to vanishing of Ormocomp® in the plasma. Taken from [121] and modified.

It was observed that the standard process is not applicable when PET is used as HS (denoted as PET-to-PET or "P2P" process). Plasma curing of the NWs on PET leads to the damaging of the PET substrate due to the excessive thermal budget transferred to it. To control if the plasma itself is destroying the PET substrate, the following experiment was conducted: bare PET samples were put in the plasma oven and the same parameters as for NW curing were applied. Without NWs on top of the PET substrate, the PET did not show any damage. It can be concluded that the NWs are cured by the induced current, from the electric field, which leads to ohmic heating in the NWs and not by the heat from the plasma itself.

To work around the heat sensitive PET substrate polyimide (Kapton®) was used as HS in first experiments, like in the work from Jung et al..[180] Kapton® is a widely-used, temperature stable polymer film. The Kapton®-to-PET process is denoted as "K2P". It was anticipated that the standard process could be used for NW transferring from the polyimide to the PET substrate. Figure 5.1-5 (d), Figure 5.1-6 (d), Figure 5.1-5 (e) and Figure 5.1-6 (e) show the sprayed NWs on the polyimide substrate before and after curing, respectively. For the curing of the NWs on polyimide, the curing time had to be decreased compared to what was used for glass. After 3 min curing time, the wire junctions showed pronounced welding points while the wires were roughened and deformed. Broken and/or melted pieces of wires were also observed. Moreover, a good embedding and transfer process was inhibited as the wires adhered strongly to the polyimide substrate. For these reasons, the curing time was

reduced to 1 min. There, the wires showed no damage. The measured sheet resistance after 1 min curing time was 12 Ω/sq.

The differences in the observed curing effects on glass and polyimide are attributed to two reasons. First, they are attributed to different thermal conductivities which are 0.96 and 0.12 W/(m*K) for glass and PI, respectively.[184,185] Due to the lower thermal conductivity of polyimide, heat cannot be easily evacuated giving rise to more pronounced NW welding which leads to NW damage.

Second, the roughness of PI is higher than the roughness of glass, making the contact area (A) between the NW and the substrate smaller, according to the 1D Fourier's law: $\frac{Q}{\Delta t} = -kA\frac{\Delta T}{\Delta x}$. With the smaller contact area *A*, the heat *Q* transferred from the NWs to the substrate per time Δt decreases, making the NW curing more pronounced. ΔT stands for the temperature difference, k stands for the Boltzmann constant.

Since it was observed that the NWs were cured inductively and not by the direct contact with the plasma, the inverse process was tested for a P2P process. It was anticipated that the embedding Ormocomp® layer would work as thermal buffer layer and reinforce the PET substrate.

For the P2P process, the inverse process order needs to be applied: after spraying the NWs (Figure 5.1-5 (a) and Figure 5.1-6 (a)), where a homogenous film is obtained, the NWs are transferred onto the FS (Figure 5.1-5 (b) and Figure 5.1-6 (b)) and then plasma-cured (Figure 5.1-5 (c) and Figure 5.1-6 (c)). The thermal budget due to the plasma curing can be evacuated to the Ormocomp® layer, invoking no damage to the PET substrate. The sheet resistance decreases from >200 kΩ/sq for the as-sprayed films on PET to 13 Ω/sq for the embedded NWs on PET after curing, i.e. the same value as the resistance achieved on glass.

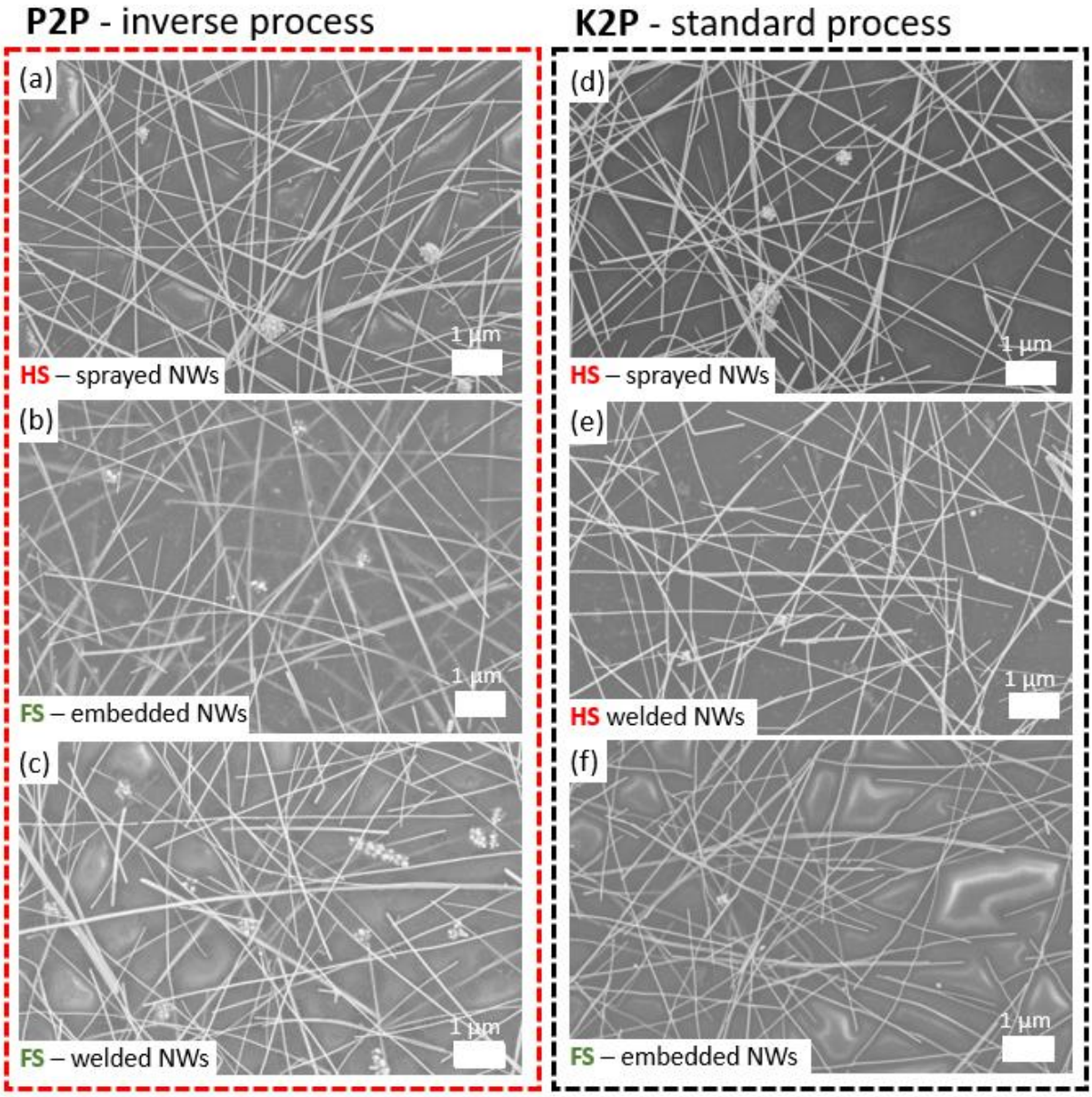

Figure 5.1-5: SEM images of the electrode surface at different process stages on flexible substrates as-sprayed NWs on the HS (PET) (a); embedded NWs on the FS (PET) (b); embedded and welded NWs on the FS (PET) (c); as sprayed NWs on Kapton® (d); welded NWs on Kapton® (e); cured and welded NWs on PET (f). Due to optimized process parameters the same morphology and wire to wire junctions are achieved. Taken from [121] and modified.

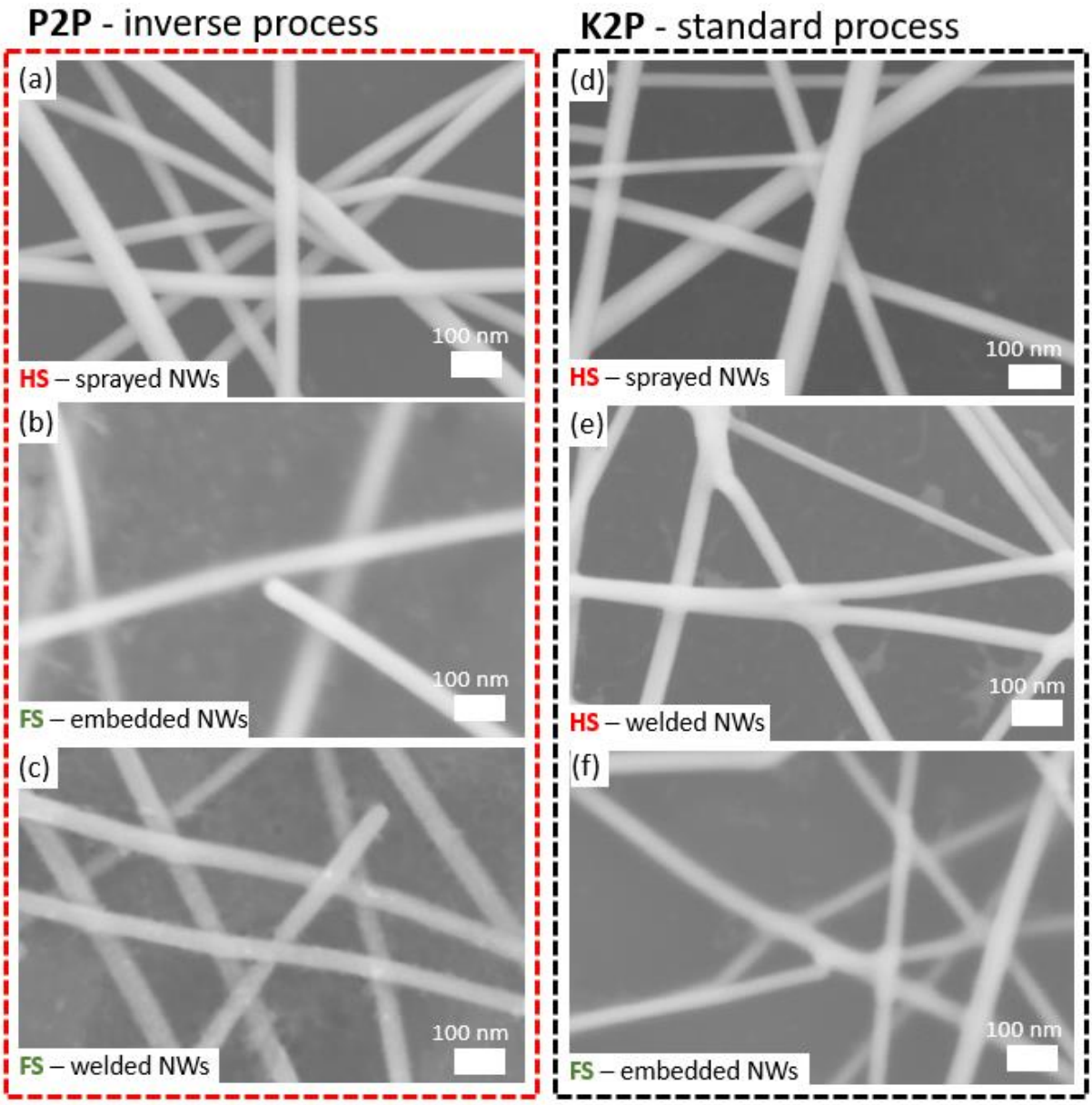

Figure 5.1-6: SEM images of the electrode surface at different process stages on flexible substrates as-sprayed NWs on the HS (PET) (a); embedded NWs on the FS (PET) (b); embedded and welded NWs on PET (c); as sprayed NWs on the HS Kapton® (d); NWs welded on Kapton® (e); welded and embedded NWs on PET (f). Due to a lower thermal budget slightly pronounced welding points occurred between the NWs on Kapton® (e-f); besides that the same close contact between the NWs as on glass is achieved and hence the same macroscopic properties.

To quantify the topography of the electrodes created by K2P and P2P processes SFM images were taken of the samples. For the P2P inverse process (Figure 5.1-7 (a)), the occurrence of holes as shown on glass gives a RMS roughness of 25 nm. The SFM image for the K2P standard process displays no holes (Figure 5.1-7 (b)) as shown for G2G SP but a RMS roughness of 18 nm. The roughness of the electrodes mainly reflects the background roughness of the host substrate. Initial roughness of glass is 1.0 nm, of Kapton® 13.7 nm and of PET 8.0 nm.

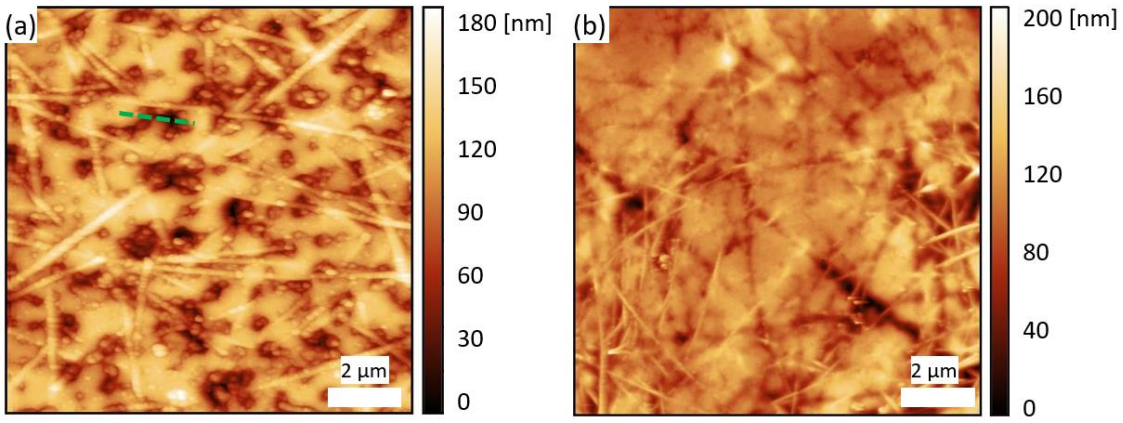

Figure 5.1-7: SFM images of: P2P in inverse process (a), due to the inverse processing the same holes and morphology as on glass for inverse processing is observed. K2P in standard process (b), traces of some lost NWs in the Ormocomp® are visible due to sticking of the NW to Ormocomp® during transfer, some NW still became transferred to the Ormocomp® on PET. Taken from [121] and modified.

Profile data were taken from IP G2G and P2P (Figure 5.1-7 (a) and Figure 5.1-7 (b)) to determine the depth of the holes. The profiles are displayed in Figure 5.1-8 . The approximate depth of the holes is 120 nm. As displayed in Table 5, these holes influence the average haze of the electrode but not the total transmittance.

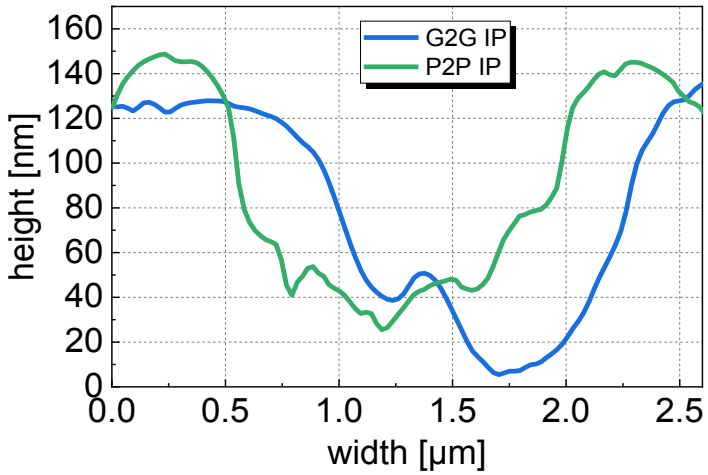

Figure 5.1-8: Surface profile lines taken from G2G and P2P IP samples showing the depth of the holes in the Ormocomp® caused by the plasma treatment. Taken from [121] and modified.

5.1.2 Current mapping

Ormocomp® is an electrical isolating polymer. Therefore, it is necessary to quantify the lateral conductivity distribution of the surface of the NW electrodes. Contact-mode conducting SFM measurements deliver conductivity measurements with the spatial resolution of a SFM.

Figure 5.1-10 visualizes the topographic SFM image (Figure 5.1-10 (a)) together with the current map image (Figure 5.1-10 (b)), acquired simultaneously. A bias voltage of 1 V was applied to the tip. The saturation current from the amplifier was 10 nA. Most of the NWs appearing in the topographic image led to saturated current flow in the current-map image. Indicating that the NWs protrude out of the Ormcomp® surface to assure an electrical conductive surface.

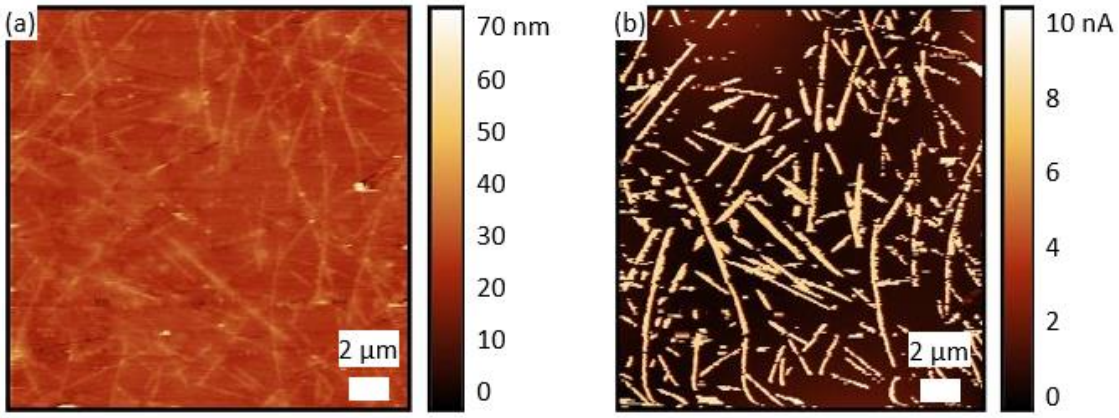

Figure 5.1-9: Large area SFM image of embedded NW on glass (a) and conductive SFM image of the same sample (b) showing the overlap between slightly pronounced NW partly above the surface of the embedding material and conductive areas on the surface. Further, some "background" conductivity (areas up to 4 nA) are visible in (b). Taken from [121] and modified.

The average distance between 2 neighboring wires is less than 1 µm (Figure 5.1-10 (b)). Figure 5.1-10 (a-b) shows morphological and contact conductive SFM images in larger magnification. Corresponding cross section line profiles were extracted from the topographic and current map images (blue lines in Figure 5.1-10 (a) and (b)). In Figure 5.1-10 (c), these profiles are plotted. IT can be seen that the topographic spikes corresponding to the NWs also lead to current spikes where the current is saturated. No current is measured between the wires on the Ormocomp® matrix.

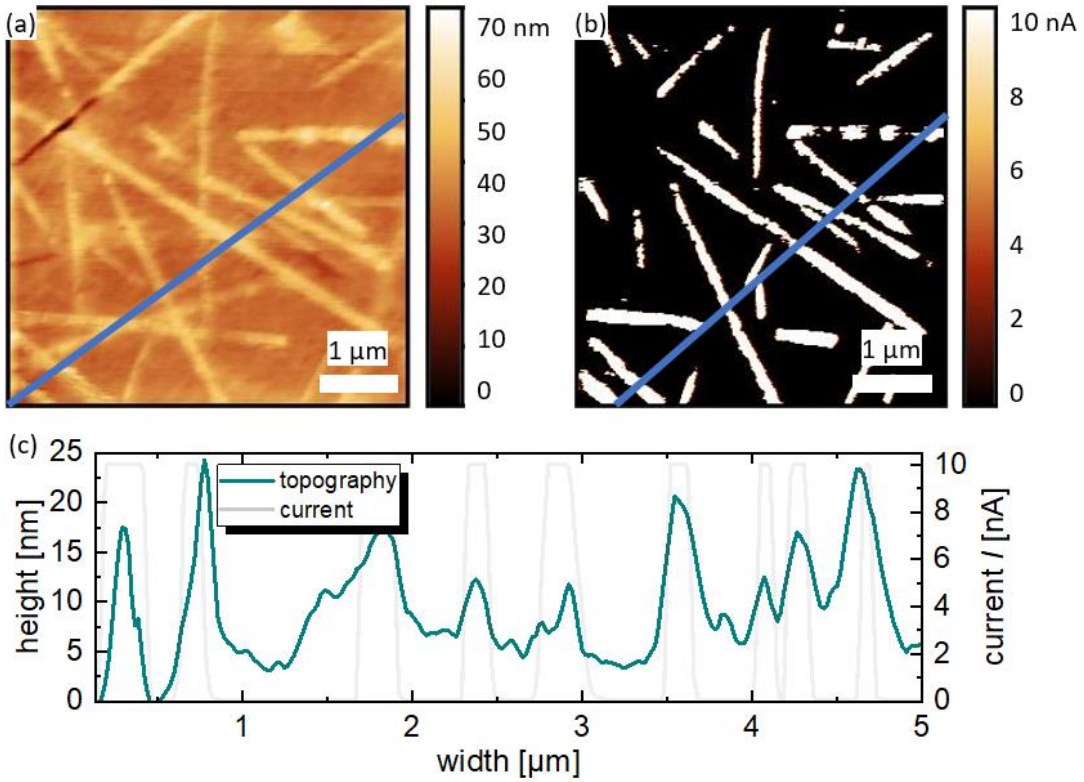

Figure 5.1-10: Simultaneously acquired SFM images of the topography (a) and current map (b), with larger magnification. Extracted topography profile (green) from the line marked in (a) and current profile (grey) from the line in (b), show that current maxima are at height maxima (NW penetrating Ormcomp® surface) (c), still in most places is some "background" conductivity visible.

5.1.3 Optical and mechanical properties

To quantify the transmittance of the NW electrodes depending on the process order as well as on the different HS and FS (glass, PET, Kapton®), transmittance spectra of the different electrodes were obtained. Figure 5.1-11 (a) shows spectra after each step of the G2G standard process. The transmittance spectra of the as-sprayed NW film (black line) and of the plasma-treated NW film (red line) are quite similar. Embedding of the NW film leads to pronounced transmittance decrease at low wavelengths due to Ormocomp® absorption (blue dashed line). In the range from 450-600 nm, the transmittance decreases slightly compared to the cured film (red line), while from 650-1100 nm, the embedded film shows a higher transmittance. The specular transmittance is slightly lower than the total transmittance of the final electrode, indicating that the NWs cause a lot of individual refractions which ad up to haze of the electrodes.

In Figure 5.1-11 (b), the transmittance spectra of the individual steps of the G2G inverse process are shown. The transmittance of the initial film is the same as in Figure 5.1-11 (a) (black line). The orange line represents the transmittance of the embedded (uncured) NW film. At low wavelengths the same transmittance decrease as in Figure 5.1-11 (a) is observable, due to the absorption by the Ormocomp®. The transmittance decrease from 450-600 nm and the increase from 650-1100 nm are also caused by the added Ormocomp® layer (same as in Figure 5.1-11 (a)). In this case, the increased transmittance must derive from the smoother surface which is caused by embedding the NWs. Curing of the embedded NW films lower specular transmittance (blue dashed line) in the visible and infrared. The total transmittance is comparable to the spectrum obtained in Figure 5.1-11 (a). The different relation from specular to total transmittance shows the increased haze of the electrode caused by the holes in the Ormocomp® due to inverse processing.

Figure 5.1-11 (c and d) displays the transmittance spectra of the NW films for the P2P and K2P process steps, respectively. The polyimide substrate lacks transparency, which is evident from the highly absorbing spectrum in Figure 5.1-11 (d) (red line). The total transmittance of the final films both in the P2P and K2P processes are similar to glass, while the specular transmittance is significantly lower for the P2P case than for K2P due to the aforementioned roughening of the polymer in the plasma, causing a higher haze. Still, the total transmittance remains as high as the transmittance of the electrodes on glass.

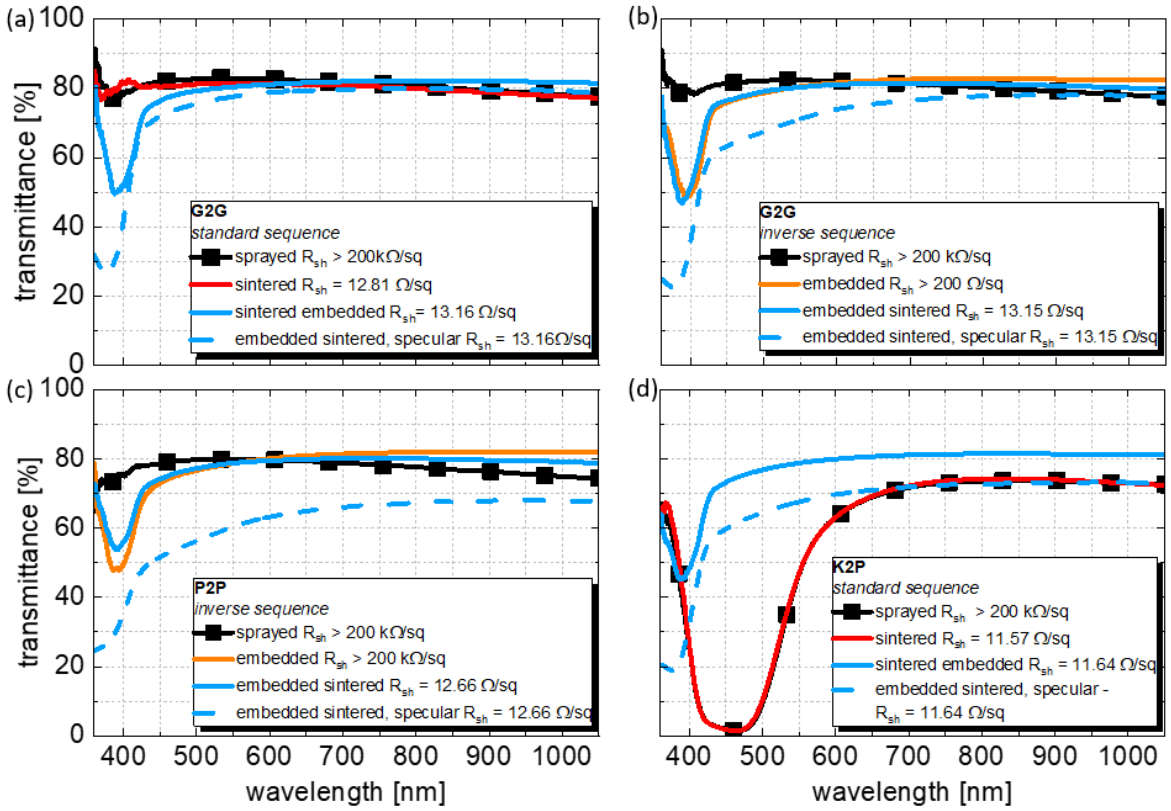

Figure 5.1-11: Transmittance spectra at varying process steps of: G2G standard process (a); G2G inverse process (b); P2P inverse process (c); K2P standard process (d). In any case is the independence of transmittance from process order shown. In cases of invers processes a lower specular transmittance is observable due to holes in the Ormocomp® layer. Taken from [121] and modified.

Key performance values for the electrodes are summarized in Table 5. Haacke's figure-of-merit, $\Phi=(T^{10}/R_{sh})$, for transparent electrodes is also included in the table, using either the average transmittance $T=T_{av}$ (Φ_{av}) or the one at 550 nm $T=T_{550}$ (Φ_{550}).[186]

Table 5: Summary of optical and electrical properties of the presented electrodes on different substrates. The RMS column shows in brackets the RMS of the HS.

sample	T_{av} [%]	T_{550} [%]	H_{av} [%]	R_{sh} [Ω/sq] pre-emb.	R_{sh} [Ω/sq] post-emb.	RMS [nm] 12x12 µm	Φ_{av} [10^{-3}/Ω]	Φ_{550} [10^{-3}/Ω]
glass	81.2	81.5	28.1	12.8	13.2	32.0	9.70	10.14
G2G SP	79.2	80.4	9.2	12.8	13.2	5.1 (1.0)	7.36	8.62
G2G IP	78.3	80.5	11.8	-	13.2	28.3 (1.0)	6.59	8.69
P2P IP	76.8	78.8	24.0	-	12.7	25.3 (8.0)	5.62	7.26
K2P SP	76.4	78.8	14.7	11.6	11.6	18.1 (13.7)	5.78	7.91

As described in the previous chapter, bending tests are necessary to quantify the mechanical stability of the electrodes during mechanical bending.[163,164] The results of the bending experiments are shown in Figure 5.1-12. The same formula for the strain ε during bending ε = *d*/2*r* as in the precious chapter was used.[164–166] In this case, the substrate thickness *d (Ormocomp + PET)* is 480 µm. A nominal strain ε of 6 % was calculated. Compressive bending was carried out additional to tensile bending at the same diameter. The change of *R* was measured in the same way as in the previous chapter. Compared to the commercial ITO on PET (60 Ω/sq), the P2P NW electrode presents much higher stability. After 5000 bending cycles, practically no changes in the sheet resistance of the embedded electrode was observed while the resistance of the ITO electrode increased 28 times after only 70 bending cycles. For the tensile bending tests with 4 mm bending radius, it is shown that the P2P embedded electrode increases its resistance 2.5 times after 5000 bending cycles.

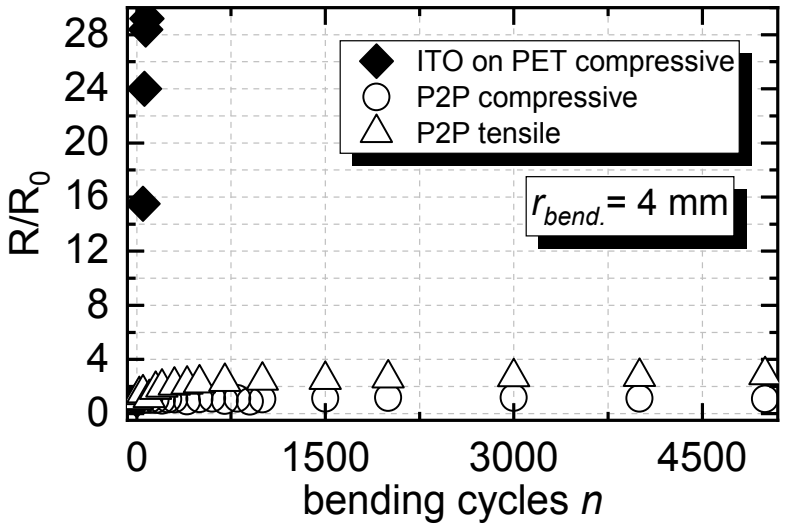

Figure 5.1-12: Relative resistance changes of ITO and embedded NW electrodes on PET under compressive and tensile bending stress with r_{bend} = 4 mm. Showing the far higher durability of NW based electrodes in comparison to ITO based electrodes. Taken from [121] and modified.

5.1.4 Sputter coating embedded nanowire films

So far, the developed NW electrode yielded sufficient morphological, electrical, mechanical and optical properties for a state of the art TE. An extension to the NW electrodes would be the implementation of an additional metal oxide layer like ITO or AZO. Both materials are widely used in OPV and OLED devices in the literature and most production processes rely on those materials as bottom electrodes. The previously shown lack of mechanical flexibility of those oxides could be worked around in a combined electrode.

To investigate a combined electrode of NW and metal oxide 100 nm AZO were sputtered on an embedded NW electrode produced through the P2P approach.

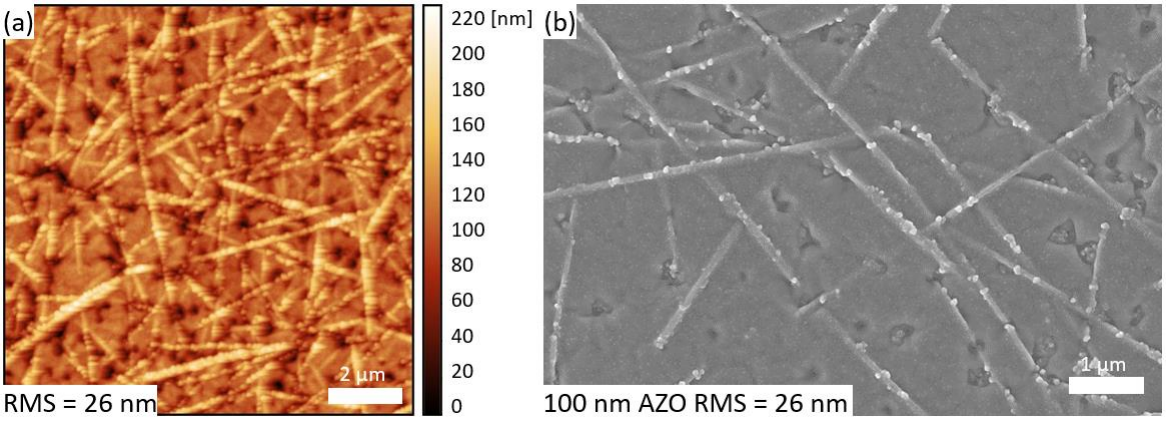

Figure 5.1-13: SFM (a) and SEM (b) images, of the embedded NW electrode, sputter-coated with 100 nm AZO. AZO forms a closed film and slightly fills the holes in the Ormocomp®. Taken from [121] and modified.

A SFM and a SEM image of the coated electrode is shown in Figure 5.1-13 (a) and Figure 5.1-13 (b) respectively. The RMS roughness remains at the same level compared to the uncoated film (26 nm) but the depth of the holes is reduced. The electrode sheet resistance is not changed after the AZO deposition.

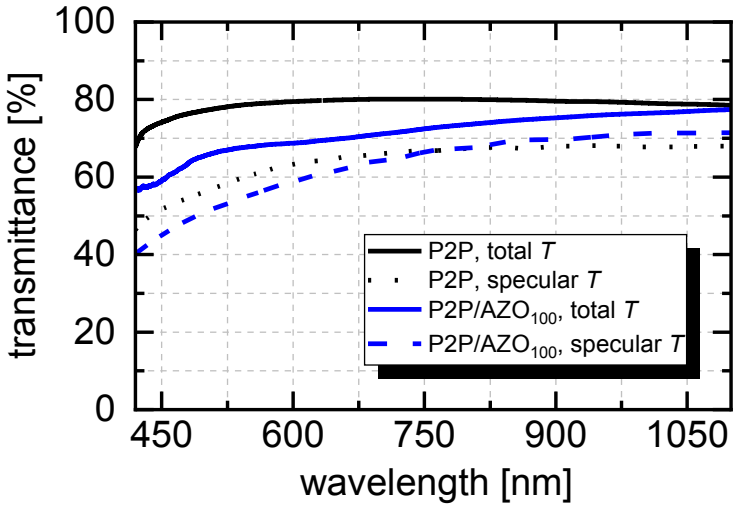

Figure 5.1-14: Transmittance spectra of embedded NW electrodes with and without sputter coated 100 nm AZO P2P IP. Taken from [121] and modified.

Figure 5.1-14 shows the optical property of the coated electrode. The transmittance is lower after the AZO coating (average visible transmittance drops from 76.8 % to 66.2 %). The haze is also decreased after the AZO coating with respect to the uncoated electrode (from 23.95 % to 18.67 %). The decrease of haze is attributed to the partial filling of the holes in the Ormocomp® layer by the sputtered AZO film.

5.2 OLEDs on embedded silver nanowire electrodes

Part of the content of this chapter is based on work that has been published and was partly modified: Kinner, L. *et al.*: Implementation of Flexible Embedded Nanowire Electrodes in Organic Light-Emitting Diodes. *Phys. Status Solidi - Rapid Res. Lett.* **2000305**, 6–11 (2020).

Following the successful transformation of the reverse transfer embedding process to create NW electrodes using only PET as substrate, device tests were done to verify the electrode performance. Embedded NWs have already been implemented in OLEDs in the literature. Lian et al. demonstrated an evaporated OLED architecture on embedded NWs. NWs were spin coated on and then pressed into a polyvinyl alcohol (PVA) film. The PVA film was spin coated on a polyethylene naphthalate substrate.[187] Although the processing is straightforward and does not require vacuum processing, it is unclear if the PVA film resists solution processing as the electrodes have been tested for evaporated OLEDs only.

In the beginning of chapter 5 an approach for a R2R NW embedding process by Jung et al. was mentioned.[180] In this work, not only an embedded NW electrode on PET was presented, but also an evaporated OLED was realized on this electrode. It was shown, that OLED achieved the same luminance but higher external quantum efficiency than a glass/ITO reference.

As stated earlier, the trend in OLED manufacturing goes towards solution processing. Yu et al. presented a solution processed OLED on embedded NWs. NWs are drop cast on a host glass substrate and covered with a UV curable poly(acrylate) which is peeled of the sacrificial glass substrate, containing the NW film. The NWs embedded in the UV-curable protrude from the surface to guarantee surface conductivity and feature a low RMS roughness. On this electrode, a solution processed OLED with the following device architecture was tested: PEDOT:PSS/SuperYellow/CsF/Al. This OLED architecture is the “regular architecture” counterpart to the used “inverted architecture” presented in this thesis. The presented devices feature a similar current efficacy performance to the ITO reference devices but lower electrical currents and lower luminance.[188]

This section presents the realization of solution processed OLEDs on the previously developed NW electrodes. Devices were manufactured on all substrate and process combinations to reveal potential process flaws. First, a short survey if the standard or inverted architecture can be applied on the NW electrodes was carried out. Second, the influence of the charge injection layer on the optical performance was studied.

5.2.1 Optical properties of embedded NW electrodes with electron injection layer

In first tests it was tried to use PEDOT:PSS as hole injection layer, because NWs may feature nonconductive areas in between them as shown in chapter 5.1.2. Due to the acidity of PEDOT:PSS, the NW electrodes lost their conductivity after spin coating PEDOT:PSS. Therefore, it was necessary to find an alternative. It was decided to use the same approach as in section 4.2, namely to use an inverted device architecture an implement the ZnONP:PEI electron injection layer on the NW electrode.
The degradation of the NWs with the use of the pH neutral ZnONP:PEI mixture was inhibited. The light emitting polymer was the solution processed Super Yellow and the anode material evaporated MoO_3/Ag as described in section 4.2.
Comparative experiments between standard and inversely processed electrodes on glass, Kapton® and PET showed, that too many NWs get lost in the standard process (Figure 5.2-1 (a)), which leads to strong luminance inhomogeneities for devices made by the standard process (Figure 5.2-1 (b)).

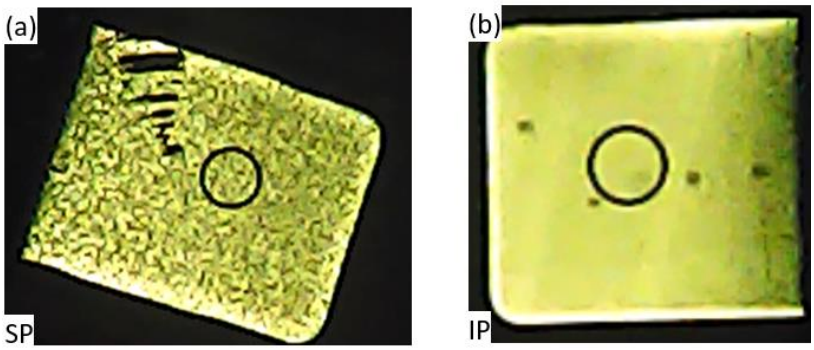

Figure 5.2-1: Images of OLEDs on K2P electrodes (a) showing strong luminance inhomogeneities, due to lost NWs on the HS Kapton® in comparison to the P2P inverse processed electrodes (b).

As shown in section 5.1.1, sticking of the NW to the HS is caused by the plasma treatment prior to embedding (SP). To work around the plasma treatment and to create a less intensive heating and hence less melting and sticking to the HS, the following experiment was carried out: the hot plate temperature during spraying was set to 110 °C. By changing the temperature during spraying, an immediately decreased R_{sh} of the NW films to below 13 Ω/sq was achieved on glass, Kapton® and PET. It could have been concluded that the plasma treatment becomes redundant, but it was observed, that plasma treatment prior to ZnONP:PEI deposition is still necessary to maximize current density and to reduce the risk of shunts in the devices. As a result, it was decided to stick with the IP for G2G and P2P to manufacture electrodes for OLED tests.
In Figure 5.2-2, transmittance spectra of the IP manufactured NW films on glass and PET as well as transmittance spectra of ITO on glass and PET all over coated with the ZnONP:PEI solution, are shown.

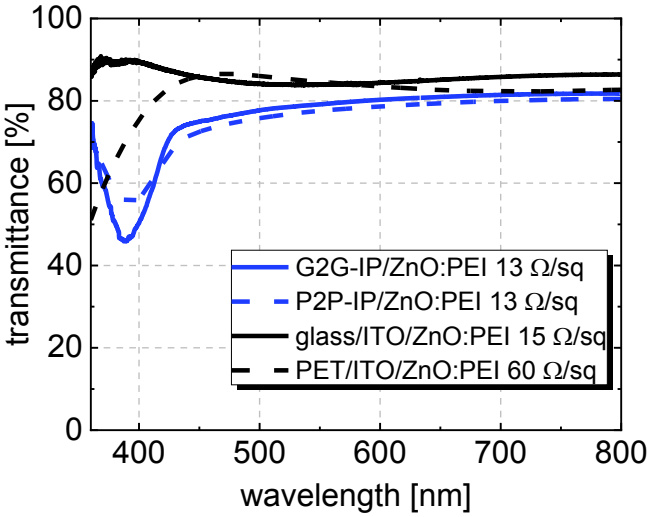

Figure 5.2-2: Transmittance spectra of sprayed NW on PET and glass overcoated with spin coated ZnONP:PEI solution (blue); commercial ITO reference electrode on PET and glass overcoated with spin coated ZnONP:PEI solution (black), showing only slightly lower transmittances for NW electrodes. Taken from [52] and modified.

Overcoating the embedded NWs with the electron injecting ZnONP:PEI mixture does not change the transmittance spectra of the NW electrodes significantly, as compared to the transmittance spectra in section 5.1.3. In comparison to PET/ITO/ZnONP:PEI, the final NW electrode shows lower transmittance in the visible spectral wavelength range. NW electrodes with the ZnONP:PEI overcoating show a R_{sh} of 15 Ω/sq.

Figure 5.2-3 (a-b) presents SEM and SFM images of the embedded NW electrode overcoated with ZnONP:PEI. Top view SEM of the same sample (Figure 5.2-3 (a)) shows the homogeneous distributed NW in the Ormocomp® matrix. Additionally, the ZnONP film is visible by the greyish layer surrounding the NWs. SFM images of the samples show the filling of the holes by the spin coated ZnONP:PEI layer (Figure 5.2-3 (b)). Overcoating the embedded NW with ZnONP:PEI leads to a smoother surface (RMS = 8.1 nm) which is close to the RMS roughness of ITO (5.1 nm).

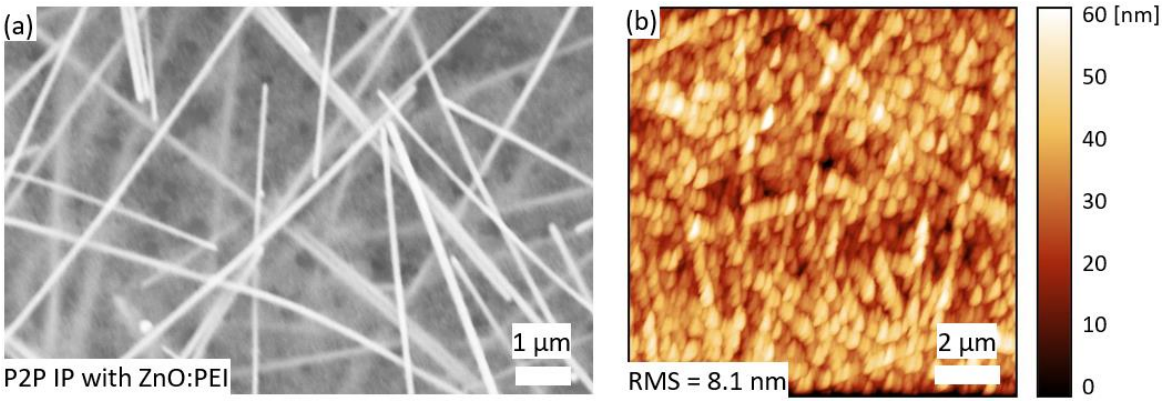

Figure 5.2-3: Top view SEM of embedded NW electrode coated with ZnONP:PEI (a). SFM image of embedded NW electrode overcoated with ZnONP:PEI (b). In both cases a reduction of holes, homogeneous wire distribution and low roughness is observable. Taken from [52] and modified.

5.2.2 OLEDs implementing embedded NW electrodes on glass

In the previous section, the IP was found to be superior over the SP for electrode manufacturing for devices. The ZnONP:PEI layer on the embedded NWs pointed out to be a promising candidate for an electron injection layer to manufacture inverted OLEDs on the embedded NWs.

Initial device experiments were conducted on embedded NWs manufactured by the IP on glass. Glass was chosen as substrate for first tests to eliminate possible errors from using PET. Figure 5.2-4 shows the JVL characteristics of the device manufactured on the G2G IP electrode and on a glass/ITO reference electrode.

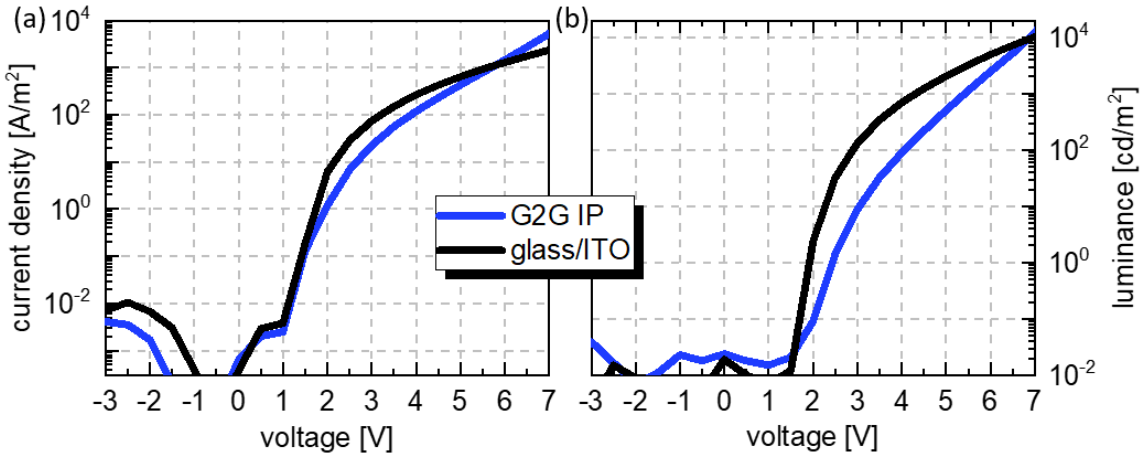

Figure 5.2-4: JV-characteristics of OLEDs on G2G IP processed NW electrodes and on ITO on glass (a), showing slightly lower currents for the NW based devices. Luminance-voltage characteristics of OLEDs on G2G IP processed NW electrodes and on ITO on glass (b), showing lower luminance values for the NW devices in the majority of the voltage range, but not at 7 V.

The JV curve of the embedded NW device Figure 5.2-4 (a) reveals almost the same shunt resistance as the ITO based reference OLED, although the RMS roughness is slightly higher compared to the roughness of the ITO electrode. Figure 5.2-4 (b) compares the luminance output of the NW and the ITO based devices. It is visible that the NW based device shows a higher turn on voltage compared to the ITO device. The luminance values of the NW based device are lower than the ones of the ITO based device up to 6.5 V. Maximum luminance of the NW based device is 12000 cd/m^2 and 10000 cd/m^2 for the ITO based device, both at 7 V.

5.2.3 OLEDs implementing embedded NW electrodes on PET

After the successful implementation of the G2G inverse process NW electrodes in OLEDs, OLED manufacturing was tested on P2P inverse processed NW electrodes. Figure 5.2-5 presents the performance data of OLEDs manufactured on embedded NWs as well as on a PET/ITO reference substrate. In Figure 5.2-5 (a), the corresponding JV characteristics of the devices are shown. In the range from 2 to 4 V, devices on NW electrodes have similar electronic behavior as on the ITO reference. At 4 V, the OLEDs on the NWs show higher currents than the OLEDs on the ITO reference. This behavior results from the 4-5 times lower R_{sh} of the NW electrode compared to the ITO reference electrode.

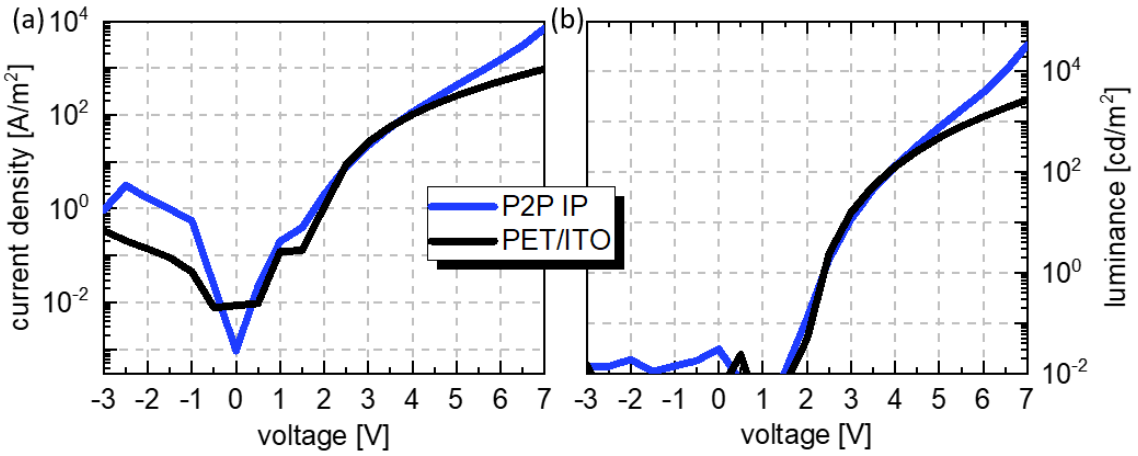

Figure 5.2-5: JV-characteristics of OLEDs on P2P IP processed NW electrodes and on ITO on PET (a) and luminance-voltage characteristics of OLEDs on P2P IP processed NW electrodes and on ITO on PET (b). Devices on NW electrodes achieve the same and higher currents and luminance values as ITO compared to NW and ITO devices on glass. Taken from [52] and modified.

In Figure 5.2-5 (b), the luminance characteristics corresponding to the JV characteristics in Figure 5.2-5 (a) are displayed. A similar turn on voltage between ITO and the NW electrodes is visible. At 4.5 V, luminance values of the NW electrode exceed the ITO reference. It is possible to conclude that the higher luminance starting at 4.5 V is caused by the higher currents starting at 4 V (Figure 5.2-5 (a)). Maximum luminance was achieved for devices on embedded NWs with 34000 cd/m^2. Albeit, the ITO reference device reaches a maximum luminance of 27000 cd/m^2, it reaches it at 11.5 V (not shown), at far higher bias than the NW devices (7 V). As stated earlier, this derives from the in this case 4-5 times lower R_{sh} of the NW electrode compared to the PET/ITO electrode.

5.2.4 Comparison of OLEDs on embedded NWs on glass and PET

So far, the IP NW electrodes showed good performance on glass and PET. For final characterization, the current and power efficacies of the devices were calculated. In Figure 5.2-6, the current efficacy in cd/A is given for the IP NW and ITO based devices on glass and PET. On glass, the ITO based devices show a higher efficacy than the NW based devices (Figure 5.2-6 (a)). Maximum efficacy of the ITO device is 4.36 cd/A and 3.33 cd/A of the embedded NW device. The higher efficacy of the ITO based device is caused by the higher luminance values compared to the NW-based device and not by high dark currents (Figure 5.2-4).

In Figure 5.2-6 (b), the current efficacies of the devices on IP P2P and PET/ITO electrodes are shown. Highest efficacy is achieved by the ITO reference device with 3.7 cd/A from 11000-16000 cd/m^2. Highest efficacy of devices on embedded NW electrodes is achieved with a maximum efficacy of 4.8 cd/A at 34000 cd/m^2. The higher efficacy of ITO-based devices on glass in comparison to ITO-based devices on PET is due to the lower R_{sh} of ITO on glass. According to this fact, ITO-based devices have a faster ohmic heating on PET and because of that, they do not reach such high luminance values. However, NW based devices on PET outperform their counter part on glass.

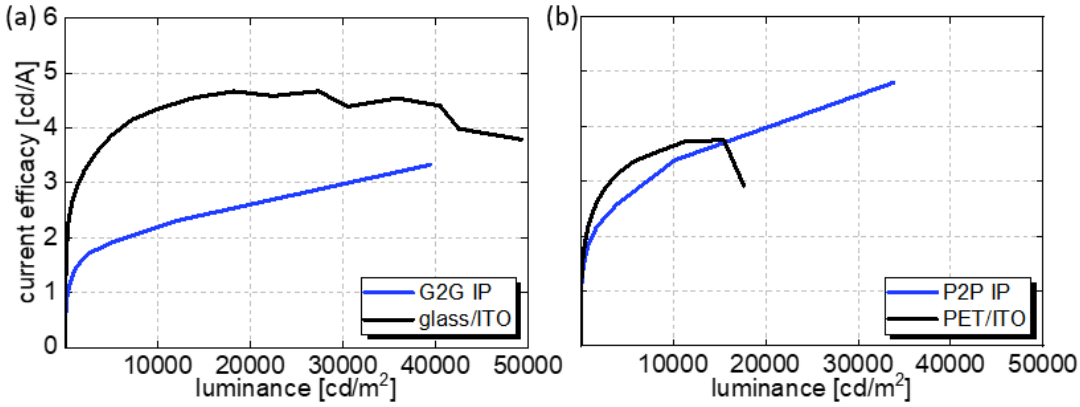

Figure 5.2-6: Comparison of current efficacy of OLEDs on G2G NW and ITO electrodes on glass (a) and PET (b), showing the higher current efficacy of ITO-based devices on glass, but on PET NW-based devices are more efficient than ITO based devices on glass. Taken from [52] and modified.

Additional to the current efficacies power efficacies are shown in Figure 5.2-7, because power efficacies also take the energy consumed by the device to create light into account, not only the current.

Power efficacy in lm/W of the devices was determined by calculating the electrical power consumed by the OLED ($P = IU$) and calculating lm from cd according to Forrest et al. by assuming a Lambertian light source: *1 lm = π (1 cd)*.[173] Figure 5.2-7 (a) displays the power efficacies of the devices on glass. The same behavior as in Figure 5.2-6 is visible. Highest power efficacy is achieved by the ITO reference device with 2.2 lm/W at 265 A/m^2. Highest power efficacy of the devices on embedded NWs on glass is 1.1 lm/W at 8000 A/m^2.

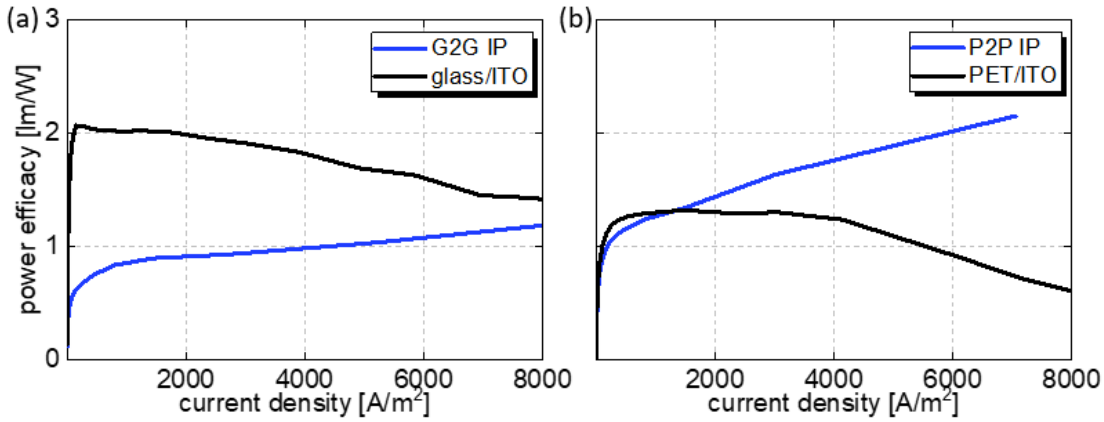

Figure 5.2-7: Power efficacy comparison of OLEDs on inverse processed NW electrodes and ITO electrodes on glass (a) and PET (b). On PET the NW based electrodes show far higher power efficacy than the ITO based devices due to a lower R_{sh}. Taken from [52] and modified.

On PET, the ITO reference device shows a higher power efficacy at lower current densities than devices on embedded NWs (Figure 5.2-7 (b)). This results from the fact that at lower current densities, the ITO-based device has a higher luminance. The highest efficacy of embedded NW devices on PET is 2.2 lm/W, the same as for the ITO device on glass, but at 7000 A/m^2. The efficacy of the NW-based device results from the higher luminance at higher current densities, which can be achieved due to the lower R_{sh} of the NW electrode.

The ITO based devices outperform the NW based devices in terms of efficacy at lower luminance values or current densities on glass and PET. With increasing luminance or current density, respectively the ITO based devices lose efficacy while the NW based devices increase efficacy.

In Figure 5.2-8 the electroluminescence spectra of the devices on ITO and on the G2G IP NW electrodes are presented. Due to the general broad transmittance spectra of the NW, the same emission color as on the ITO device is visible. The CIE coordinates are: x = 0.4515 and y = 0.5208 for the NW device and: x = 0.4624 and y = 0.5238 for the ITO device.

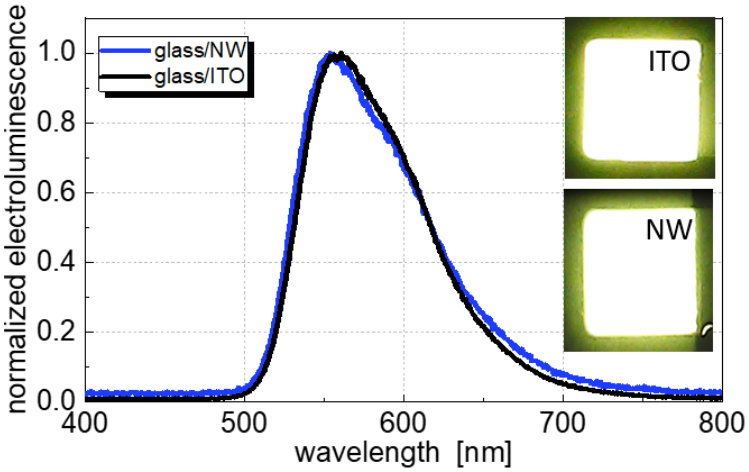

Figure 5.2-8: EL-spectra of OLEDs on NW and ITO electrodes on glass, showing that the emission color is independent of electrode type. Taken from [52] and modified.

5.3 Summary of NW electrodes

Chapter 5 discussed different ways to realize a NW TE and proofed the concept of the electrodes in inverted OLEDs. Spraying and solution parameters were optimized to achieve the best trade-off between conductivity and transmittance. Initial NW films showed a high RMS roughens of 46 nm. To flatten the electrode, surface an embedding process was introduced.

The standard process order was spraying and welding the NWs on glass and transferring them to glass. While transferring the process to fabricate NW films on PET, it was observed that the PET substrate starts to melt during the plasma welding of the NWs. This problem was tackled by two attempts: first, Kapton® was introduced as processing substrate for the NWs. During the embedding process the NW films could be transferred from Kapton® to PET to yield a flexible transparent electrode.

Second, a parallel approach was done by changing the process sequence from first curing and then embedding to first embedding and then curing (inverse process). This process was first tried successfully on glass. However, holes occurred in the OrmoComp® due to the plasma processing. These holes influence the haze of the samples, but not the total transmittance.

Nevertheless, the process offered the possibility of spraying NWs on PET and transfer them to another PET substrate, while the PET is reinforced with OrmoComp® to withstand the heat during plasma treatment. The resulting electrode has a sheet resistance of 12 Ω/sq and a T_{av} of 76.35 % and did not show significant sheet resistance changes under 5000 tensile bending cycles.

To test further process options for the embedded NW films, electrodes where sputter coated with 100 nm AZO. It was shown that the haze could be reduced by filling up the holes in the Ormocomp® layer. Unfortunately, total transmittance was reduced by 10 % by the AZO layer. Yet, sheet resistance remained the same, proofing the sputter process stability of the flexible transparent electrode.

The bottleneck for the developed electrode were experiments for the implementation in OLEDs. It was found out that the standard process cannot be applied for electrodes in devices since an inhomogeneous light emission caused by missing NW was observed. To work around this fact, NWs were sprayed at 110 °C to get rid of plasma processing. Still, plasma processing was necessary to maximize current density and minimize leakage in devices. Sticking with the inverse process for glass and PET was favored. P2P inverse processed NW electrodes applied in a solution processed inverse architecture OLED outperformed its ITO counterpart on PET in terms of efficacy and luminance. Compared to earlier work of embedded NWs on glass, with the same light emitting polymer, our electrode yields higher electrical currents which leads to higher luminance values than ITO based reference devices.

6 Overall conclusion

"Pass on what you have learned." – Master Yoda

Transparent electrodes on glass are widely applied in our society. However, the development of transparent electrodes on flexible substrates is still an ongoing research. Two approaches for such a development were targeted and discussed in this thesis.

Since sputtering is the state of the art industrial process for creating transparent electrodes, it was also chosen as the manufacturing method for the first approach. The most widely sputtered material for transparent electrodes is ITO. To overcome some of the drawbacks of ITO, such as its scarcity, high price, limited mechanical stability and therefore applicability on flexible substrates, dielectric/metal/dielectric (DMD) electrodes were developed.

To maximize the transmittance of the electrode in the optical wavelength range (400-700 nm), a transfer matrix algorithm was used to calculate the optimized layer thicknesses of the dielectric layers. The metal layer was kept constant at 10 nm to maximize conductivity. Three types of DMD electrodes were investigated.

Firstly, silver was chosen as metal film since it offers the best trade-off in terms of abundance, flexibility, conductivity and transmittance. ZnO proved to be a valuable oxide in transparent electrode applications and was hence chosen to be the first material choice for the dielectrics sandwiching the metal film. The tested ZnO/Ag/ZnO film already displayed similar transmittance, conductivity and roughness values compared to ITO.

Secondly, Al doped ZnO was tested as the dielectric underneath and above the Ag film. Similar properties as in the ZnO case were observed besides a higher average transmittance on PET. The higher transmittance is due to the larger bandgap caused by doping.

Thirdly, and most successfully, DMD electrodes were based on a TiO_x/Ag/AZO electrode on glass. In order to transfer the high performing layer architecture from glass to PET, detailed surface investigations were necessary. It was found that the initial PET roughness hampers a closed TiO_x film formation. The TiO_x layer morphology was enhanced by using a smoothing polymer interlayer. Hence, the highest performing electrode was achieved with the TiO_x/Ag/AZO layers not only on glass but also on PET.

To prove the superiority of this layer sequence against the commercial ITO standard electrode, OLEDs were manufactured on both electrode types on glass and PET substrates.

The TiO_x/Ag/AZO electrode-based devices outperformed the ITO based devices on glass and PET. On glass, an outstanding high luminance of almost 100000 cd/m^2 was achieved and on PET, a current efficacy of almost 10 cd/A could be reached.

The second approach of achieving flexible transparent electrodes was based on using sprayed silver nanowire films. Spray coating offers the possibility of easy upscaling and R2R implementation. The main challenge to implement nanowire thin films in flexible transparent electrodes is to reduce the initial surface roughness of the sprayed films. An embedding process was applied in order to reduce the roughness of the NWs. It was found that embedding of the nanowires did not only significantly reduce the RMS roughness but also thermally stabilize the heat sensitive PET. Hence, it was possibly to produce flexible transparent nanowire electrodes using only PET as substrate.

The silver nanowire-based electrode was then also tested in OLEDs. On glass, the devices on embedded nanowire electrodes outperformed its ITO counterpart in terms of maximum luminance. Additionally, on PET, the nanowire-based OLEDs outperform the ITO-based OLEDs both in terms of maximum luminance (34000 cd/m^2) and efficacy (4.8 cd/A).

Regarding both approaches, it can be concluded that the sputtered DMD electrodes yield higher transmittance and lower sheet resistance, resulting in higher device performance compared to the silver nanowire-based electrodes. Unfortunately, sputtering is a more complex process than spray coating which requires high vacuum facilities and is hence costlier. One can conclude that higher quality electrodes require higher cost manufacturing. Still, the developed NW electrode yielded sufficient performance to be a good low-cost competitor. In terms of their specific application on flexible substrates, both electrode types provide greater durability and mechanical stability than the commercial ITO standard.

7 Bibliography

1. Ellmer K. Past achievements and future challenges in the development of optically transparent electrodes. *Nat. Photonics* **6**, 809–817 (2012).
2. ECE alumni win Emmy for inventing the flat-panel plasma display | Electrical & Computer Engineering | U of I. https://ece.illinois.edu/newsroom/news/2541. accessed: 03.04.2019
3. Heilmeier G. H., Zanoni L. A. & Barton L. A. Dynamic Scattering: A New Electrooptic Effect in Certain Classes of Nematic Liquid Crystals. *Proc. IEEE* **56**, 1162–1171 (1968).
4. Tang C. W. Two-layer organic photovoltaic cell. *Appl. Phys. Lett.* **48**, 183–185 (1986).
5. Tang C. W. & Vanslyke S. A. Organic electroluminescent diodes. *Appl. Phys. Lett.* **51**, 913–915 (1987).
6. Jonda C. H., Mayer a B. R. & Stolz U. Surface roughness effects and their influence on the degradation of organic light emitting devices. *J. Mater. Sci.* **35**, 5645–5651 (2000).
7. Tak Y. H., Kim K. B., Park H. G., Lee K. H. & Lee J. R. Criteria for ITO (indium-tin-oxide) thin film as the bottom electrode of an organic light emitting diode. *Thin Solid Films* **411**, 12–16 (2002).
8. Kinner L., Nau S., Popovic K., Sax S., Burgués-Ceballos I., Hermerschmidt F., Lange A., Boeffel C., Choulis S. A. & List-Kratochvil E. J. W. Inkjet-printed embedded Ag-PEDOT:PSS electrodes with improved light out coupling effects for highly efficient ITO-free blue polymer light emitting diodes. *Appl. Phys. Lett.* **110**, 101107 (2017).
9. Park J., Shin K. & Lee C. Roll-to-Roll Coating Technology and Its Applications: A Review. *Int. J. Precis. Eng. Manuf.* **17**, 537–550 (2016).
10. Guillén C. & Herrero J. TCO/metal/TCO structures for energy and flexible electronics. *Thin Solid Films* **520**, 1–17 (2011).
11. Kim D. Y., Han Y. C., Kim H. C., Jeong E. G. & Choi K. C. Highly Transparent and Flexible Organic Light-Emitting Diodes with Structure Optimized for Anode/Cathode Multilayer Electrodes. *Adv. Funct. Mater.* **25**, 7145–7153 (2015).
12. Hofmann A. I., Cloutet E. & Hadziioannou G. Materials for Transparent Electrodes: From Metal Oxides to Organic Alternatives. *Adv. Electron. Mater.* **1700412**, (2018).
13. Ashcroft N. W. & Mermin N. D. *Solid state physics*. (Holt, Rinehart and Winston, 1976).
14. Kittel C. *Introduction to Solid State Physics*. *John Wiley & Sons, New York* (1996).
15. Holgate S. A. *Understanding Solid State Physics*. *Understanding Solid State Physics* (2009). doi:10.1201/b15977.
16. Ibach H. & Lüth H. *Solid-state physics: An introduction to principles of materials science*. *Solid-State Physics* 7th edition (Springer, 2010).
17. Tipler P. A. & Mosca G. *Physics for scientists and engineers.* (W.H. Freeman, 2003).

18. Van Zant P. *Microchip fabrication : a practical guide to semiconductor processing*. (McGraw-Hill, 2004).
19. Ellmer K. Past achievements and future challenges in the development of optically transparent electrodes. *Nat. Photonics* **6**, 808–816 (2012).
20. Griffiths D. *Introduction to electrodynamics*. (Pearson Education Asia, 2003).
21. Uzan J.-P. & Leclercq B. *The natural laws of the universe : understanding fundamental constants*. (Springer, 2008).
22. Young T. A course of lectures on natural philosophy and the mechanical arts. *J. Johnson* 413 https://archive.org/details/lecturescourseof01younrich/page/n4/mode/2up (1807). accessed: 18.07.2019
23. Shelby R. A., Smith D. R. & Schultz S. Experimental verification of a negative index of refraction. *Science (80-.).* **292**, 77–79 (2001).
24. Hecht E. *Optics (4th Edition)*. (Addison-Wesley, 2001).
25. Lakhtakia A. The Ewald--Oseen Extinction Theorem and the Extended Boundary Condition Method. in *The World of Applied Electromagnetics: In Appreciation of Magdy Fahmy Iskander* (eds. Lakhtakia A. & Furse C. M.) 481–513 (Springer International Publishing, 2018). doi:10.1007/978-3-319-58403-4_19.
26. Fox J. G. Experimental Evidence for the Second Postulate of Special Relativity. *Am. J. Phys.* **30**, 297–300 (1962).
27. Vella E., Messina F., Cannas M. & Boscaino R. Unraveling exciton dynamics in amorphous silicon dioxide: Interpretation of the optical features from 8 to 11 eV. *Phys. Rev. B* **83**, 174201 (2011).
28. Bennett H. E. & Stanford J. L. Structrue-related optical characteristics of thin metallic films in the visible and ultraviloet. *J. Phys. Chem.* **80 A**, 643–658 (1976).
29. Young H. D. & Sears F. W. *University physics.* (Addison-Wesley, 1992).
30. Vandergriff L. *Nature and Properties of Light*. (2015). doi:10.2134/agronj1923.00021962001500110011x.
31. Becker R. & Sauter F. *Electromagnetic fields and interactions*. (Dover Publications, 1982).
32. Nolting W. *Grundkurs Theoretische Physik 3: Elektrodynamik*. *Grundkurs Theoretische Physik 3: Elektrodynamik* (2013). doi:10.1007/978-3-663-12153-4.
33. Demtröder W. *Experimentalphysik 2 (Elektrizität und Optik)*. *Springer-Verlag Berlin Heidelberg* (2013). doi:10.1007/978-3-642-29944-5.
34. Haddouche I. & Cherbi L. Comparison of finite element and transfer matrix methods for numerical investigation of surface plasmon waveguides. *Opt. Commun.* **382**, 132–137 (2017).
35. Heavens O. S. & Singer S. F. Optical Properties of Thin Solid Films. *Phys. Today* (1956) doi:10.1063/1.3059910.

36. Born M. & Wolf E. *Principles of optics: electromagnetic theory of propagation, interference ... Principles of Optics Electromagnetic Theory of Propagation INterference and Diffraction of Light 2nd edition by Max Born Emil Wolf New York NY Pergamon Press 1964* (1999).

37. Hermerschmidt F., Burgués-Ceballos I., Savva A., Sepos E. D., Lange A., Boeffel C., Nau S., List-Kratochvil E. J. W. & Choulis S. A. High performance indium tin oxide-free solution-processed organic light emitting diodes based on inkjet-printed fine silver grid lines. *Flex. Print. Electron.* **1**, 035004 (2016).

38. Hermerschmidt F., Choulis S. A. & List-Kratochvil E. J. W. Implementing Inkjet-Printed Transparent Conductive Electrodes in Solution-Processed Organic Electronics. *Adv. Mater. Technol.* **4**, 1–16 (2019).

39. De S., Higgins T. M., Lyons P. E., Doherty E. M., Nirmalraj P. N., Blau W. J., Boland J. J. & Coleman J. N. Silver Nanowire Networks as Flexible ,. *ACSNano* **3**, 1767–1774 (2009).

40. Naghdi S., Rhee K., Hui D. & Park S. A Review of Conductive Metal Nanomaterials as Conductive, Transparent, and Flexible Coatings, Thin Films, and Conductive Fillers: Different Deposition Methods and Applications. *Coatings* **8**, 278 (2018).

41. Dimopoulos T., Radnoczi G. Z., Pécz B. & Brückl H. Characterization of ZnO:Al/Au/ZnO:Al trilayers for high performance transparent conducting electrodes. *Thin Solid Films* **519**, 1470–1474 (2010).

42. Bauch M. & Dimopoulos T. Design of ultrathin metal-based transparent electrodes including the impact of interface roughness. *Mater. Des.* **104**, 37–42 (2016).

43. Dimopoulos T., Radnoczi G. Z., Horváth Z. E. & Brückl H. Increased thermal stability of Al-doped ZnO-based transparent conducting electrodes employing ultra-thin Au and Cu layers. *Thin Solid Films* **520**, 5222–5226 (2012).

44. Ebner D., Bauch M. & Dimopoulos T. High performance and low cost transparent electrodes based on ultrathin Cu layer. *Opt. Express* **25**, A240 (2017).

45. Dimopoulos T., Bauch M., Wibowo R. A., Bansal N., Hamid R., Auer M., Jäger M. & List-Kratochvil E. J. W. Properties of transparent and conductive Al:ZnO/Au/Al:ZnO multilayers on flexible PET substrates. *Mater. Sci. Eng. B* **200**, 84–92 (2015).

46. Wright A. W. On the production of transparent metallic film by the electrical discharge in exhausted tubes. *Am. J. Sci.* (2013) doi:10.2475/ajs.s3-13.73.49.

47. Winkler N., Edinger S., Kautek W. & Dimopoulos T. Mg-doped ZnO films prepared by chemical bath deposition. *J. Mater. Sci.* **53**, 5159–5171 (2018).

48. Platforma Tecnologica Espanola de Impresion Avanzada. ITO alternatives to gain speed in the $2 billion TCF market. http://3neo.org/en/news/i/3443/48/alternativas-al-ito-ganan-puestos-en-el-mercado-de-los-2-billones-de-dolares-de-los-ctf (2012). accessed: 13.05.2019

49. MCDONALD A. New reports size up the Indium Tin Oxide (ITO) market. https://prnewsglobe.com/2019/01/11/indium-tin-oxide-ito-market-industry-report/ (2019). accessed: 23.04.2019

50. Kumar A. & Zhou C. The race to replace tin-doped indium oxide: Which material will win? *ACS Nano* **4**, 11–14 (2010).

51. Gondorf A., Geller M., Weißbon J., Lorke A., Inhester M., Prodi-Schwab A. & Adam D. Mobility and carrier density in nanoporous indium tin oxide films. *Phys. Rev. B - Condens. Matter Mater. Phys.* **83**, 212201 (2011).

52. Kinner L., Hermerschmidt F., Dimopoulos T. & List-kratochvil E. J. . W. Implementation of Flexible Embedded Nanowire Electrodes in Organic Light-Emitting Diodes. *Phys. Status Solidi - Rapid Res. Lett.* **2000305**, 6–11 (2020).

53. Granqvist C. G. Oxide electrochromics: An introduction to devices and materials. *Sol. Energy Mater. Sol. Cells* **99**, 1–13 (2012).

54. De Keersmaecker M., Lang A. W., Österholm A. M. & Reynolds J. R. All polymer solution processed electrochromic devices: A future without ITO? *Appl. Mater. Interfaces* **10**, 318568-31–579 (2018).

55. Woo H. G. & Choi H. T. *Indium: Properties, technological applications and health issues*. *Indium: Properties, Technological Applications and Health Issues* (Nova Science Publ, 2013).

56. Li J., Tao Y., Chen S., Li H., Chen P., Wei M. Z., Wang H., Li K., Mazzeo M. & Duan Y. A flexible plasma-treated silver-nanowire electrode for organic light-emitting devices. *Sci. Rep.* **7**, 1–9 (2017).

57. Xu R. P., Li Y. Q. & Tang J. X. Recent advances in flexible organic light-emitting diodes. *J. Mater. Chem. C* **4**, 9116–9142 (2016).

58. Ou Q.-D., Xu L.-H., Zhang W.-Y., Li Y.-Q., Zhang Y.-B., Zhao X.-D., Chen J.-D. & Tang J.-X. Light outcoupling enhanced flexible organic light-emitting diodes. *Opt. Express* **24**, A674 (2016).

59. Song C., Zhang N., Lin J., Guo X. & Liu X. Sb2O3/Ag/Sb2O3 Multilayer Transparent Conducting Films for Ultraviolet Organic Light-emitting Diode. *Sci. Rep.* **7**, 1–7 (2017).

60. Cao W., Li J., Chen H. & Xue J. Transparent electrodes for organic optoelectronic devices: a review. *J. Photonics Energy* **4**, 040990 (2014).

61. Kinner L., Bauch M., Wibowo R. A., Ligorio G., List-Kratochvil E. J. W. & Dimopoulos T. Polymer interlayers on flexible PET substrates enabling ultra-high performance, ITO-free dielectric/metal/dielectric transparent electrode. *Mater. Des.* **168**, 107663 (2019).

62. Maniyara R. A., Mkhitaryan V. K., Chen T. L., Ghosh D. S. & Pruneri V. An antireflection transparent conductor with ultralow optical loss (<2 %) and electrical resistance (<6Ωsq-1). *Nat. Commun.* **7**, 1–8 (2016).

63. Kim T. H., Park S. H., Kim D. H., Nah Y. C. & Kim H. K. Roll-to-roll sputtered ITO/Ag/ITO multilayers for highly transparent and flexible electrochromic applications. *Sol. Energy Mater. Sol. Cells* **160**, 203–210 (2017).

64. Ellmer K. Past achievements and future challenges in the development of optically transparent electrodes. *Nat Phot.* **6**, 809–817 (2012).

65. Cattin L., Bernède J. C. & Morsli M. Toward indium-free optoelectronic devices: Dielectric/metal/dielectric alternative transparent conductive electrode in organic photovoltaic cells: Towards indium-free optoelectronic devices. *Phys. status solidi* **210**, 1047–1061 (2013).

66. Zilberberg K. & Riedl T. Metal-nanostructures-a modern and powerful platform to create transparent electrodes for thin-film photovoltaics. *J. Mater. Chem. A* **4**, 14481–14508 (2016).

67. Klein A. Energy band alignment at interfaces of semiconducting oxides: A review of experimental determination using photoelectron spectroscopy and comparison with theoretical predictions by the electron affinity rule, charge neutrality levels, and the common anion. *Thin Solid Films* **520**, 3721–3728 (2012).

68. Li Y., Tang Z., Hänisch C., Will P. A., Kovačič M., Hou J. L., Scholz R., Leo K., Lenk S. & Reineke S. Ultrathin MoO3 Layers in Composite Metal Electrodes: Improved Optics Allow Highly Efficient Organic Light-Emitting Diodes. *Adv. Opt. Mater.* **7**, 1–8 (2019).

69. Sun Y., Yin Y., Mayers B. T., Herricks T. & Xia Y. Uniform silver nanowires synthesis by reducing AgNO3 with ethylene glycol in the presence of seeds and poly(vinyl pyrrolidone). *Chem. Mater.* **14**, 4736–4745 (2002).

70. Lee J. Y., Connor S. T., Cui Y. & Peumans P. Solution-processed metal nanowire mesh transparent electrodes. *Nano Lett.* **8**, 689–692 (2008).

71. Levermore P. A., Jin R., Wang X., de Mello J. C. & Bradley D. D. C. Organic Light-Emitting Diodes Based on Poly(9,9-dioctylfluorene- *co* -bithiophene) (F8T2). *Adv. Funct. Mater.* **19**, 950–957 (2009).

72. Park J. & Ham H. Sputter-patterned ITO-based organic light-emitting diodes with leakage current cut-off layers. *Org. Electron. physics, Mater. Appl.* **12**, 1872–1878 (2011).

73. Kim Y. S., Chang M. H., Lee E. J., Ihm D. W. & Kim J. Y. Improved electrical conductivity of PEDOT-based electrode films hybridized with silver nanowires. *Synth. Met.* **195**, 69–74 (2014).

74. Gaynor W., Burkhard G. F., McGehee M. D. & Peumans P. Smooth nanowire/polymer composite transparent electrodes. *Adv. Mater.* **23**, 2905–2910 (2011).

75. Han J., Yuan S., Liu L., Qiu X., Gong H., Yang X., Li C., Hao Y. & Cao B. Fully indium-free flexible Ag nanowires/ZnO:F composite transparent conductive electrodes with high haze. *J. Mater. Chem. A* **3**, 5375–5384 (2015).

76. Maisch P., Tam K. C., Lucera L., Egelhaaf H. J., Scheiber H., Maier E. & Brabec C. J. Inkjet printed

silver nanowire percolation networks as electrodes for highly efficient semitransparent organic solar cells. *Org. Electron. physics, Mater. Appl.* **38**, 139–143 (2016).

77. Ok K. H., Kim J., Park S. R., Kim Y., Lee C. J., Hong S. J., Kwak M. G., Kim N., Han C. J. & Kim J. W. Ultra-thin and smooth transparent electrode for flexible and leakage-free organic light-emitting diodes. *Sci. Rep.* **5**, 1–8 (2015).
78. de Guzman N., Lopez J., Vasquez Jr. M. & Balela M. D. Conductivity Improvement of Silver Nanowire Transparent Electrodes by Surface Plasma Treatment. *Mater. Sci. Forum* **890**, 89–92 (2017).
79. Kim T., Canlier A., Kim G. H., Choi J., Park M. & Han S. M. Electrostatic spray deposition of highly transparent silver nanowire electrode on flexible substrate. *ACS Appl. Mater. Interfaces* **5**, 788–794 (2013).
80. Akter T. & Kim W. S. Reversibly stretchable transparent conductive coatings of spray-deposited silver nanowires. *ACS Appl. Mater. Interfaces* **4**, 1855–1859 (2012).
81. Lee P., Lee J., Lee H., Yeo J., Hong S., Nam K. H., Lee D., Lee S. S. & Ko S. H. Highly stretchable and highly conductive metal electrode by very long metal nanowire percolation network. *Adv. Mater.* **24**, 3326–3332 (2012).
82. Jin Y., Deng D., Cheng Y., Kong L. & Xiao F. Annealing-free and strongly adhesive silver nanowire networks with long-term reliability by introduction of a nonconductive and biocompatible polymer binder. *Nanoscale* **6**, 4812–4818 (2014).
83. Ye S., Rathmell A. R., Chen Z., Stewart I. E. & Wiley B. J. Metal nanowire networks: The next generation of transparent conductors. *Adv. Mater.* **26**, 6670–6687 (2014).
84. Bai S., Wang H., Yang H., Zhang H. & Guo X. Corrigendum: Preparation of smooth, flexible and stable silver nanowires- polyurethane composite transparent conductive films by transfer method (Materials Research Express (2018) 5 (026406) DOI: 10.1088/2053-1591/aaab26). *Mater. Res. Express* **5**, (2018).
85. Xiao G., Makeiff D., Tao Y., Lu J. & Zhang Z. Improving the Adhesion between Silver Nanowire Transparent Electrode and PET Film Using a Crosslinkable Polymer. *2018 Int. Flex. Electron. Technol. Conf. IFETC 2018* 1–3 (2018) doi:10.1109/IFETC.2018.8583973.
86. Jang Y. R., Chung W. H., Hwang Y. T., Hwang H. J., Kim S. H. & Kim H. S. Selective Wavelength Plasmonic Flash Light Welding of Silver Nanowires for Transparent Electrodes with High Conductivity. *ACS Appl. Mater. Interfaces* **10**, 24099–24107 (2018).
87. Maurer J. H. M., Gonzalez-Garcia L., Reiser B., Kanelidis I. & Kraus T. Templated Self-Assembly of Ultrathin Gold Nanowires by Nanoimprinting for Transparent Flexible Electronics. *Nano Lett.* acs.nanolett.5b04319 (2016) doi:10.1021/acs.nanolett.5b04319.
88. Mitsubishi Polyester Film GmbH. Kunststofffolien im Vergleich. https://www.m-

petfilm.de/service/kunststofffolien-im-vergleich/ (2019). accessed: 15.06.2019

89. Harkema S., Mennema S., Barink M., Rooms H., Wilson J. S., van Mol T. & Bollen D. Large area ITO-free flexible white OLEDs with Orgacon PEDOT:PSS and printed metal shunting lines. *Proc. SPIE* **7415**, 74150T-74150T–8 (2009).

90. Park J., Lee J., Shin D. & Park S. Luminance uniformity of large-area OLEDs with an auxiliary metal electrode. *IEEE/OSA J. Disp. Technol.* **5**, 306–311 (2009).

91. Kang M.-G. & Guo L. J. Nanoimprinted Semitransparent Metal Electrodes and Their Application in Organic Light-Emitting Diodes. *Adv. Mater.* **19**, 1391–1396 (2007).

92. Sam F. L. M., Razali M. A., Jayawardena K. D. G. I., Mills C. A., Rozanski L. J., Beliatis M. J. & Silva S. R. P. Silver grid transparent conducting electrodes for organic light emitting diodes. *Org. Electron.* **15**, 3492–3500 (2014).

93. Georgiou E., Choulis S. A., Hermerschmidt F., Pozov S. M., Burgués-Ceballos I., Christodoulou C., Schider G., Kreissl S., Ward R., List-Kratochvil E. J. W. & Boeffel C. Printed Copper Nanoparticle Metal Grids for Cost-Effective ITO-Free Solution Processed Solar Cells. *Sol. RRL* 1700192 (2018) doi:10.1002/solr.201700192.

94. Pozov S. M., Schider G., Voigt S., Ebert F., Popovic K., Hermerschmidt F., Georgiou E., Burgués-Ceballos I., Kinner L., Nees D., Stadlober B., Rapley C., Ward R., Choulis S. A., List-Kratochvil E. J. W. & Boeffel C. Up-scalable ITO-free organic light emitting diodes based on embedded inkjet-printed copper grids. *Flex. Print. Electron.* **4**, 025004 (2019).

95. Tsai T. C., Chang H. C., Chen C. H., Huang Y. C. & Whang W. T. A facile dedoping approach for effectively tuning thermoelectricity and acidity of PEDOT:PSS films. *Org. Electron. physics, Mater. Appl.* **15**, 641–645 (2014).

96. Shi H., Liu C., Jiang Q. & Xu J. Effective Approaches to Improve the Electrical Conductivity of PEDOT:PSS: A Review. *Adv. Electron. Mater.* **1**, 1–16 (2015).

97. Sun K., Zhang S., Li P., Xia Y., Zhang X., Du D., Isikgor F. H. & Ouyang J. Review on application of PEDOTs and PEDOT:PSS in energy conversion and storage devices. *J. Mater. Sci. Mater. Electron.* **26**, 4438–4462 (2015).

98. Geim a K. & Novoselov K. S. The rise of graphene. *Nat. Mater.* **6**, 183–191 (2007).

99. Fang T., Konar A., Xing H. & Jena D. Carrier statistics and quantum capacitance of graphene sheets and ribbons. *Appl. Phys. Lett.* **91**, 092109 (2007).

100. Wu J., Agrawal M., Becerril H. A., Bao Z., Liu Z., Chen Y. & Peumans P. Organic Light-Emitting Diodes on Solution-Processed Graphene Transparent Electrodes. *ACS Nano* **4**, 43–48 (2010).

101. Zhang D., Ryu K., Liu X., Polikarpov E., Ly J., Tompson M. E. & Zhou C. Transparent, Conductive, and Flexible Carbon Nanotube Films and Their Application in Organic Light-Emitting Diodes. *Nano Lett.* **6**, 1880–1886 (2006).

102. Li J., Hu L., Wang L., Zhou Y., Grüner G. & Marks T. J. Organic Light-Emitting Diodes Having Carbon Nanotube Anodes. *Nano Lett.* **6**, 2472–2477 (2006).
103. Rowell M. W., Topinka M. a., McGehee M. D., Prall H.-J., Dennler G., Sariciftci N. S., Hu L. & Gruner G. Organic solar cells with carbon nanotube network electrodes. *Appl. Phys. Lett.* **88**, 233506 (2006).
104. Hu L., Hecht D. S. & Grüner G. Percolation in Transparent and Conducting Carbon Nanotube Networks. *Nano Lett.* **4**, 2513–2517 (2004).
105. Gruner J., Hamer P. J., Friend R. H., Huber H., Schera U. & Holmes A. B. A High Efficiency Blue-Light-Emitting Diode Based on Novel Ladder Poly(p-phenylene)s. *Adv. Mater.* **6**, 748–752 (1994).
106. Malliaras G., Salem J., Brock P. & Scott C. Electrical characteristics and efficiency of single-layer organic light-emitting diodes. *Phys. Rev. B* **58**, R13411–R13414 (1998).
107. Lu F., Liu X. & Xing Y. Numerical study of the influence of applied voltage on the current balance factor of single layer organic light-emitting diodes. *J. Appl. Phys.* **115**, 164508 (2014).
108. Pope M. & Swenberg C. E. *Electronic Processes in Organic Crystals and Polymers*. (Oxford University Press, 1999).
109. Chen S., Song L., Tao Z., Shao X., Huang Y., Cui Q. & Guo X. Neutral-pH PEDOT:PSS as over-coating layer for stable silver nanowire flexible transparent conductive films. *Org. Electron. physics, Mater. Appl.* **15**, 3654–3659 (2014).
110. Zhou Y. *et al.* A Universal Method to Produce Low–Work Function Electrodes for Organic Electronics. *Sciecne* **873**, 327–332 (2012).
111. Kacar R., Mucur S. P., Yildiz F., Dabak S. & Tekin E. Highly efficient inverted organic light emitting diodes by inserting a zinc oxide/polyethyleneimine (ZnO:PEI) nano-composite interfacial layer. *Nanotechnology* **28**, (2017).
112. Baptista A., Silva F., Porteiro J., Míguez J. & Pinto G. Sputtering physical vapour deposition (PVD) coatings: A critical review on process improvement andmarket trend demands. *Coatings* **8**, (2018).
113. Ehrlich G. & Stolt K. Surface Diffusion. *Ann. Rev. Phys. Chem.* **31:603**-**37**, (1980).
114. Magnetron Sputtering: Types of coating processes and Advantages. https://www.alcatechnology.com/en/blog/magnetron-sputtering/. accessed: 17.08.2019
115. Wasa K. *Handbook of Sputter Deposition Technology: Fundamentals and Applications for Functional Thin Films, Nanomaterials and MEMS*. (Elsevier Inc., 2012).
116. Scardaci V., Coull R., Lyons P. E., Rickard D. & Coleman J. N. Spray deposition of highly transparent, low-resistance networks of silver nanowires over large areas. *Small* **7**, 2621–2628 (2011).

117. Krantz J., Stubhan T., Richter M., Spallek S., Litzov I., Matt G. J., Spiecker E. & Brabec C. J. Spray-coated silver nanowires as top electrode layer in semitransparent P3HT:PCBM-based organic solar cell devices. *Adv. Funct. Mater.* **23**, 1711–1717 (2013).
118. CNT, Nanowires & Other Nanomaterials CNT, Nanowires & Other Nanomaterials | Sono-Tek. https://www.sono-tek.com/industry/alternative-energy-nanomaterials/cnt-nanowires-and-other-nanomaterials/. accessed: 17.08.2019
119. Koch N., Ueno N. & Wee A. T. S. *The Molecule-Metal Interface*. (Wiley-VCH Verlag, 2013).
120. Hüfner S. *Photoelectron spectroscopy: principles and applications*. (Springer, 2003).
121. Kinner, Lukas; List-Kratochvil, Emil J. W. and Dimopoulos T. Gentle plasma process for embedded silver-nanowire flexible transparent electrodes on temperature-sensitive polymer substrates. *Nanotechnology* **31**, (2020).
122. Huang Z. H., Zeng X. T., Sun X. Y., Kang E. T., Fuh J. Y. H. & Lu L. Influence of plasma treatment of ITO surface on the growth and properties of hole transport layer and the device performance of OLEDs. *Org. Electron.* **9**, 51–62 (2008).
123. Kim T. H., Choi B. H., Park J. S., Lee S. M., Lee Y. S. & Park L. S. Transparent Conductive ITO/Ag/ITO Multilayer Films Prepared by Low Temperature Process and Physical Properties. *Mol. Cryst. Liq. Cryst.* **520**, 209/[485]-214/[490] (2010).
124. Banerjee A. N., Ghosh C. K., Chattopadhyay K. K., Minoura H., Sarkar A. K., Akiba A., Kamiya A. & Endo T. Low-temperature deposition of ZnO thin films on PET and glass substrates by DC-sputtering technique. *Thin Solid Films* **496**, 112–116 (2006).
125. Ward-Harvey K. *Fundamental Building Materials*. (2009).
126. Kenoyer J. M. Bead technologies at Harappa, 3300-1900 BC: A comparative summary. *South Asian Archaeol. 2001* 157–170 (2005).
127. Kwan S., Kwan S. & Keller J. A. Early Chinese Faience and Glass Beads and Pendants. *J. Soc. Bead Res.* **25**, 3–39 (2013).
128. Zallen R. *The Physics of Amorphous Solids*. *The Physics of Amorphous Solids* (Wiley Blackwell, 2007). doi:10.1002/9783527617968.
129. Salmon P. S. Order within disorder. *Nat. Mater.* **1**, 87–88 (2002).
130. Laird T. Ullmann's Encyclopedia of Industrial Chemistry, 5th Edition VCH: Weinheim, Germany. 1996/1997. Section A, 28 vols. Section B, 8 vols. DM 19 400. *Org. Process Res. Dev.* **1**, 391–392 (1997).
131. Achintha M. *Sustainability of glass in construction*. *Sustainability of Construction Materials* (Elsevier Ltd., 2016). doi:10.1016/b978-0-08-100370-1.00005-6.
132. Whinfield J. R., Dickson J. T. & Lothian E. Polymeric linear terephthalic esters. *United States Patent Office* vol. 1 (1941).

133. Films D. T. *MSDS 'Melinex' Polyester Film*. (2007).
134. Thiele U. K. Polyester Additives. 1–5.
135. Özgür Ü., Alivov Y. I., Liu C., Teke A., Reshchikov M. A., Doğan S., Avrutin V., Cho S. J. & Morkç H. A comprehensive review of ZnO materials and devices. *J. Appl. Phys.* **98**, 1–103 (2005).
136. Han H., Theodore N. D. & Alford T. L. Improved conductivity and mechanism of carrier transport in zinc oxide with embedded silver layer. *J. Appl. Phys.* **103**, (2008).
137. Kuo F. L., Li Y., Solomon M., Du J. & Shepherd N. D. Workfunction tuning of zinc oxide films by argon sputtering and oxygen plasma: An experimental and computational study. *J. Phys. D. Appl. Phys.* **45**, (2012).
138. Schlaf R., Murata H. & Kafafi Z. H. Work function measurements on indium tin oxide films. *J. Electron Spectros. Relat. Phenomena* **120**, 149–154 (2001).
139. Mcintyre N. S., Johnston D., Chauvin W. J., Lau W. M., Schuetzle D., Shankar K. & Macdonald J. E. SIMS DEPTH PROFILING OF MULTILAYER METAGOXIDE THIN FILMS - IMPROVED ACCURACY USING A XENON PRIMARY ION. *Nucl. Instruments Methods Phys. Res.* **12**, 389–395 (1985).
140. Rakić A. D., Djurišić A. B., Elazar J. M. & Majewski M. L. Optical properties of metallic films for vertical-cavity optoelectronic devices. *Appl. Opt.* **37**, 5271 (1998).
141. Bingel A., Steglich M., Naujok P., Müller R., Schulz U., Kaiser N. & Ti¿½nnermann A. Influence of the ZnO:Al dispersion on the performance of ZnO:Al/Ag/ZnO:Al transparent electrodes. *Thin Solid Films* **616**, 594–600 (2016).
142. Guillén C. & Herrero J. Optical, electrical and structural characteristics of Al:ZnO thin films with various thicknesses deposited by DC sputtering at room temperature and annealed in air or vacuum. *Vacuum* **84**, 924–929 (2010).
143. Park S. H., Lee S. M., Ko E. H., Kim T. H., Nah Y. C., Lee S. J., Lee J. H. & Kim H. K. Roll-to-Roll sputtered ITO/Cu/ITO multilayer electrode for flexible, transparent thin film heaters and electrochromic applications. *Sci. Rep.* **6**, 1–12 (2016).
144. Stijn Mahieu. Biaxial alignment in sputter deposited thin films: PhD Thesis. *Univ. Gent* (2006) doi:http://dx.doi.org/10.1016/j.tsf.2006.06.027.
145. Zhang Y., Ji Q. & Pei X. Surface morphology and structure study of titanium dioxide thin films deposited on PET substrates. **82**, 883–886 (2009).
146. Eufinger K. Effect of deposition conditions and doping on the structure , optical properties and photocatalytic activity of d . c . magnetron sputtered TiO 2 thin films. (2007).
147. Endo T., Reddy L., Nishikawa H., Kaneko S., Nakamura Y. & Endo K. Composite Engineering - Direct Bonding of plastic PET Films by Plasma Irradiation. *Procedia Eng.* **171**, 88–103 (2017).
148. Chan C. M., Ko T. M. & Hiraoka H. Polymer surface modification by plasmas and photons. *Surf. Sci. Rep.* **24**, 1–54 (1996).

149. Junkar I., Vesel A., Cvelbar U., Mozetič M. & Strnad S. Influence of oxygen and nitrogen plasma treatment on polyethylene terephthalate (PET) polymers. *Vacuum* **84**, 83–85 (2009).
150. Pelagade S. M., Singh N. L., Qureshi A., Rane R. S., Mukherjee S., Deshpande U. P., Ganesan V. & Shripathi T. Investigation of surface properties of Ar-plasma treated polyethylene terephthalate (PET) films. *Nucl. Instruments Methods Phys. Res. Sect. B Beam Interact. with Mater. Atoms* **289**, 34–38 (2012).
151. Wang C., Zhang G., Wang X. & He X. Surface modification of poly(ethylene terephthalate) (PET) by magnet enhanced dielectric barrier discharge air plasma. *Surf. Coatings Technol.* **205**, 4993–4999 (2011).
152. Vasiljeva I. V., Mjakin S. V., Makarov A. V., Krasovsky A. N. & Varlamov A. V. Electron beam induced modification of poly(ethylene terephthalate) films. *Appl. Surf. Sci.* **252**, 8768–8775 (2006).
153. De Assis T. A. & Aarão Reis F. D. A. Smoothening in thin-film deposition on rough substrates. *Phys. Rev. E - Stat. Nonlinear, Soft Matter Phys.* **92**, 1–10 (2015).
154. Bayramoğlu G., Kahraman M. V., Kayaman-Apohan N. & Güngör A. Synthesis and characterization of UV-curable dual hybrid oligomers based on epoxy acrylate containing pendant alkoxysilane groups. *Prog. Org. Coatings* **57**, 50–55 (2006).
155. Zou K. & Soucek M. D. UV-curable organic-inorganic hybrid film coatings based on epoxidized cyclohexene derivatized linseed oil. *Macromol. Chem. Phys.* **205**, 2032–2039 (2004).
156. AMO GmbH. AMONIL & AMOPRIME - low viscosity imprint resist and adhesion promoter. *Data sheet* 5–6 (2015).
157. Stepanova M. & Dew S. *Nanofabrication: Techniques and principles*. *Nanofabrication: Techniques and Principles* vol. 9783709104 (2014).
158. Tsougeni K., Bourkoula A., Petrou P., Tserepi A., Kakabakos S. E. & Gogolides E. Photolithography and plasma processing of polymeric lab on chip for wetting and fouling control and cell patterning. *Microelectron. Eng.* **124**, 47–52 (2014).
159. Tsougeni K., Vourdas N., Tserepi A., Gogolides E. & Cardinaud C. Mechanisms of oxygen plasma nanotexturing of organic polymer surfaces: From stable super hydrophilic to super hydrophobic surfaces. *Langmuir* **25**, 11748–11759 (2009).
160. Zidan H. M. & Abu-Elnader M. Structural and optical properties of pure PMMA and metal chloride-doped PMMA films. *Phys. B Condens. Matter* **355**, 308–317 (2005).
161. Al-Taa'Y W. A., Oboudi S. F., Yousif E., Abdul Nabi M., Yusop R. M. & Derawi D. Fabrication and characterization of nickel chloride doped PMMA films. *Adv. Mater. Sci. Eng.* **2015**, (2015).
162. Haacke G. New figure of merit for transparent conductors. *J. Appl. Phys.* **47**, 4086–4089 (1976).
163. Glushko O., Klug A., List-Kratochvil E. J. W. & Cordill M. J. Relationship between mechanical

damage and electrical degradation in polymer-supported metal films subjected to cyclic loading. *Mater. Sci. Eng. A* **662**, 157–161 (2016).

164. Glushko O., Klug A., List-Kratochvil E. J. W. & Cordill M. J. Monotonic and cyclic mechanical reliability of metallization lines on polymer substrates. *J. Mater. Res.* **32**, 1760–1769 (2017).
165. Glushko O., Cordill M. J., Klug A. & List-Kratochvil E. J. W. The effect of bending loading conditions on the reliability of inkjet printed and evaporated silver metallization on polymer substrates. *Microelectron. Reliab.* **56**, 109–113 (2016).
166. Glushko O., Klug A., List-Kratochvil E. J. W. & Cordill M. J. Relationship between mechanical damage and electrical degradation in polymer-supported metal films subjected to cyclic loading. *Mater. Sci. Eng. A* **662**, 157–161 (2016).
167. Han Y. C., Lim M. S., Park J. H. & Choi K. C. ITO-free flexible organic light-emitting diode using ZnS/Ag/MoO3 anode incorporating a quasi-perfect Ag thin film. *Org. Electron.* **14**, 3437–3443 (2013).
168. Lu H. W., Huang C. W., Kao P. C. & Chu S. Y. ITO-free organic light-emitting diodes with MoO 3 /Al/MoO 3 as semitransparent anode fabricated using thermal deposition method. *Appl. Surf. Sci.* **347**, 116–121 (2015).
169. Xu L. H., Ou Q. D., Li Y. Q., Zhang Y. B., Zhao X. D., Xiang H. Y., Chen J. De, Zhou L., Lee S. T. & Tang J. X. Microcavity-free broadband light outcoupling enhancement in flexible organic light-emitting diodes with nanostructured transparent metal-dielectric composite electrodes. *ACS Nano* **10**, 1625–1632 (2016).
170. Socol M., Preda N., Breazu C., Florica C., Costas A., Istrate C. M., Stanculescu A., Girtan M. & Gherendi F. Organic heterostructures obtained on ZnO/Ag/ZnO electrode. *Vacuum* **154**, 366–370 (2018).
171. Gentle A. R., Yambem S. D., Burn P. L., Meredith P. & Smith G. B. AZO/Ag/AZO anode for resonant cavity red, blue, and yellow organic light emitting diodes. *J. Appl. Phys.* **119**, (2016).
172. Okigawa Y., Mizutani W., Suzuki K., Ishihara M., Yamada T. & Hasegawa M. Improvement of device performance of polymer organic light-emitting diodes on smooth transparent sheet with graphene films synthesized by plasma treatment. *Jpn. J. Appl. Phys.* **54**, (2015).
173. Forrest S. R., Bradley D. D. C. & Thompson M. E. Measuring the efficiency of organic light-emitting devices. *Adv. Mater.* **15**, 1043–1048 (2003).
174. Xie H., Yang X., Du D., Zhao Y. & Wang Y. Flexible transparent conductive film based on random networks of silver nanowires. *Micromachines* **9**, 1–8 (2018).
175. Zhu S., Gao Y., Hu B., Li J., Su J., Fan Z. & Zhou J. Transferable self-welding silver nanowire network as high performance transparent flexible electrode. *Nanotechnology* **24**, 335202 (2013).

176. Madaria A. R., Kumar A., Ishikawa F. N. & Zhou C. Uniform, highly conductive, and patterned transparent films of a percolating silver nanowire network on rigid and flexible substrates using a dry transfer technique. *Nano Res.* **3**, 564–573 (2010).

177. Madaria A. R., Kumar A. & Zhou C. Large scale, highly conductive and patterned transparent films of silver nanowires on arbitrary substrates and their application in touch screens. *Nanotechnology* **22**, (2011).

178. Nam S., Song M., Kim D.-H., Cho B., Lee H. M., Kwon J.-D., Park S.-G., Nam K.-S., Jeong Y., Kwon S.-H., Park Y. C., Jin S.-H., Kang J.-W., Jo S. & Kim C. S. Ultrasmooth, extremely deformable and shape recoverable Ag nanowire embedded transparent electrode. *Sci. Rep.* **4**, 4788 (2014).

179. Zhang H., Bai S., Guo X., Yang H. & Wang H. Corrigendum: Preparation of smooth, flexible and stable silver nanowires- polyurethane composite transparent conductive films by transfer method *Mater. Res. Express* **5**, 059501 (2018).

180. Jung E., Kim C., Kim M., Chae H., Cho J. H. & Cho S. M. Roll-to-roll preparation of silver-nanowire transparent electrode and its application to large-area organic light-emitting diodes. *Org. Electron. physics, Mater. Appl.* **41**, 190–197 (2017).

181. Burgués-Ceballos I., Kehagias N., Sotomayor-Torres C. M., Campoy-Quiles M. & Lacharmoise P. D. Embedded inkjet printed silver grids for ITO-free organic solar cells with high fill factor. *Sol. Energy Mater. Sol. Cells* **127**, 50–57 (2014).

182. Doraiswamy a., Jin C., Narayan R. J., Mageswaran P., Mente P., Modi R., Auyeung R., Chrisey D. B., Ovsianikov a. & Chichkov B. Two photon induced polymerization of organic-inorganic hybrid biomaterials for microstructured medical devices. *Acta Biomater.* **2**, 267–275 (2006).

183. Aura S., Jokinen V., Laitinen M., Sajavaara T. & Franssila S. Porous inorganic-organic hybrid material by oxygen plasma treatment. *J. Micromechanics Microengineering* **21**, (2011).

184. ToolBox E. Thermal Conductivity of common Materials and Gases. https://www.engineeringtoolbox.com/thermal-conductivity-d_429.html (2003). accessed: 17.07.2019

185. DuPont™. Kapton®. **5213**, 1–4 (2019).

186. Haacke G. New figure of merit for transparent conductors. *J. Appl. Phys.* **47**, 4086–4089 (1976).

187. Lian L., Dong D., Feng D. & He G. Low roughness silver nanowire flexible transparent electrode by low temperature solution-processing for organic light emitting diodes. *Org. Electron.* **49**, 9–18 (2017).

188. Yu Z., Zhang Q., Li L., Chen Q., Niu X., Liu J. & Pei Q. Highly flexible silver nanowire electrodes for shape-memory polymer light-emitting diodes. *Adv. Mater.* **23**, 664–668 (2011).